

Luminescence investigation of bulk solar silicon and silicon thin films on glass substrate

Von der Fakultät für Mathematik, Naturwissenschaften und Informatik
der Brandenburgischen Technischen Universität Cottbus - Senftenberg

zur Erlangung des akademischen Grades

Doktor der Naturwissenschaften
(Dr. rer. nat.)

genehmigte Dissertation

vorgelegt von

Diplomphysiker

Daniel Mankovics

geboren am 29. August 1985 in Cottbus, Deutschland

Gutachter: apl. Prof. Dr. sc. nat. Martin Kittler

Gutachter: Prof. Dr. rer. nat. habil. Jürgen Reif

Gutachter: PD. Dr. rer. nat. habil. Hartmut S. Leipner

Tag der mündlichen Prüfung: 22.06.2015

Abstract

The aim of this work is to study the optical properties of crystal defects in multicrystalline solar silicon and poly-/microcrystalline silicon thin films on glass substrate.

First a setup for photoluminescence imaging on multicrystalline silicon solar wafers was developed. This system is suitable for detecting band-to-band luminescence as well as defect-related luminescence at room temperature on large-scale wafers at different stages of their processing.

Spectroscopic photoluminescence investigations of multicrystalline silicon solar wafers indicated a new intense luminescence line at ≈ 0.91 eV at room temperature. The origin of this line is probably found in a specific grain boundary. Furthermore, luminescence in the region of 0.8 eV was investigated in detail, and it was found that probably oxygen is responsible for a peak at 0.77 eV at 80 K.

Electroluminescence investigations at room temperature at both materials exhibit extended defect structures such as grain boundaries. Furthermore, it can be concluded that electroluminescence imaging in reverse bias mode indicate on serious breakdown points in solar cells, which can lead to destruction of solar cells and modules. By comparing defect-related and reverse bias electroluminescence images, a difference in the spatial distribution of defects emitting D1 radiation and defects emitting light under reverse bias beyond -12 V is detectable.

In addition, there seems to be a correlation in the distribution of non-doping impurities and photoluminescence. Concerning this, vertical slabs of two silicon blocks were examined by means of Fourier-transform infrared spectroscopy and photoluminescence. A correlation of the distributions of interstitial oxygen and the band-to-band luminescence profiles could be found. Additionally, a correlation between D3/D4 luminescence profile and nitrogen distribution in the blocks was observed.

Finally, the growth process, particularly the transition from amorphous to microcrystalline silicon by PECVD, was studied by combined photoluminescence and Raman investigations. Formation of silicon nano-grains was detected by means of photoluminescence and Raman spectroscopy.

Kurzfassung

Das Ziel dieser Arbeit ist es, die optischen Eigenschaften von Kristalldefekten in multikristallinem Solarsilizium und poly-/mikrokristallinen Silizium-Dünnschichten auf Glas-Substrat zu studieren.

Zuerst wurde ein Aufbau für Photolumineszenz-Imaging an multikristallinem Silizium-Solarwafern entwickelt. Dieses System eignet sich zur Erfassung von Band-zu-Band-Lumineszenz sowie Defek-Lumineszenz bei Raumtemperatur großer Solarwafer nach verschiedenen Prozessschritten.

Spektroskopische Photolumineszenz-Untersuchungen von multikristallinen Silizium-Solarwafern zeigte eine neue intensive Lumineszenzlinie bei ≈ 0.91 eV bei Raumtemperatur. Der Ursprung dieser Linie liegt wahrscheinlich in einer bestimmten Korngrenze. Weiterhin wurde die Lumineszenz im Bereich von 0.8 eV im Detail untersucht, und es wurde gefunden, dass wahrscheinlich Sauerstoff für einen Peak bei 0.77 eV bei 80 K verantwortlich ist.

Elektrolumineszenz Untersuchungen bei Raumtemperatur an beiden Materialien zeigen ausgedehnte Defektstrukturen wie Korngrenzen. Darüber hinaus kann der Schluss gezogen werden, dass das Elektrolumineszenz-Imaging im Rückwärtsvorspannungs-Modus auf schwerwiegende Durchbruchstellen in Solarzellen hinweist, die zur Zerstörung von Solarzellen und Modulen führen kann. Durch Vergleich von Defektlumineszenz- und Sperrvorspannungs-Elektrolumineszenz-Bildern ist ein Unterschied in der räumlichen Verteilung der Defekte, die D1 emittieren, und der Durchbruchlumineszenz unter Sperrvorspannung über -12 V erkennbar.

Außerdem gibt es Hinweise auf einen Zusammenhang bei der Verteilung von nicht-dotierenden Verunreinigungen und der Lumineszenz. Hierzu wurden vertikale Scheiben zweier Siliziumblöcke mittels Fourier-Transformations-Infrarotspektroskopie und Photolumineszenz untersucht. Eine Korrelation der Verteilung von interstitiellem Sauerstoff und den Band-zu-Band-Lumineszenz-Profilen konnte gefunden werden. Außerdem wird eine Korrelation zwischen dem D3/D4 Lumineszenzprofil und der Stickstoffverteilung in den Blöcken beobachtet.

Schließlich wurde der Wachstumsprozeß, insbesondere der Übergang von amorphem zu mikrokristallinem Silizium mittels PECVD, durch Kombination der Photolumineszenz- und Raman-Methoden untersucht. Bildung von Silizium-Nanokörnern wurde mittels Photolumineszenz- und Raman-Spektroskopie detektiert.

Contents

Introduction	9
I. Theoretical and experimental background	12
1. Crystalline silicon solar cells	13
1.1. Multicrystalline ingot fabrication	13
1.2. Wafer and cell manufacturing	16
1.3. The solar cell	21
1.4. Polycrystalline silicon thin film on glass substrate	29
2. Defects and recombination processes in silicon	31
2.1. Defects	31
2.1.1. Point defects	31
2.1.2. Extended defects	33
2.2. Recombination processes	36
2.2.1. Radiative recombination	37
2.2.2. Defect-related radiation	41
2.2.3. Non-radiative recombination	43
3. Experimental methods	46
3.1. Scanning photoluminescence	46
3.2. Luminescence imaging	46
3.3. Fourier-transform infrared spectroscopy	50
3.4. Electron-beam-induced current	54

II. Measurements and results	55
4. Photoluminescence imaging	56
4.1. Samples and measurements	56
4.2. Results and discussion	59
4.2.1. Luminescence around 0.8 eV	59
4.2.2. Comparison of BB and D1 images	63
4.2.3. Influence of different processing steps	65
4.3. Summary	71
5. Spectroscopic photoluminescence	73
5.1. Multicrystalline silicon	73
5.1.1. Di luminescence	74
5.1.2. Oxygen-related luminescence	78
5.2. Polycrystalline silicon thin film on glass substrate	90
5.2.1. One crystallization step	91
5.2.2. Two crystallization steps	93
5.3. Summary	93
6. Electroluminescence imaging	96
6.1. EL on mc-Si solar cells in forward and reverse bias mode and EBIC	96
6.1.1. Samples and measurements	96
6.1.2. Results and discussion	97
6.2. EL on silicon thin film on glass cells in forward and reverse bias mode	103
6.2.1. Samples and measurements	104
6.2.2. Results and discussion	104
6.3. Summary	109
7. Comparative analysis of PL and FTIR	111
7.1. FTIR	111
7.2. PL measurements	113
7.3. Comparison of FTIR and PL	115
7.4. Summary	120
8. Growth process of microcrystalline silicon	121
8.1. Samples and measurements	122

8.2. Results and discussion	123
8.3. Summary	133
9. Conclusions	134
Scientific visibility	136
References	139
Acknowledgments	152

Introduction

Solar energy is the most abundant energy resource on earth. The solar energy that hits the earth's surface in 90 minutes is about the same as the amount consumed by all human activities in a year. Direct conversion of sunlight into electricity in photovoltaic cells is one of the three main solar active technologies, the two others being concentrating solar power and solar thermal collectors for heating and cooling. Today, photovoltaics (PV) provide 0.1% of total global electricity generation. However, PV is expanding very rapidly due to dramatic cost reductions. Photovoltaic is a commercially available and reliable technology with a significant potential for long-term growth.

PV systems directly convert solar energy into electricity. The basic building block of a PV system is the PV cell, which is a semiconductor device that converts solar energy into direct-current electricity. PV cells are interconnected to form a PV module. The modules combined with a set of additional application-dependent system components (for example inverters, batteries, electrical components, and mounting systems), form a PV system. These systems are highly modular, i.e. modules can be linked together to provide power ranging from a few watts to tens of megawatts.

Research, development and industrialization have led to a portfolio of available PV technology options at different levels of maturity. Commercial PV modules may be divided into two broad categories: wafer based crystalline silicon and thin films. Crystalline silicon (c-Si) modules represent 85 – 90% of the global annual market today. C-Si modules are subdivided into two main sorts: (i) single-crystalline (sc-Si), and (ii) multicrystalline (mc-Si). Thin films currently account for 10% to 15% of global PV module sales. They are subdivided into three main families: (i) amorphous (a-Si) and micromorph silicon (a-Si/ μ c-Si), (ii) Cadmium-Telluride (CdTe), and (iii) Copper-Indium-Diselenide (CIS) and Copper-Indium-Gallium-Diselenide (CIGS). [IEA10]

For large-scale cell production, mc-Si is used predominantly. It is cost efficient and allows fabrication of devices with a remarkable performance. The mc-Si contains different type of defects, which should be engineered and monitored in the course of the cell production,

in order to minimize their impact over the final device.

Among those defects dislocations are recognized as a major factor limiting the cell performance [KSA⁺02]. For instance, the interaction of impurities with dislocations can significantly amplify their detrimental influence. That is why a monitoring technique is needed for tracking the dislocation activity in the production process at as many as possible steps. The dislocations can be sensed by a contactless optical method, based on their specific luminescence at room temperature. Indeed, it has been found, that besides the radiative band-to-band (BB) recombination, dislocated silicon shows a quartet of lines (D1 - D4) [DN76] in the near infrared luminescence spectrum. The spectral features of those appear in the sub-band gap region and are observable at low temperatures mainly. At room temperature, the BB and only D1 line can be detected.

Aim and outline of the work

The goals of this work are the adaption of investigation techniques used for bulk silicon solar cells and wafers to silicon thin films on glass substrate. Electroluminescence investigations in forward and reverse bias mode are conducted at multicrystalline silicon solar cells and polycrystalline thin film cells. Photoluminescence investigations were carried out at bulk multicrystalline silicon for detailed analysis of two specific defect lines. Additionally, thin silicon films are investigated by photoluminescence to consider the material properties in comparison to bulk material. Additionally, it was tried to observe if there can be drawn a correlation between FTIR and PL measurements. Finally, the growth process of microcrystalline silicon thin film were studied by combined PL and Raman investigations.

This work is divided into two main parts; the first deals with the theoretical and experimental background, and the second consists experimental results and conclusions. This work is divided in seven chapters, which are briefly described in the following.

The first chapter provides a description of solar cell manufacturing, especially for multicrystalline silicon solar cells, starting at the ingot fabrication. Finally, the production of solar cells made of polycrystalline silicon thin films on glass substrate is described.

In chapter two, theoretical background, regarding to defects in silicon, is presented. Different types of defects in crystalline silicon are presented and recombination processes in silicon are described.

The third chapter presents the used experimental methods, including scanning photoluminescence, luminescence imaging, Fourier transform infrared spectroscopy, and electron-beam-induced-current (EBIC).

In chapter four photoluminescence imaging at various manufacturing steps of silicon solar wafers are presented.

Chapter five deals with temperature dependent spectroscopic photoluminescence investigations on bulk multicrystalline silicon wafer, showing two new luminescence lines. Furthermore, silicon thin film material on glass is investigated and the results are compared to bulk material.

In chapter six electroluminescence investigations in forward and reverse bias mode on bulk and thin film silicon solar cells are presented and discussed.

In chapter seven photoluminescence and FTIR investigations on vertical slabs of silicon blocks are compared to each other.

Chapter eight describes the growth process of microcrystalline silicon studied by combined photoluminescence and Raman investigations.

A summary of the results and the conclusions drawn on their base are given in chapter nine.

Part I.

Theoretical and experimental background

1. Crystalline silicon solar cells

Nowadays, the dominant semiconductor in photovoltaics is silicon. The main source is multicrystalline silicon. Multicrystalline silicon devices are generally less efficient than those of single-crystal silicon are, but they can be less expensive to produce. The silicon feedstock for photovoltaics is produced by the Siemens process or by upgrading metallurgical grade silicon. The first section describes the ingot fabrication for multicrystalline silicon; the second section describes a common solar cell process, whereas the third section deals with the cell structure. The last section gives a brief description of solar cells made of polycrystalline silicon on glass substrate.

1.1. Multicrystalline ingot fabrication

There are two different fabrication technologies for multicrystalline silicon the Bridgman and the block casting process (cf. illustrations in Figures 1.1 and 1.2). The main difference between both techniques is, that for the melting and crystallization process only one crucible (Bridgman) is used, whereas for the crystallization process a second crucible (block casting) is necessary. In case of the Bridgman process, a silicon nitride (Si_3N_4) coated quartz crucible is usually used for melting of the silicon raw material and subsequent directional solidification of the multicrystalline ingot. The Si_3N_4 coating thereby serves as an anti-sticking layer, preventing the adhesion of the silicon ingot to the crucible walls during crystallization, which would destroy the silicon ingot and the crucible. Concerning the block casting process, the melting is performed in a crucible without coating, whereas - after pouring the molten silicon into a second crucible - for the crystallization also a Si_3N_4 coated one is used. In general, in both processes, the crystallization starts at the bottom of the crucible by lowering the temperature below the melting point of silicon (1410°C). Within the Bridgman process, the temperature reduction is achieved by descending the liquid silicon-containing crucible out of the hot area. Contrarily, the temperature control during block casting is achieved by a corresponding adjustment of heaters, whereas the

crucible itself is not moved. After solidification starts in the bottom region, the crystallization front, that is the liquid-solid interphase, moves in a vertical direction upwards through the crystallization crucible. This so-called directional solidification results in a columnar crystal growth and consequently adjacent wafers fabricated out of the ingots show nearly identical defect structures (grain boundaries and dislocations). [LH03, NU09]

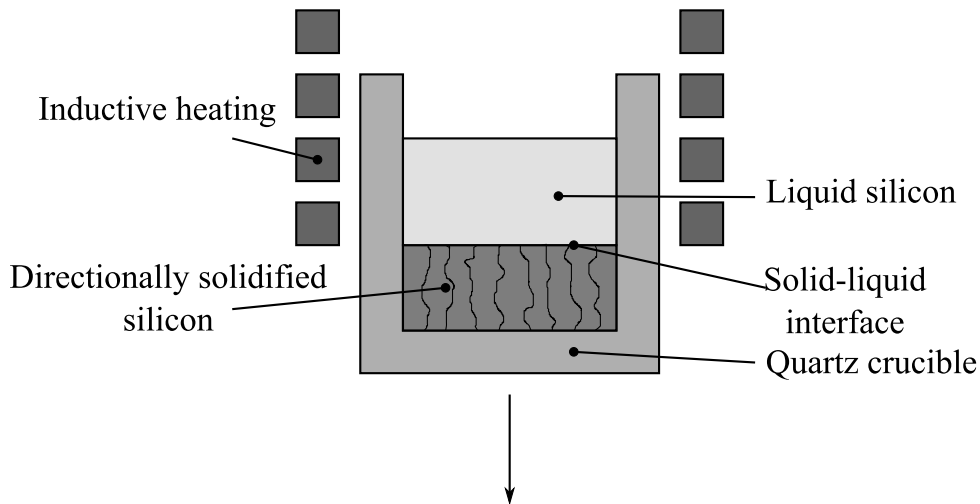


Figure 1.1.: Conventional Bridgman technique that still is mainly used for the fabrication of multicrystalline ingots. Both melting and crystallization of the silicon is performed in a Si_3N_4 coated quartz crucible. Crystallization is realized by slowly moving downward the liquid silicon containing crucible out of the inductively heated hot zone of the process chamber. [LH03]

Doping

Standard multicrystalline silicon for solar cells is *p*-type material (boron doped) with a specific electrical resistivity of about $1 \Omega \text{ cm}$, which corresponds to a boron concentration of about $2 \times 10^{16} \text{ cm}^{-3}$. The specific resistivity can be adjusted by the boron concentration. The typical specific resistivity for solar cells is in a range of 0.1 to $5 \Omega \text{ cm}$ and is adjusted in a way that optimal solar cell performance is guaranteed. For phosphorus as an *n*-type dopant, the disadvantage of lower minority charge carrier (i.e. holes) mobility and a more complicated solar cell process is encountered. However, results indicate that the activity of extended defects in *n*-type material is lower, which could render it an attractive new feedstock source for photovoltaics. [LH03]

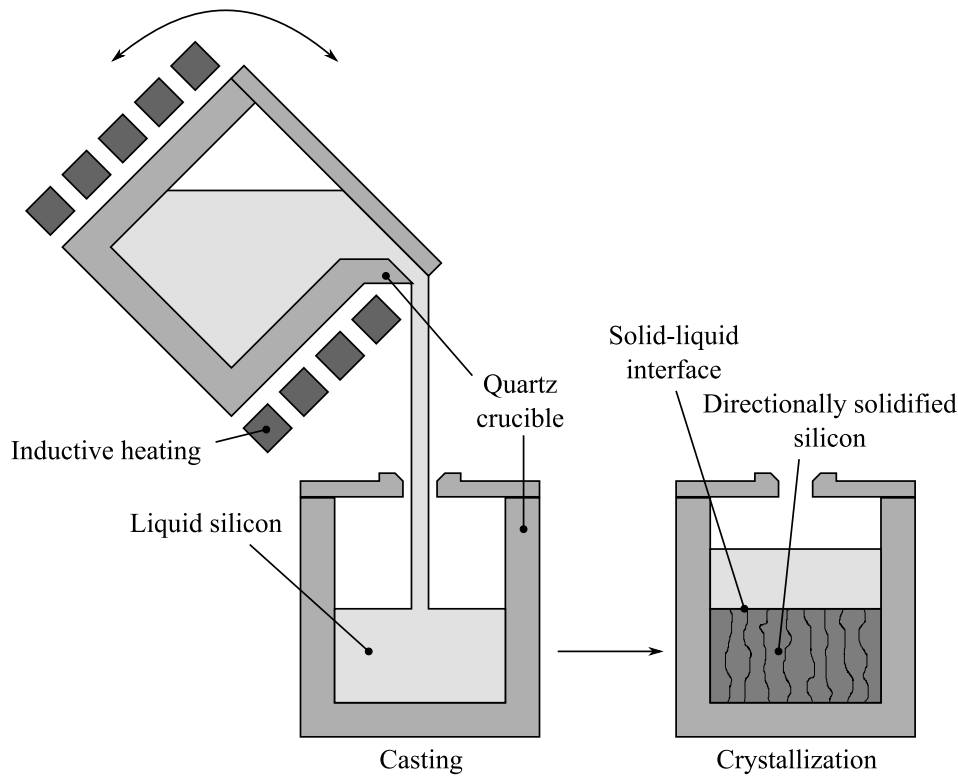


Figure 1.2.: Block casting process for the fabrication of multicrystalline silicon. After melting the silicon in a quartz pot, the silicon is poured into a second quartz crucible with a Si_3N_4 coating. The heating elements of the crystallization crucible are not shown in the figure. In comparison to the Bridgman technique (see Figure 1.1), shorter crystallization and cooling times can be realized by employing a more variable heater system. [LH03]

Impurities

Besides the intentionally introduced impurity for doping (e.g. boron), higher impurity concentrations are observed for oxygen, carbon and nitrogen in multicrystalline silicon. During crystallization SiO_2 , Si_3N_4 and SiC precipitates can be formed. Moreover, transition metals play a significant role in solar silicon.

The interstitial oxygen concentration is affected by the oxygen incorporation via the quartz crucible during melting, the evaporation of SiO on the melt surface and the oxygen-containing coating of the crucible. The oxygen content decreases with increasing block height. Typical interstitial oxygen content from different Bridgman processes are given in Table 1.1.

Carbon is another noteworthy impurity in silicon as it appears in a higher concentration than those of boron for doping. Typical concentrations of substitutional carbon are given in

Table 1.1 as well. Generally, the concentration is increasing with increasing block height. The sources for carbon are mainly the graphite parts like heaters in the crystallization chamber and the CO in the gas atmosphere. Due to a high carbon concentration, needle-shaped SiC crystals are formed within the silicon material. SiC effectively shorts the $p-n$ junction of the solar cell, leading to a decreased efficiency. [RTJ⁺10]

Ingot Position	interstitial oxygen $[O_i]$ [10^{17} cm^{-3}]		substitutional carbon $[C_s]$ [10^{17} cm^{-3}]	
	process 1	process 2	process 1	process 2
Bottom	3.0	7.5	0.5	7.0
Middle	1.0	1.5	1.2	11
Top	0.4	0.5	10	13

Table 1.1.: Interstitial oxygen $[O_i]$ and substitutional carbon $[C_s]$ concentration from Bridgman material of two different processes. For the determination of the oxygen and carbon content Fourier Transform Infrared Spectroscopy (FTIR) was used.

1.2. Wafer and cell manufacturing

Wafering

Today the multi-wire wafering technique is used to cut the ingots into wafer mostly. The principle of this technology is drafted in Figure 1.3. A single wire is fed from a supply spool through a pulley and tension control unit to the wire guides that are grooved with a constant pitch. Multiple strands of a wire net are formed by winding the wire on the wire guides through the 800 parallel grooves. A take-up spool collects the used wire. The wire is pulled by the torque exerted by the main drive and slave. The tension on the wire is maintained by a feedback control unit. The silicon crystal on the holder is pushed against the moving wire web and sliced into hundreds of wafers at the same time.

Cutting is achieved by abrasive slurry, which is supplied through nozzles over the wire web and carried by the wire into the sawing channel. The slurry consists of a suspension of hard lapping particles, mainly SiC powders. The mean grain size of these SiC particles is about $2 \mu\text{m}$ in diameter. The main purpose of the slurry is to transport the abrasive particles into the sawing channels and to the crystal surface.

The kerf loss and surface quality are determined by the diameter of the wire, the size distribution of the SiC particles, and possible transverse vibrations of the wire. Typical diameters of steel wires are around $100 \mu\text{m}$, which leads to kerf losses of around $125 \mu\text{m}$

per wafer. Today's wafer thickness is between $100 - 200 \mu\text{m}$, which means a loss of silicon to around 50 %. [Möl06, SSPR09]

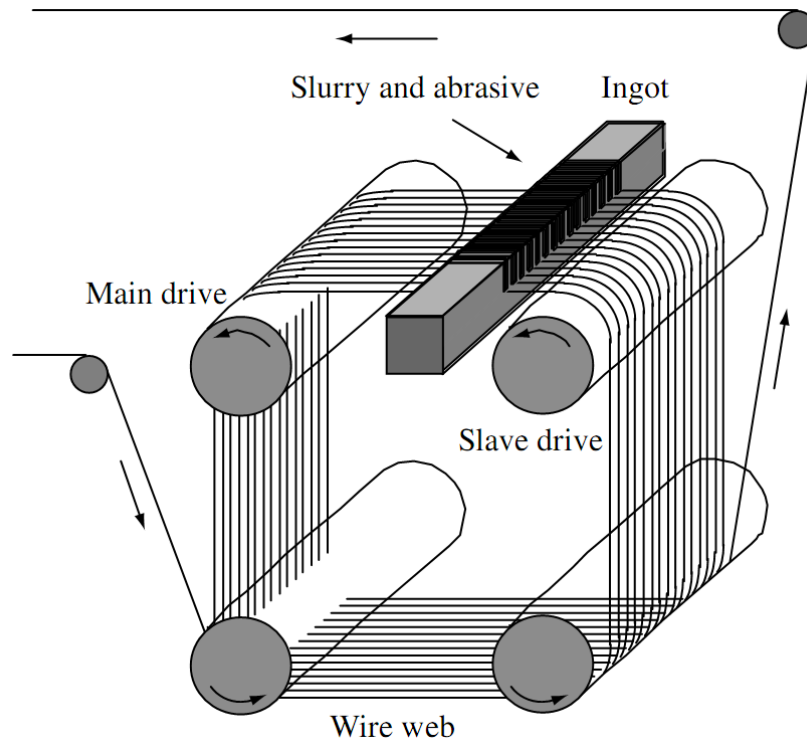


Figure 1.3.: Schematic diagram depicting the principle of the multi-wire sawing technique. [LH03]

Solar cell process

Figure 1.4 shows the main steps of a process for solar cell fabrication based on screen-printing. With minor modifications, many manufacturers use this process. Each step is described shortly in the following text. Values of temperature, time and so on are indicative only. It is necessary to describe the cell process briefly, because in the chapter of photoluminescence imaging (4) solar wafers after different processing steps are investigated.

1. *Starting material*: The raw material is solar grade Cz-Si, round in origin but mostly trimmed to a pseudo square shape, or multicrystalline square wafers. Wafer dimensions are between 10 and 15 cm side, and 100 and $200 \mu\text{m}$ thickness, respectively. Doping is *p*-type (boron) to a resistivity of around $1 \Omega \text{cm}$.
2. *Saw damage removal*: The surface of the “as-cut” wafers have a high degree of damage due to sawing. To remove these damages, ten microns are etched off from each face

in alkaline solutions. The wafers are immersed in tanks containing the solution under temperature and composition control.

3. *Texturization*: NaOH or KOH etching leads to microscopic pyramids, which is commonly employed in the industry. Their size must be optimized, since very small pyramids lead to high reflection, while very large ones can hinder the formation of the contacts. To ensure complete texturing coverage and adequate pyramid size, the concentration, temperature and agitation of solution, and the duration of the bath has to be controlled. The alkaline solution is at higher concentration and at higher temperature as used for saw damage removal. Alcohol is added to improve homogeneity through an enhancement of the wettability of the silicon surface. Typical parameters are 5% NaOH concentration, 80 °C and 15 min.
4. *Phosphorus diffusion*: The phosphorus deposition is made in belt furnaces, where solid phosphorus sources are used. Screen-printed, spun-on or CVD pastes containing phosphorus compounds are applied on one wafer face and, after drying, placed in a conveyor belt passing through the furnace. The temperature inside it can be adjusted in several zones and gases can be supplied. The temperature cycle undergone by the wafer will mimic the temperature profile along the furnace with the time scale set by the advancing speed of the belt. A cycle begins with several minutes at around 600 °C with clean air to burn off organic materials of the paste, followed by the diffusion step in nitrogen at 950 °C for 15 min. After diffusion, an amorphous glass of phosphosilicates remains at the surface that is etched off in diluted HF.
5. *Junction isolation*: The *n*-type region at the edges of the wafer would interconnect the front and back contacts: the junction would be shunted by this path translating into a very low shunt resistance. To remove this region, dry etching, low temperature procedures are used.
6. *ARC deposition*: Titanium dioxide (TiO₂) is used for creating the anti-reflecting coating due to its near optimum refraction index for encapsulated cells. Silicon nitride (SiN_x) is also used as ARC material, which also yields to a passivation of the surfaces. The coatings are commonly deposited by PECVD (plasma-enhanced chemical vapor deposition). These amorphous films are produced with up to 40 atomic percentage of hydrogen (i.e. they are referred as SiN_x but are really a-SiN_x:H). A subsequent thermal step is needed to activate hydrogenation; in an industrial process, the metal firing step fulfills this objective.

7. *Front contact print and dry:* The requirements for the front metallization are low contact resistance to silicon, low bulk resistivity, low line width with high aspect ratio, good mechanical adhesion, solderability and compatibility with the encapsulated materials. Resistivity, price and availability considerations make silver the ideal choice as the contact metal. Copper offers similar advantages, but due to the following heat treatments its high diffusivity it will produce contamination of the silicon wafer. Screen-printing is used to stick a paste containing silver powder to the front face of the wafer in the comb-like (fingers and bus bars) pattern. The paste is a viscous liquid due to the solvent it contains; these are evaporated in an in-line furnace at 100 to 200 °C. The dried paste is capable for subsequent processing.

8. *Back contact print and dry:* The same operation is done on the backside of the wafer, except that the paste contains silver and aluminum and the printed pattern is different. Al is required because silver does not form an ohmic contact to *p*-Si, but cannot be used alone because it cannot be soldered. The low eutectic temperature of the Al-Si system means that some silicon will be dissolved and then re-crystallize upon cooling in a *p*-type layer.

9. *Co-firing of metal contacts:* A high temperature step is still needed: organic components of the paste have to be burnt off, the metallic grains must sinter together to form a good conductor and it is necessary that they form an intimate electric contact to the underlying silicon.

10. *Testing and sorting:* The illuminated $I - V$ curve of finished cells is measured under a “sun simulator”. Defective devices are then rejected and the rest are classified according to their output.

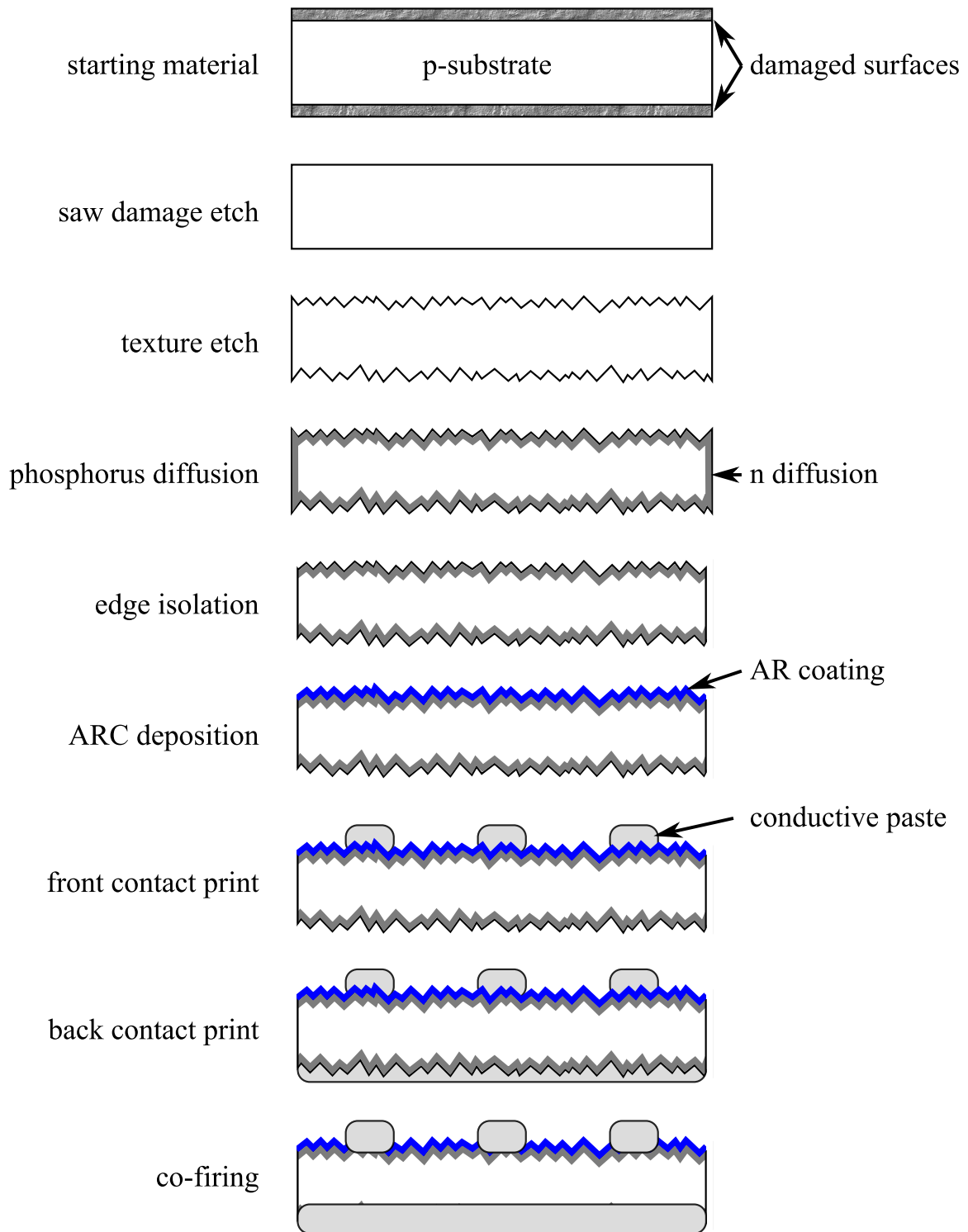


Figure 1.4.: A typical processing sequence with schematic illustrations of the resulting structures. [LH03]

1.3. The solar cell

Semiconductors have the capability to absorb light and convert a portion of the energy of the absorbed photons to carriers of electrical current - electrons and holes. A semiconductor diode separates and collects the carriers and conducts the generated electrical current preferentially in a specific direction. A schematic representation of a p - n junction solar cell is depicted in Figure 1.5. Sunlight is incident from the top on the front of the solar cell. A metallic grid forms one of the electrical contacts of the diode. An anti-reflective layer increases the amount of light transmitted to the semiconductor. The diode's other electrical contact is formed by a metallic layer on the back of the solar cell.

In a direct semiconductor cell, the most of the light is absorbed in a small depth under the surface, where usually the p - n junction is situated. Then the built-in field of the junction immediately separates the positive and the negative excess carriers and forms a voltage at the leads of the cell.

The situation is a bit different for cells made of indirect semiconductors. Those are characterized by a relatively low absorption coefficient for light with photon energy close to the semiconductor band gap. That is why an efficient conversion requires cells with a bigger thickness. The light is absorbed in the semiconductor in a depth of more than a $100\ \mu\text{m}$. It is clear that no junction space charge region can be extended so deep at the usual doping levels in the semiconductor. The carriers are actually generated in the quasi-neutral base region of the cell. There is no electrical or concentration driving force for those. The only way for contribution of those carriers is to diffuse to the junction, where a separation of the minority and majority charge carriers is done. The diffusion of the minority charge carriers to the junction is accompanied by undesired recombination on defects. Those minority charge carriers, which recombine in the base, do not contribute to the cell operation. Such recombination should be avoided to increase the cell efficiency. The undesired recombination is integrally characterized by the charge carrier lifetime of the material, the higher the lifetime, the lower the recombination. A mutual relation between the lifetime and the radiative recombination exists, which will be explained later.

All electromagnetic radiation is composed of photons, which carry specific amounts of energy determined by the spectral properties of their source. The photon energy, E_λ , can be expressed as:

$$E_\lambda = \frac{hc}{\lambda} = h\nu, \quad (1.1)$$

where h is Planck's constant, c the speed of light, and λ and ν the wavelength and frequency

1. Crystalline silicon solar cells

of the photon, respectively. Only photons with sufficient energy to create an electron-hole pair, that is, those with energy greater than the band gap of the semiconductor (for silicon $E_g = 1.12$ eV), will contribute to the energy conversion process.

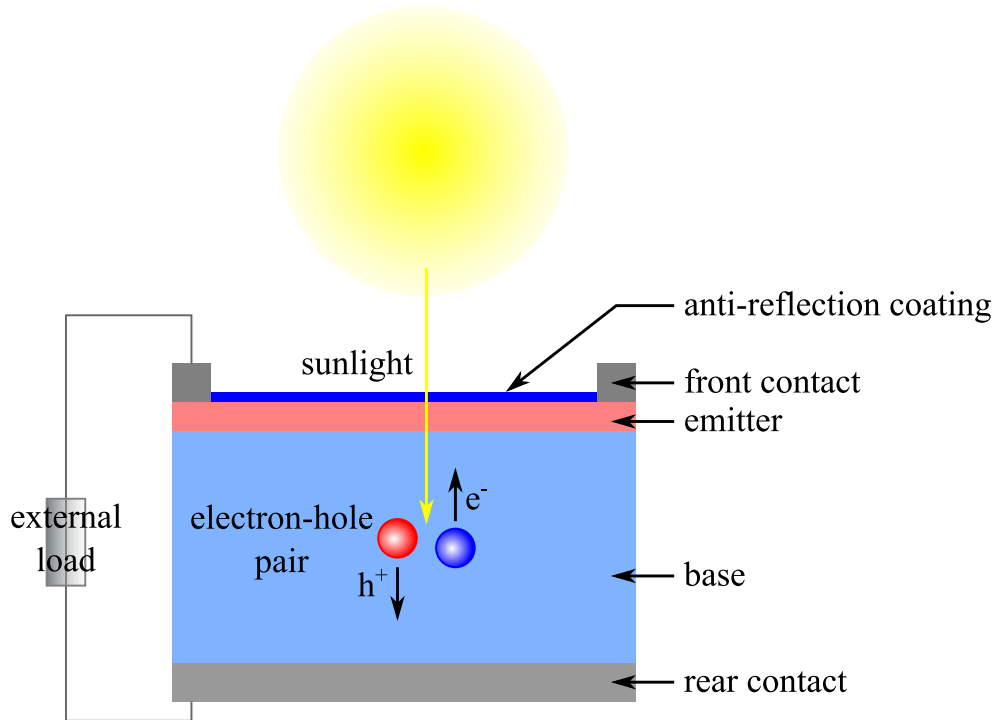


Figure 1.5.: Schematic cross section of a solar cell.

The device (cf. Figure 1.5) consists of a shallow p - n junction formed on the surface, a front ohmic contact, a back ohmic contact that covers the entire back surface, and an anti-reflection coating on the sunny side.

If a solar cell is connected to a load and illuminated, a difference in potential will be produced across the load and current will circulate. The current leaves the cell from the positive terminal and returns to the negative terminal. Under such operating conditions, the cell functions as a generator of electrical energy. The on-going processes inside the cell can be described as follows (cf. Figure 1.6):

- Photons, that reach the interior of the cell and have an energy equal or greater than the band gap, are absorbed in the bulk of the semiconductor generating electron-hole pairs, that work as charge carriers.
- Charge carriers in semiconductors tend, because of their random thermal motion, to move (diffuse) from regions of high concentration to regions of low concentration.

During this diffusion, minority charge carriers can be captured by defective structures in the crystal lattice. The trapped charge carriers recombine at these defects, and thus their possible contribution to the electric current is withdrawn.

- The electric field, or potential difference, produced by the p - n junction is responsible for separating the charge carriers before they have a chance to recombine. The result is a potential difference and current in the external circuit including the load.
- The presence of a potential difference across the terminals of the device produces, as in any device on p - n junctions, the phenomena of injection and recombination of electron-hole pairs. In the solar cell, these amount to losses. The extent of the losses depends on this potential difference.

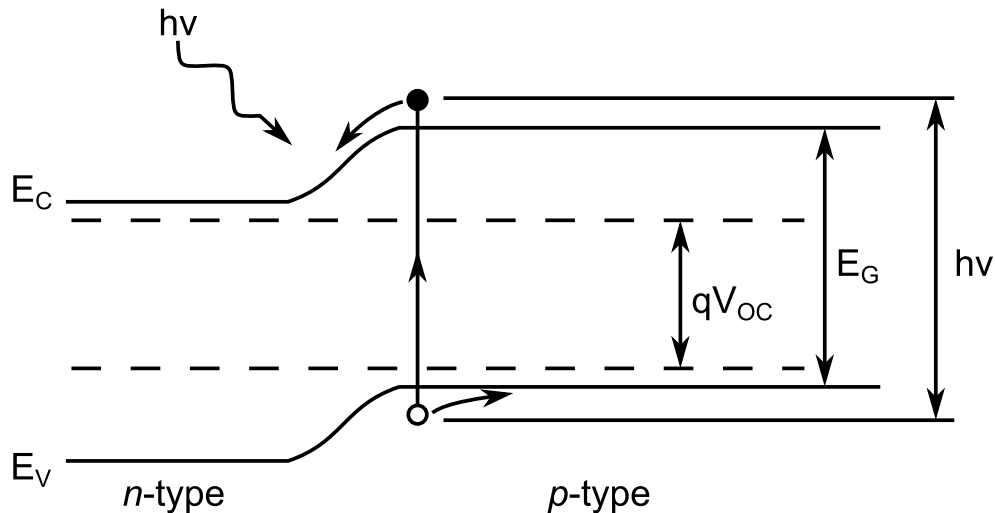


Figure 1.6.: Energy band diagram of a p - n junction solar cell under solar irradiation.

In summary, when a load is connected to an illuminated solar cell the current that flows is the net result of two counteracting components of internal current:

1. The photocurrent, I_L , due to the generation of charge carriers by the light;
2. The dark current, I_D , due to the recombination of charge carriers driven by the external voltage; this voltage is needed to deliver power to the load.

Assuming that, the two currents can be superimposed linearly, and then the current in the external circuit can be calculated as the difference between those two components:

$$I = I_L - I_D(V). \quad (1.2)$$

1. Crystalline silicon solar cells

The main characteristic of a solar cell is the I - V curve. It has several derivative parameters such as I_{sc} (short circuit current), V_{oc} (open circuit voltage) and the maximum possible delivered energy $P_{mp} = V_{mp} \cdot I_{mp}$, as shown in Figure 1.7. The main parameter that determines the solar cell efficiency is the maximum square area (power) as form of multiplication I - V ($P_{mp} = V_{mp} \cdot I_{mp}$), which is a maximum square formed inside the I - V curve as shown in Figure 1.7. The next derivative parameter is the fill factor FF that represents the ration P_{mp} to the product of V_{oc} and I_{sc} :

$$FF = \frac{P_{mp}}{V_{oc} \cdot I_{sc}}. \quad (1.3)$$

The energy-conversion efficiency η can be written as:

$$\eta = \frac{V_{oc} \cdot I_{sc} \cdot FF}{P_{in}}, \quad (1.4)$$

where P_{in} is the total power of light illumination on the cell.

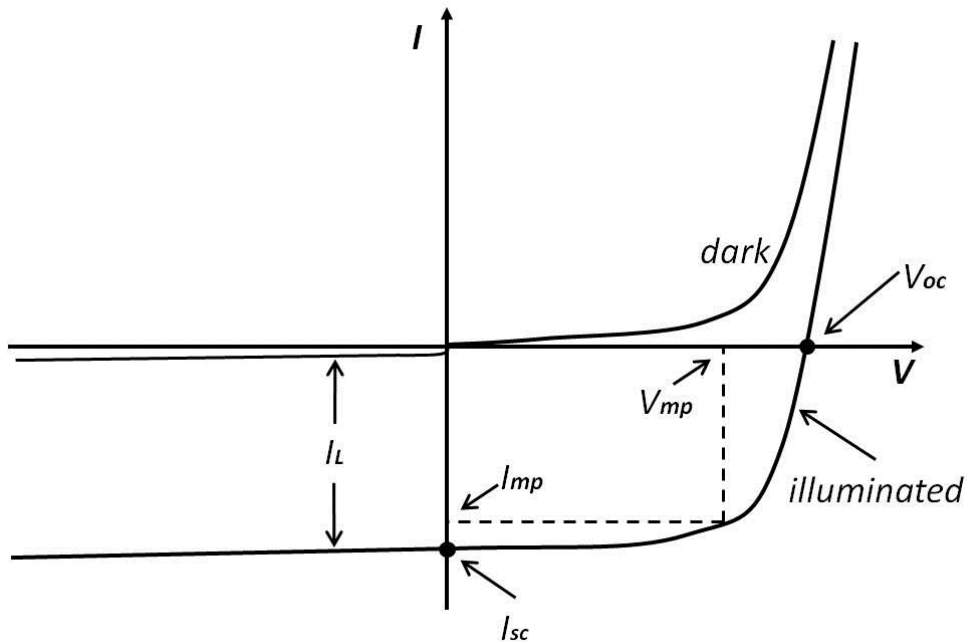


Figure 1.7.: Graph of the I - V characteristic of an ideal solar cell under dark and illuminated conditions.

Cell structure

Silicon has many advantages for application as material in large-scale cell production. It is the second most abundant element in the earth's crust and it is not toxic. Silicon forms an oxide surface layer on air, which fully protects it and prevents further corrosion. The interface between silicon and SiO_2 when grown under clean-room conditions has a very low density of surface states, with a very low surface recombination velocity. With $E_g = 1.12 \text{ eV}$, silicon has a favorable energy gap for the conversion of solar energy. Besides all these advantages, silicon, with its indirect optical transition, has the serious disadvantage of weak absorption. Consequently, silicon must be much thicker than a semiconductor with direct transitions. Moreover, due to the weak absorption the generation of electron-hole pairs is distributed over a large penetration depth $1/\alpha$ of photons and at least one kind of charge carriers must diffuse over a large distance in order to reach the contact. This implies that this charge carrier type must also have a large diffusion length and lifetime. Because of the poor absorption, not only more silicon is needed, but silicon must also have a higher purity than if the optical transitions were direct.

In the usual structure of a solar cell, the contacts are applied to opposite surfaces. For the illuminated surface, a non-transparent contact poses a problem. Metal contacts are therefore arranged in narrow strips, in comb-like structures leaving most of the surface uncovered. The charge must then flow in the membrane layer (emitter) towards the contact strips parallel to the surface. A high doping level is required in this layer to avoid an intolerably large serial resistance. Adjacent to the emitter is a weakly doped absorber region (base) over the greatest part of the solar cell thickness. Since electrons have a greater mobility than holes and thus a greater diffusion length for a given lifetime, they are chosen to be minority charge carriers. Therefore, the base is p -doped and the emitter is strongly n -doped. In order to minimize the loss of electrons by surface recombination at the back contact, a strong p -doped layer may be used in front of the back contact. The reduction of the recombination at the rear contact is commonly attributed to the so-called "back surface field" (BSF; cf. Figure 1.8(a)), originating from the negative charge of the p^+ -doped region, thought to repel the electrons. This repulsion is, however, not recognizable in the total force and the smaller recombination probability is instead due to the reduced concentration of the electrons in the p^+ -layer.

The areas of the front surface without metal contact are covered with a passivating layer, in order to reduce the rate of surface recombination.

Figure 1.8 illustrates for both, a high efficient ($\eta \approx 20\%$) laboratory (FhG-ISE) and

industrial cell the contacting structure mentioned above. [Wür05]

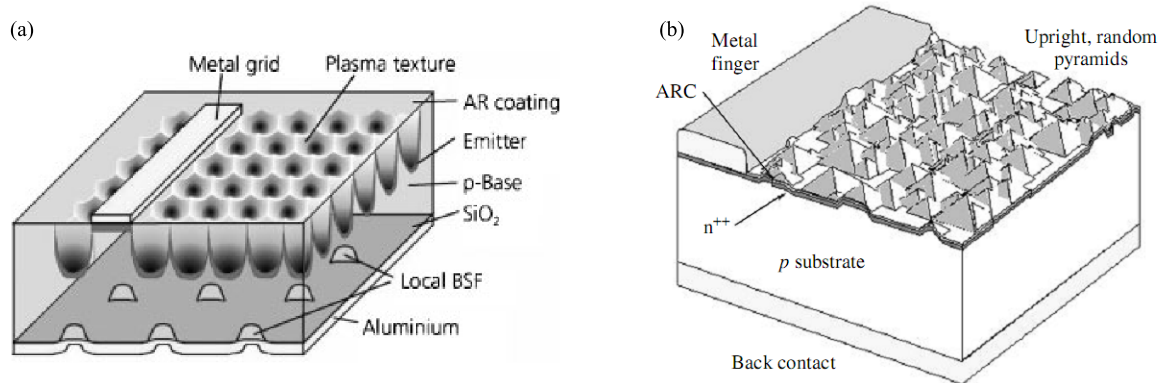


Figure 1.8.: (a) Schematic drawing of a solar cell with plasma textured front surface and wet oxide/LFC rear (FhG-ISE); (b) industrial cell with screen printed contacts. (Not to scale) [SGW04, LH03]

Substrate

Highest efficiencies are achieved with monocrystalline float zone (FZ-Si) material, which in addition to extreme crystalline perfection shows the lowest contamination levels of metallic and electrically neutral impurities. However, this resource is too expensive to use it for mass production.

Industrial cells use either Czochralski (Cz-Si) wafers or multicrystalline substrates. The Czochralski wafers have a perfect crystal structure, but they also contain a lot of oxygen, that affects lifetime in several ways. The drawback of Czochralski growth is its production per hour of about 2 kg/h in comparison to directional solidification of mc-Si of about 7 kg/h. Furthermore, the energy consumption for a Cz puller is three times higher than for directional solidification. Additionally to crystal defects, such as grain boundaries and dislocations, in multicrystalline wafers the content of metallic impurities is higher, because of the lower segregation in the melt during the faster solidification process. As a result, the lifetime of mc-Si is lower than in Cz-Si. Nevertheless, the lifetime is important for the solar cell performance, one can say the higher the lifetime, the higher the efficiency of the solar cell. Final substrate lifetimes of industrial cells range from 10 to 100 μ s. There are several techniques during the manufacturing process to reduce the concentration of lifetime affecting impurities.

The optimum substrate doping depends on the cell structure and the dominant recombination mechanism. It is determined in considerations of two factors: serial resistance and recombination in the base. Intrinsic substrates present the advantage of low Auger recombination. Higher doping favors trap-assisted recombination, because recombination is proportional to the excess charge carrier density, which decreases as doping increases. Furthermore, a high doping lowers the serial resistance losses associated to the transport of charge carriers to the backside in thick cells. The typical doping levels in the substrate are in the range of 10^{16} cm^{-3} .

The choice of the optimum substrate thickness is driven mainly by two factors. The requirement of less material usage per cell leads to a cost efficient production. The thinner cells are mechanically unstable and get broken with a higher probability during the processing. It is clear, that the thicker the cell the less contribution of the surfaces to the cell performance. A careful consideration of the parameters surface recombination, diffusion length and light absorption should be made to get optimal performance from a cell with certain thickness.

Surfaces

At the front surface metal grids are used to collect the photogenerated charge carriers. The compromise between transparency and serial resistance requires metallization techniques to produce very narrow but thick and highly conductive metal lines with low contact resistance to the silicon. Laboratory cells use photolithography and evaporation to form 10 to 15 μm metal fingers from Ti, Pd or Ag. In the industry Ag pastes are screen printed, resulting in $\approx 100 \mu\text{m}$ wide lines. Coarser metallization techniques imply higher shading and resistance losses.

Beneath the metal lines, the substrate has to be heavily doped to make the contact selective to the minority charge carriers. The doped region, the emitter, extends all across the front surface and is acting as a “transparent electrode” by offering the minority charge carriers a low resistance path to the metal lines. Industrial phosphorus emitters, typically, feature surface concentrations over 10^{20} cm^{-3} and 0.4 μm depth, and result in a sheet resistance of around $40 \Omega/\square$. To decrease the front surface recombination, SiN_x passivation layers are used. The back p -contact is usually printed and subsequently fired with an Al paste. A higher p -doped layer would be useful to decrease contact recombination. For high efficient solar devices, contact passivation is essential. Due to the high conductivity of the rear p^+ -layer a metal contact is not required over the entire rear surface. The areas of the

rear surface without metal contact are covered with a passivating layer, silicon dioxide, in order to reduce the rate of surface recombination. The oxide layer is covered by a metal mirror layer that reflects photons not yet absorbed and thus enhances absorption in the cell.

Solar cell light trapping

The cell converts the incident sunlight to electrical power. It is clear, that only the light absorbed in the cell can cause an impact on its efficiency. Light reflected from the cell surface does not contribute to charge carrier generation. Therefore, the reflection of light, capable of carrier generation in silicon, should be minimized.

The reflection from bare silicon-air interface of light in the visible and NIR spectral range is strong. A main reason for this high reflection is the big difference in the refractive indices of air and silicon. Indeed, assuming normal incidence of light on a polished air-silicon interface and applying the Fresnel equation

$$R = \left(\frac{n_{\text{Si}} - 1}{n_{\text{Si}} + 1} \right)^2 \quad (1.5)$$

one obtains a reflection coefficient of $R \approx 9/25$ for a mean refractive index of 4 for the silicon in the visible range. Such high reflection is unacceptable for the practical application and that is why techniques for overcoming that type of losses are developed.

There are two main methods for reflection minimization: First anti-reflection coating and second surface structuring. The anti-reflection coating (ARC) consists of TiO_x or SiN_x . The reflection is at a minimum, when the layer thickness is $n_{\text{ARC}}\lambda_0/4$ (or an odd multiple of it), with n_{ARC} the refractive index of the ARC, and λ_0 the free space wavelength. In case of the solar spectrum $\lambda_0 = 600 \text{ nm}$. The surface structuring is done for an efficient light trapping. The light trapping is realized by a pyramidal surface. Light incident on the side of a pyramid will be reflected onto another pyramid instead of being lost. The reflectivity of bare silicon is reduced from about 35 % for flat surfaces to around 20 % for the textured surface; the addition of an anti-reflection coating reduces the overall reflection to a few percent [Sze81]. There are two ways for structuring: selective etching by alkaline basic solution and enhancement of the sawing marks by means of acidic sour etching.

1.4. Polycrystalline silicon thin film on glass substrate

Polycrystalline silicon on glass solar cells count to the “second generation solar cells”, based on reducing the cost of “first generation solar cells” by employing thin film technologies. Polycrystalline silicon is representative for the transition between crystalline and amorphous silicon, but it is rather comparable to crystalline than to amorphous silicon. Exact statements about the properties are complicated by the fact that they are strongly dependent on the deposition conditions, e.g. ratio of silane to hydrogen, substrate temperature, etc. Several studies were published dealing with these dependences on the structural, electrical and optical properties of polycrystalline silicon [FCH⁺96, CFB⁺97]. A schematic of a polycrystalline silicon solar cell is given in Figure 1.9.

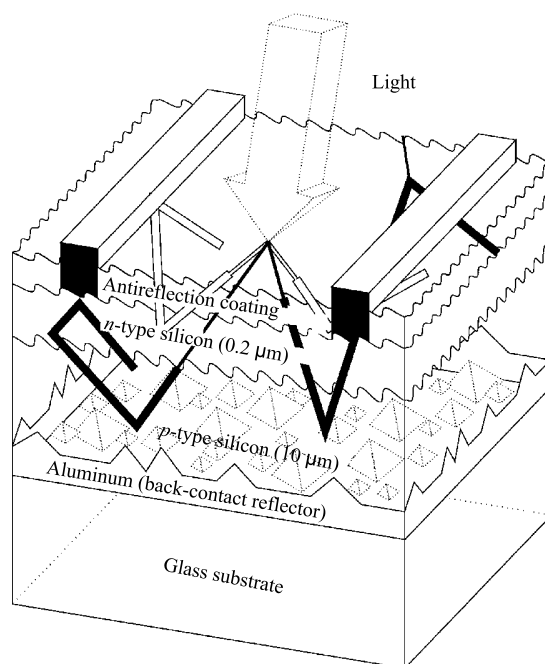


Figure 1.9.: A schematic of a polycrystalline silicon solar cell. [LH03]

The liquid-phase crystallized silicon layers investigated in this work are grown on *Corning Eagle XG*[®] glass substrates. The silicon layers are deposited on whether an amorphous SiC_x or SiO_x layer with a thickness of 250 nm after appropriate substrate cleaning. Next a LPCVD process using silane was employed to deposit an amorphous to nanocrystalline 8 – 13 μm thick absorber layer onto the prepared substrates. Avoiding incorporation of hydrogen into the silicon layer, the deposition temperature was set to 670 °C. No additional doping is provided, because the boron doping is introduced by out-diffusion of boron from

the SiC/SiO layer during zone-melting crystallization. Subsequently, crystallization of the layer was carried out using a line shaped electron beam with a constant scanning speed. The thickness of the silicon layer is about $10\ \mu\text{m}$.

The cell concept combines an a-Si:H(n) emitter deposited at low temperatures with poly-Si absorber layer on SiC/SiO on glass as described before. The thin 20 nm a-Si:H(n) emitter layer was deposited immediately after a HF-dip of the absorber surface. The phosphorous doping was realized by adding phosphine diluted with hydrogen into the silane gas during PECVD at $210\ ^\circ\text{C}$ substrate temperature. A sputtered layer of Al-doped ZnO serves as transparent front electrode and anti-reflection coating. The buried back contact is established by mesa-etched trenches about $4/5$ of layer thickness in depth. Electrical connections are made by e-beam evaporated aluminum as a grid and as trench rear contact, structured by a photolithographic lift-off process. [AMS⁺11, SAA⁺11]

2. Defects and recombination processes in silicon

In this chapter, defects in silicon crystals and recombination processes in silicon are described. According to the recombination paths at crystal defects, both of these topics are set together.

2.1. Defects

In an ideal crystal lattice, every atom is arranged in an ordered, exactly repeating pattern extending in all three spatial dimensions. However, in reality, deviations from the ideal structure occur. Those deviations are called defects. The types and structures of those defects may have a profound effect on the mechanical, electrical and optical properties of the material. In this section, the most common defects in (multi-) crystalline silicon will be discussed. A scheme of some defects is given in Figure 2.1.

Crystal lattice defects are usually classified according to their dimensions: (*i*) zero-dimensional defects, also called point defects like vacancies, interstitial and substitutional atoms; (*ii*) one-dimensional defects, which include all kinds of dislocations; (*iii*) two-dimensional defects like stacking faults and grain boundaries; (*iv*) three-dimensional defects like voids and precipitates.

2.1.1. Point defects

Point defects are classified into intrinsic point defects and extrinsic point defects. Intrinsic point defects in silicon are vacancies and self-interstitial atoms. Extrinsic point defects are impurity atoms either at a lattice site (substitutional) or at an interstitial site of the lattice. Typical extrinsic point defects in silicon are doping atoms like boron or phosphorus, transition metals, interstitial oxygen and substitutional carbon.

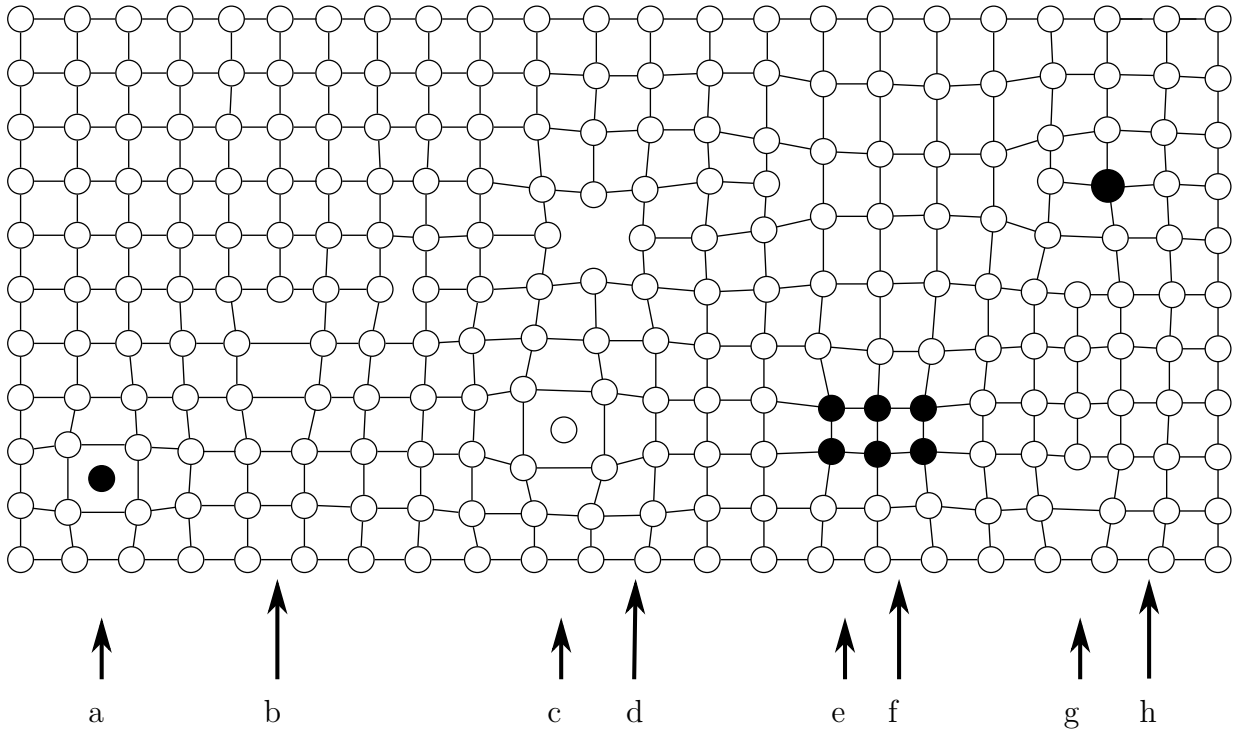


Figure 2.1.: Defects: (a) Interstitial impurity atom, (b) Edge dislocation, (c) Self interstitial atom, (d) Vacancy, (e) Precipitate of impurity atoms, (f) Vacancy type dislocation loop, (g) Interstitial type dislocation loop, (h) Substitutional impurity atom. [FK76]

Types

The simplest point defect in a crystal is a vacancy, a missing atom at a given atomic position. If an atom occupies a site in the crystal structure at which there is usually not an atom, an interstitial defect is formed. An interstitial atom, which has the same chemical species as the crystal, is called self-interstitial. A nearby pair of a vacancy and an interstitial is called Frenkel defect or Frenkel pair. This is caused when an atom moves into an interstitial site and creates a vacancy.

If an atom site is populated with an atom of different chemical species, an impurity is present. Impurities can also sit on an interstitial position. There are two different types of substitutional defects: Isovalent substitution and aliovalent substitution. Isovalent substitution means that the number of valence electrons is the same as for the original atom; it quasi fits into the bonding scheme. Aliovalent substitution means that the number of valence electrons of the substituting atom is different as for the original atom. The impurity adds extra (negative or positive) charge to the crystal bonds, which is compensated by the

extra, locally fixed charge in the nucleus. This mechanism is discussed in detail in the context of doping (1.1).

Noteworthy impurities are also nitrogen, oxygen and carbon, as well as transition metals like interstitial iron. These are discussed in the context of impurities (1.1).

Point defects can cluster. A void is equivalent to a large number of clustered vacancies. Clustered impurities are called precipitates.

2.1.2. Extended defects

Dislocations

Dislocations are line defects, where the crystal lattice is shifted by a certain amount. The vector along the dislocation line is called line vector \vec{L} . A closed path around the dislocation core differs from that in an ideal crystal. The difference vector is called the Burger's vector \vec{b} . Dislocations for which the Burger's vector is a vector of the lattice are called *full* dislocations, whereas dislocations with Burger's vector that are not translation vectors of the lattice are called *partial* dislocations. [Gru10]

Edge dislocations For an edge dislocation, \vec{b} and \vec{L} are perpendicular to each other. An extra half-plane spanned by \vec{L} and $\vec{b} \times \vec{L}$ is inserted (cf. Figure 2.2 (a)).

Screw dislocations For a screw dislocation, \vec{b} and \vec{L} are collinear. The solid has been cut along a half-plane up to the dislocation line, shifted along \vec{L} by the amount \vec{b} and reattached (cf. Figure 2.2 (b)).

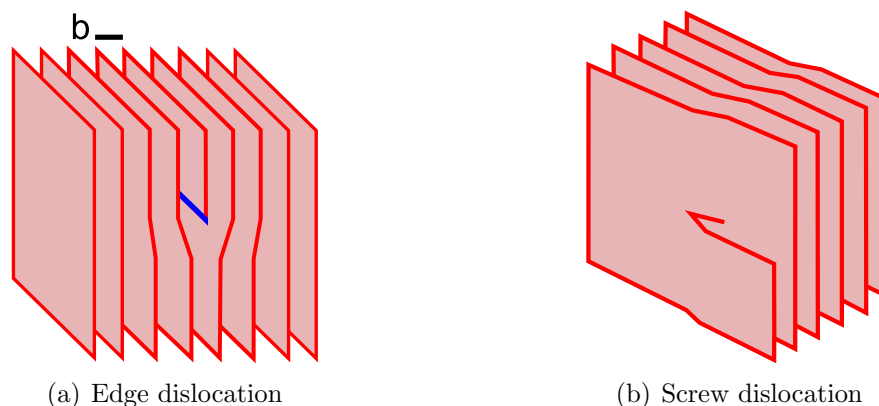


Figure 2.2.: Schematic of an edge dislocation (a) and a screw dislocation (b).

60° dislocations Due to the two-atomic basis of the diamond structure of silicon, two types of 60° dislocations can be constructed; one in the *glide set*, the other in the *shuffle set*, depending at which base the cut is done (cf. Figure 2.3). [HL82]

Usually 60° dislocations dissociate into partials to lower the system energy, resulting in 90° and 30° partials bounding a stacking fault ribbon between them [DBP10].

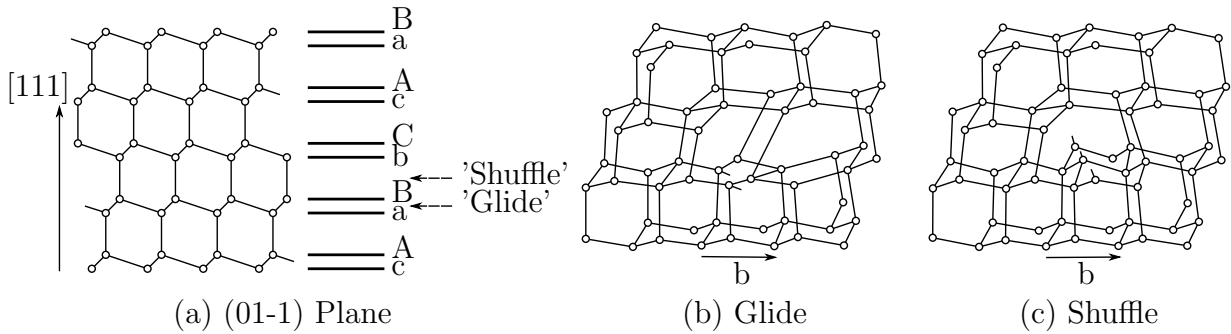


Figure 2.3.: (01-1) plane in silicon showing the stacking sequence and glide planes (a), and perfect 60° dislocations of the glide set (b) and the shuffle set (c).

Partial dislocations As mentioned before, partial dislocations are a result of the dissociation of 60° dislocations (cf. Figure 2.4). Partial dislocations are defined as dislocations which Burger's vector \vec{b} is not a translation vector of the lattice.

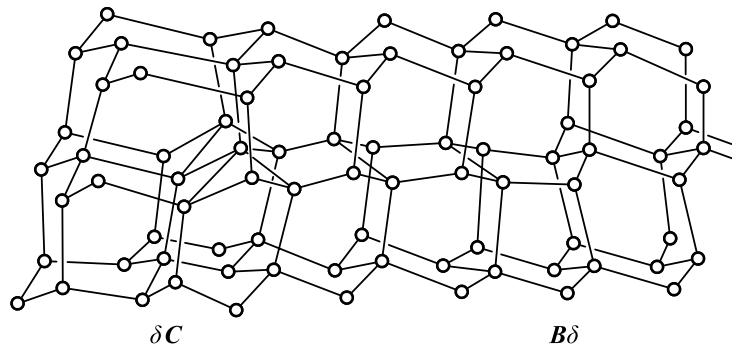


Figure 2.4.: Dissociation of a perfect 60° glide dislocation into 30° (δC) and 90° ($B\delta$) partials. [HL82]

2- and 3-dimensional defects

Stacking faults Ideal stacking of (111) planes in the diamond structure of silicon, $AaB-bCcAaBbCc\dots$, can be disturbed in various ways and creates planar defects. If one plane is

missing, an intrinsic stacking fault is present. If an additional plane is present, the defect is called extrinsic stacking fault. An extended stacking fault in which the stacking is reversed is called twin lamella. If two regions have inverted stacking order, they are called twins and their joint interface is called twin-boundary.

Grain boundaries Grain boundaries occur where the crystallographic direction of the lattice abruptly changes. This happens when two crystals begin growing separately and then meet. Grain boundaries are defined at least by five parameters, three rotational angles to describe how the orientation of grain II results from grain I and two parameters to define the boundary plane of the two grains in the coordinate system of reference grain I. Such defects can have a large impact on the electric properties. They can act as barriers for transport or as carrier sinks. The two crystal grains meet each other with a relative tilt and/or twist. Figure 2.5 shows it schematically.

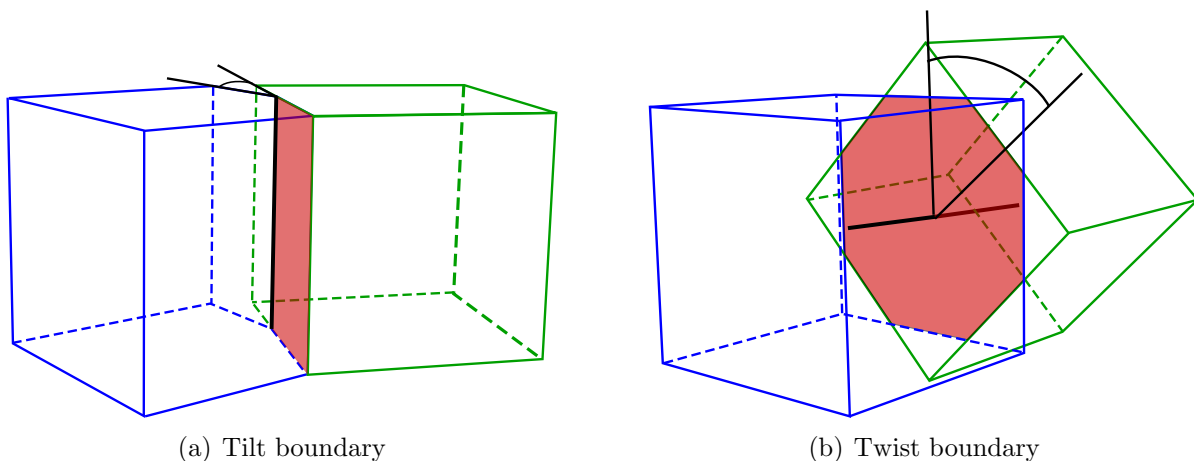


Figure 2.5.: Illustration of a tilt (a) and a twist (b) boundary.

Precipitates Precipitates are agglomerates of extrinsic and/or intrinsic point defects. Such agglomeration occurs when the concentration of point defects is above the solubility limit at a certain temperature. The point defects begin to form nuclei either at an existing defect (heterogeneous nucleation) or through clusters formed due to local fluctuation of the point defect concentration (homogeneous nucleation). The sequence of precipitation is characterized by nucleation, growth in which excess atoms diffuse to precipitates and Ostwald ripening in which a growth competition exists where large precipitates grow at the expense of small ones.

Carbon is a common substitutional impurity. Like silicon, it has four valence electrons and is therefore electrically neutral. The carbon atom is smaller than the silicon atom and may therefore be involved in precipitation of species expanding the lattice like silicon oxide. In metallurgical grade (mg) silicon, carbon is present at levels above the solid solubility limit and SiC precipitates are commonly present. In electronic grade (eg) silicon, the concentration of carbon is low. However, in contact with the crucible and the carbon-rich atmosphere (graphite), it is difficult to avoid contamination of the melt. [LH03]

Oxygen in solid solutions is electrically inactive and predominantly enters interstitial sites. On cooling, super saturation is easily obtained and oxygen precipitates at a rate that depends on oxygen content, temperature, and time at temperature and nucleation sites. Carbon is also found to influence the precipitation of silicon oxides, possibly because the carbon atom reduces the expansion of the lattice when silicon oxide is growing. By heat treatments, the distribution of oxide particles may change since particles may be dissolved when heated and grow when cooled. Oxygen atoms are found to change the effect of other impurities, a process known as internal gettering. One important oxygen source is the crucible. Silicon is melted in high-purity-fused quartz (SiO_2) crucibles or quartz crucibles coated with high-purity Si_3N_4 . If holes appear in the coating, quartz will dissolve in the melt and raise the level of oxygen in the solid. [LH03]

Except for copper, which forms Cu_3Si particles when cooled, the other 3d metals form MeSi_2 precipitates. Investigations of crystallographic structure, morphology and composition of several transition-metal precipitates in silicon identify crystalline silicides, FeSi_2 , CoSi_2 , NiSi_2 , as compounds that influence the minority charge carrier's diffusion length. The morphology and density depend upon temperature and time at temperature. Elements having a high diffusivity like Ni and Cu precipitate easily. This reduces the number of atoms in solid solution and may therefore change the electric properties. [LH03]

2.2. Recombination processes

In standard bulk silicon, the probability of phonon-assisted radiative band-to-band recombination is very small. The electron-hole pairs recombine primarily non-radiative. In standard multicrystalline silicon solar cells, many defects are present. These defects offer an additional way for radiative and non-radiative recombination. Radiative recombination processes and their temperature behavior have an increased significance, because they are an instrument to execute a non-destructive and contactless characterization method,

luminescence experiments. Whereas the non-radiative recombination processes are representative for the concentration of excited charge carriers and influences accordingly the efficiency of radiative processes. Figure 2.6 depicts some recombination processes, (a) shows band-to-band recombination, where the energy can be exchanged to a radiative or an Auger process and (b) shows non-radiative Shockley-Read-Hall recombination.

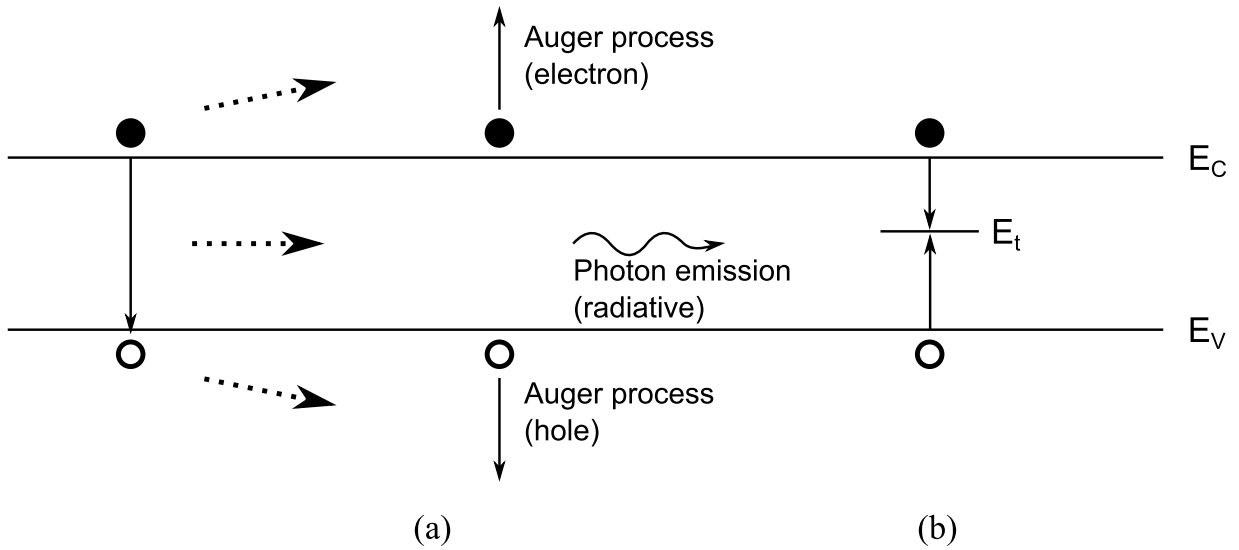


Figure 2.6.: Recombination processes. (a) Band-to-band recombination. Energy is exchanged to a radiative or Auger process. (b) Recombination through single level traps (nonradiative).

2.2.1. Radiative recombination

A recombination process in a semiconductor consist the annihilation of a conduction band electron and a valence band hole. According to that, the recombination rate R should be proportional to the concentration of electrons n and to the concentration of holes p . The recombination rate is then:

$$R = -\frac{dn}{dt} = -\frac{dp}{dt} = Bnp. \quad (2.1)$$

Absorption of light or current injection leads to the creation of excess charge carriers in the semiconductor. The concentrations of electrons and holes can be written as:

$$\begin{aligned}n &= n_0 + \Delta n, \\p &= p_0 + \Delta p,\end{aligned}$$

where n_0 and p_0 are the equilibrium concentrations, and Δn and Δp are the concentrations of the excess charge carriers. Usually the excitation of the charge carriers is done in a way that the concentrations of both types are equal $\Delta n = \Delta p$. The recombination rate can be regarded as a sum of equilibrium R_0 and excess ΔR recombination rates:

$$R = R_0 + \Delta R. \quad (2.2)$$

In a p -type semiconductor with majority charge carrier's concentration $p_0 \gg n_0$ the recombination rate of the excess charge carriers is given by:

$$\Delta R = B(n_0 + \Delta n)(p_0 + \Delta p) - Bn_0p_0 = B(n_0 + p_0)\Delta n + B\Delta n^2. \quad (2.3)$$

In case of low injection ($\Delta n \ll p_0$), the term with Δn^2 can be neglected and the rate of recombination becomes linearly dependent on the injected charge carrier concentration:

$$\Delta R = B(n_0 + p_0)\Delta n. \quad (2.4)$$

This equation is called the “monomolecular” rate equation. This held, if the injected charge carriers are negligible in comparison to the concentration of majority charge carriers. At high injection ($\Delta n \gg p_0$) the Δn^2 term gets dominant, and thus:

$$\Delta R = B\Delta n^2. \quad (2.5)$$

That is the “bimolecular” rate equation and B denotes the recombination coefficient.

In the event of radiative recombination, B is related to the intensity of the emitted radiation. It can be theoretically evaluated by the detailed balance principle [vRS54]. Under the terms of this principle, the rate of radiative recombination at thermal equilibrium in an elementary frequency interval $d\nu$ at frequency ν is equal to the corresponding rate of generation of electron-hole pairs by thermal radiation. The generation rate can then be defined by the spectral photon density in the semiconductor $\rho(\nu)$, which is determined by

Planck's law:

$$\rho(\nu)d\nu = \frac{8\pi\nu^2}{c^3} \frac{n^2 \left[\frac{d(n\nu)}{d\nu} \right]}{\exp\left(\frac{h\nu}{kT}\right) - 1} d\nu, \quad (2.6)$$

and the probability at which photons are absorbed in the semiconductor. The absorption probability is given by the product of the group velocity of light $v_g = \frac{c d\nu}{d(n\nu)}$ and the absorption coefficient α of the semiconductor. Thus, $R(\nu)d\nu$ becomes:

$$R(\nu)d\nu = \frac{8\pi\alpha n^2}{c^2} \frac{\nu^2}{\exp\left(\frac{h\nu}{kT}\right) - 1} d\nu, \quad (2.7)$$

where n is the refractive index of the semiconductor, and c , h and k are the speed of light, Planck's and Boltzmann's constants, respectively. The radiative recombination coefficient can now be given as:

$$B = \frac{R}{n_i^2}, \quad (2.8)$$

in which R is defined as the integral of Equation 2.7: $R = \int_0^\infty R(\nu)d\nu$ [vRS54, Var67] and n_i is the intrinsic carrier concentration ($n_i^2 = n_0 p_0$ for thermal equilibrium). For intrinsic silicon at $T = 300$ K the radiative recombination coefficient is given by [TGW⁺03]: $B = 4.73 \cdot 10^{-15} \text{ cm}^3 \text{ s}^{-1}$.

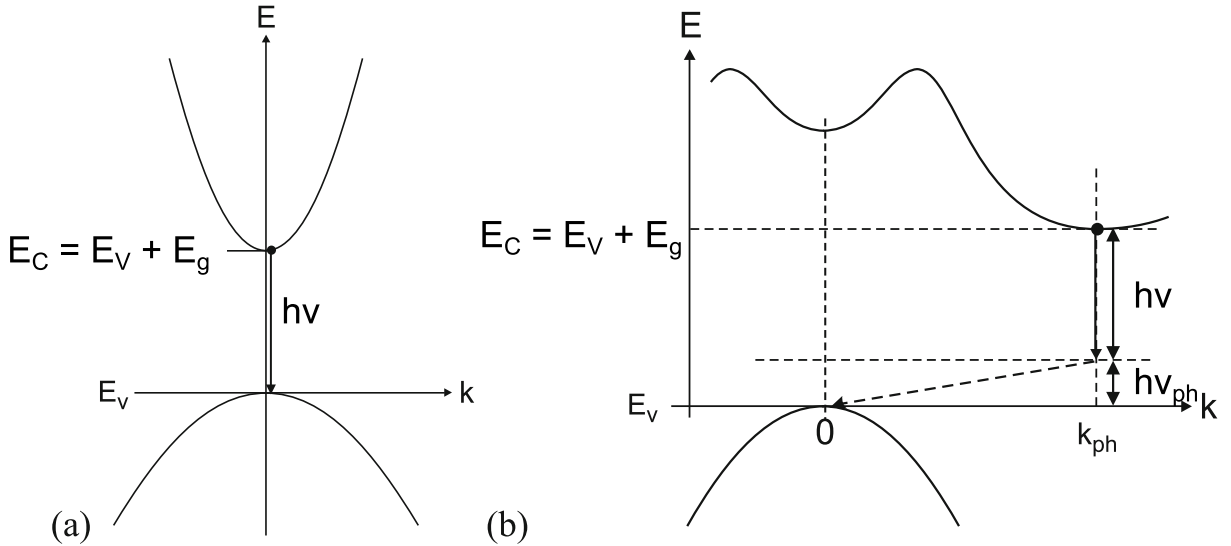


Figure 2.7.: (a) Direct optical transition and (b) indirect optical transition between valence and conduction bands. The photon energy is $h\nu$. The indirect transition involves a phonon with energy $h\nu_{ph}$ and wavevector k_{ph} .

In an indirect-gap semiconductor as silicon, all occupied upper states connect to the empty lower states. Nevertheless, the transition must be mediated by an intermediate process that conserves momentum (cf. Figure 2.7 (b)). Phonon emission is the most likely intermediate process. An optical transition assisted by phonon emission occurs at a lower photon energy than the gap energy, $h\nu = E_g - h\nu_{ph}$.

Additionally, in practice, electrons and holes reside slightly above and below their band edges E_C and E_V respectively, due to thermal energy when the temperature is above absolute zero. As a result, the photon energy emitted would be slightly larger than the band gap energy. Here, the spectrum of the spontaneous emission is analyzed. Near the band edges, the energy of the emitted photons is governed by the relationship

$$h\nu = \left(E_C + \frac{\hbar^2 k^2}{2m_e^*} \right) - \left(E_V + \frac{\hbar^2 k^2}{2m_h^*} \right) = E_g + \frac{\hbar^2 k^2}{2m_r^*}. \quad (2.9)$$

The above is called the joint dispersion relation and m_r^* is the reduced effective mass

$$\frac{1}{m_r^*} = \frac{1}{m_e^*} + \frac{1}{m_h^*}. \quad (2.10)$$

With similar treatment, a joint density of states can be obtained [Sch06b]

$$N_J(E) = \frac{(2m_r^*)^{3/2}}{2\pi^2\hbar^3} \sqrt{E - E_g}. \quad (2.11)$$

The distribution of carriers is governed by the Boltzmann distribution

$$F(E) = \exp\left(-\frac{E}{kT}\right). \quad (2.12)$$

The spontaneous emission rate is proportional to the product of Eqs. 2.11 and 2.12, and it generally has the form [Sch06b]

$$I(E = h\nu) \propto \sqrt{E - E_g} \exp\left(-\frac{E}{kT}\right). \quad (2.13)$$

The essence of Eq. 2.13 is depicted in Figure 2.8. The spectrum of spontaneous emission has a threshold energy of E_g , a peak of $(E_g + 1/2kT)$, and a half-power width of $1.8kT$.

Thus, one can say that the peak photon energy of the band-to-band radiative transition

in an indirect-gap semiconductor is

$$E = E_g + \frac{kT}{2} - h\nu_{ph}. \quad (2.14)$$

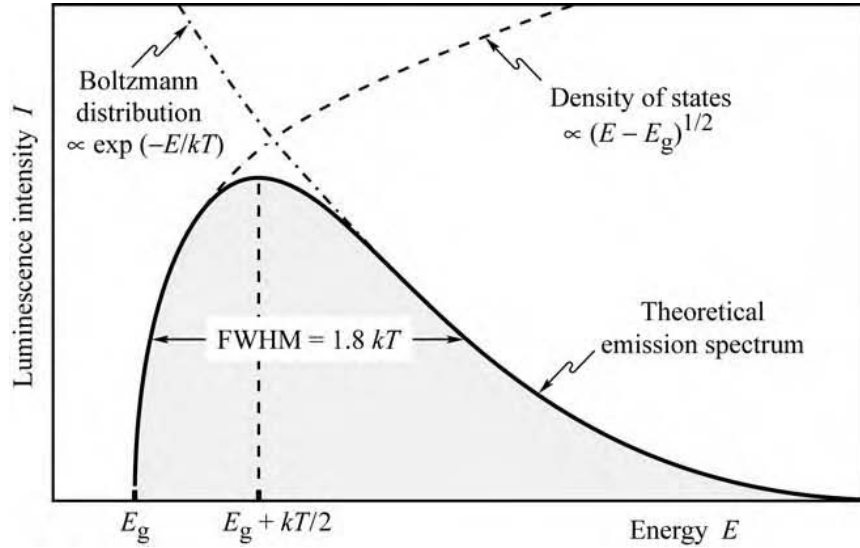


Figure 2.8.: Theoretical spectrum of spontaneous emission. (After [Sch06b].)

2.2.2. Defect-related radiation

As mentioned above (2.1), multicrystalline silicon has plenty of defects. Some of them can be observed by photoluminescence spectroscopy, but others are observable by electroluminescence spectroscopy only. Using photoluminescence and forward-biased electroluminescence, besides the band-to-band transition, subband-gap luminescence can be monitored. Using reverse-biased electroluminescence on the contrary, a different kind of luminescence, namely pre-breakdown luminescence, can be detected. In the following, these types of luminescence are described.

Subband-gap luminescence

Subband-gap luminescence was first addressed by Drozdov et al. [DN76], who found that at liquid helium temperature (4 K) dislocations in silicon give rise to four photoluminescence lines labeled D1 (0.812 eV), D2 (0.875 eV), D3 (0.934 eV), and D4 (1.000 eV). A typical photoluminescence spectrum of dislocated silicon at 80 K is shown in Figure 2.9.

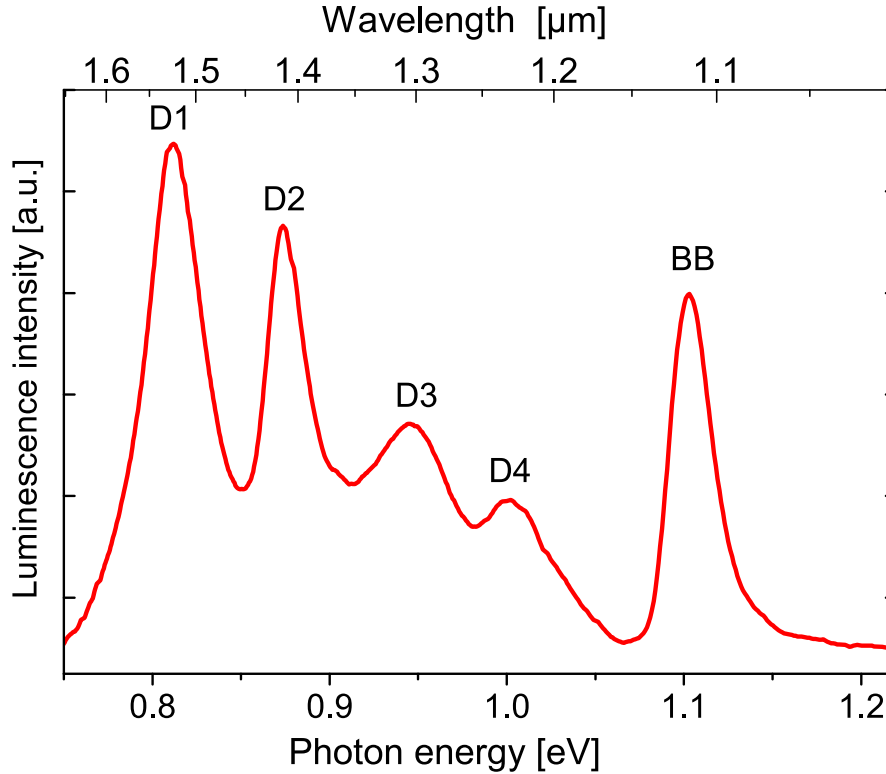


Figure 2.9.: Typical spectrum obtained from plastically deformed silicon at 80 K. Dislocation lines (D1 - D4) and band-to-band (BB) radiation. [Arg07]

Narrow emission lines indicate bound states, which could be motivated for charge carriers at dislocations by following factors:

- mechanical strain or long-range electrical interaction
- dangling bonds, structural imperfections and defects in the dislocation core
- impurities and defects close to the dislocation

Sauer et al. [SWS⁺85] concluded, that the lines D1 - D4 are related to “relaxed” dislocations. Sekiguchi et al. [SKS94, SS96] observed D3 and D4 along slip lines, while D1 and D2 were found at intersections of plural slip lines. They showed that Lomer-Cottrell dislocations and jogs act as recombination centers for D1 and D2 emission. Mchedlidze et al. [MKA⁺09] suggested that screw dislocations are responsible for D1 and D2 peaks, whereas edge dislocations are responsible for D3 and, probably, for D4 peaks. Furthermore, there is a wide set of investigations (e.g. [TTW95, PLB⁺04, IST⁺08, BFM12, TIO⁺12]) that

suggest that oxygen precipitates, thermal donors and dislocations are capable of supporting an origin for emission in the 0.7 – 0.9 eV region.

Pre-breakdown luminescence

In mc-Si solar cells, three types of breakdown appearing in different reverse bias ranges are known so far. Between -4 and -9 V “early breakdown” (type 1) occurs, which is induced by aluminum contamination at the wafer surface. Between -9 and -13 V “defect-induced breakdown” (type 2) dominates. This breakdown site is attributed to metal-containing precipitates lying within recombination active grain boundaries. Beyond -13 V, “avalanche breakdown” (type 3) can be found. It is supposed, that this breakdown type occurs at etch pits produced during the cell process. [BBB⁺11]

2.2.3. Non-radiative recombination

The non-radiative recombination processes, which are described here, are the Shockley-Read-Hall (SRH), multi-phonon and Auger recombination processes.

Shockley-Read-Hall recombination

In spite of all improvements, there are several impurity atoms or crystal defects in the final wafer. Few of them can be electrically active, causing levels in the band gap. Thereby, the impurities appear as recombination active centers or traps for the minority charge carriers in the semiconductor (cf. Figure 2.6(b)). The recombination rate, caused due to their presence, is given by [SR52, Hal52]:

$$R_{SRH} = \frac{np - n_i^2}{\tau_p(n + n_0) + \tau_n(p + p_0)}. \quad (2.15)$$

In Equation 2.15, n and p denote concentration of electrons and holes; n_i^2 is the intrinsic charge carrier concentration. The lifetime for electrons, when the centers are completely empty, is given by τ_n , and τ_p is the hole lifetime with all centers occupied by electrons. They relate to the density of recombination centers N_t , their capture cross section for electrons σ_n and holes σ_p , and the thermal velocity of the carriers $v_{th,n}$ and $v_{th,p}$ ($\approx 10^7$ cm/s for silicon), respectively:

$$\tau_n = \frac{1}{\sigma_n v_{th,n} N_t} \text{ and } \tau_p = \frac{1}{\sigma_p v_{th,p} N_t}. \quad (2.16)$$

The recombination centers lie at an energy level defined by n_0 and p_0 , which are the equilibrium electron and hole concentrations, when the Fermi level coincides with the energetic position of the recombination center E_t in the band gap:

$$n_0 = N_C \exp\left(\frac{E_t - E_C}{kT}\right) \text{ and } p_0 = N_V \exp\left(\frac{E_V - E_t}{kT}\right). \quad (2.17)$$

N_C and N_V are the effective density of states for conduction band and valence band, respectively, k is Boltzmann constant and T stands for the temperature. E_C and E_V indicate the conduction band and valence band energy, respectively.

At low injection, the SRH recombination is usually the main mechanism in silicon. In doped materials, the change of the concentration of majority charge carriers due to injection can be neglected. The contribution in the total recombination due to the SRH part can be simplified to:

$$\Delta R_{SRH} = \frac{\Delta n}{\tau_{SRH}}, \quad (2.18)$$

where τ_{SRH} is the lifetime of the minority charge carriers and Δn their concentration.

Auger recombination

In case of high majority charge carrier or doping concentration, the Auger process becomes the predominant recombination mechanism in elemental semiconductors. The Auger recombination is a three-particle process: an electron and a hole recombine in a band-to-band transition and the released energy is immediately absorbed by another electron or hole (cf. Figure 2.6(a)). The expression for the total recombination rate is dependent on the concentration of all three species participating in the recombination:

$$R_{Auger} = C_{eeh}n^2p + C_{ehh}np^2, \quad (2.19)$$

in which C_{eeh} and C_{ehh} stand for the electron-electron-hole and electron-hole-hole recombination mechanism, correspondingly. Both coefficients depend slightly on the temperature [DS77] (Table 2.1) and are not influenced by presence of impurities.

T	77 K	300 K	400 K
$C_{eeh} \text{ cm}^6\text{s}^{-1}$	2.3×10^{-31}	2.8×10^{-31}	2.8×10^{-31}
$C_{ehh} \text{ cm}^6\text{s}^{-1}$	7.8×10^{-32}	9.9×10^{-32}	1.2×10^{-31}

Table 2.1.: Auger coefficients for e-e-h and e-h-h process at different temperatures. [DS77]

A large number of Auger processes can occur, depending on the charge carrier concentration and the nature of the possible transitions [Pan75].

3. Experimental methods

3.1. Scanning photoluminescence

The experimental setup for the conventional scanning photoluminescence (scanning PL) system is given in Figure 3.1. The excitation beam is given by an optical pumped solid-state laser of the *Verdi G* series from *Coherent*. The excitation light has a wavelength of 532 nm and a maximum output power of 2 W. The beam passes a heat-blocking filter, F_1 , so that no IR radiation of the source will reach the detection system. To use the lock-in technique, the laser beam is modulated by a chopper. The exciting beam is directed perpendicular to the sample surface and is focused to a spot of about $100\ \mu\text{m}$. The focusing parabolic mirror (focal length 12 cm) is used as a collecting mirror for the luminescence signal as well. A long-pass filter, F_2 , blocks light with wavelengths lower than 800 nm, such as reflected and scattered excitation light. The luminescence is spectral resolved by a monochromator (*HR 640 Jobin Yvon*) equipped with a 300 grooves/mm grating and blazed at 1300 nm. The spectral resolution is 5 nm.

A liquid nitrogen cooled germanium p-i-n diode (*North coast L*) is used for detection. The detector is sensitive in the wavelength range $0.8 - 1.8\ \mu\text{m}$. The 5 ms response time of the detector needs a modulation frequency of 33 Hz. The integration constant of the lock-in is usually set to 30 ms. The sample-holder (cryostat) is mounted on motorized x - y -positioning stage, thus maps can be scanned.

3.2. Luminescence imaging

Nowadays, two luminescence imaging techniques to characterize silicon solar cells exist. Fuyuki et al. [FKY⁺05] reported first on a photographic survey of minority charge carrier diffusion length in solar cells by electroluminescence. Electroluminescence measurements can be performed at finished, fully contacted and isolated solar cells only. Furthermore, electroluminescence can be applied easy on whole modules. Another approach is the pho-

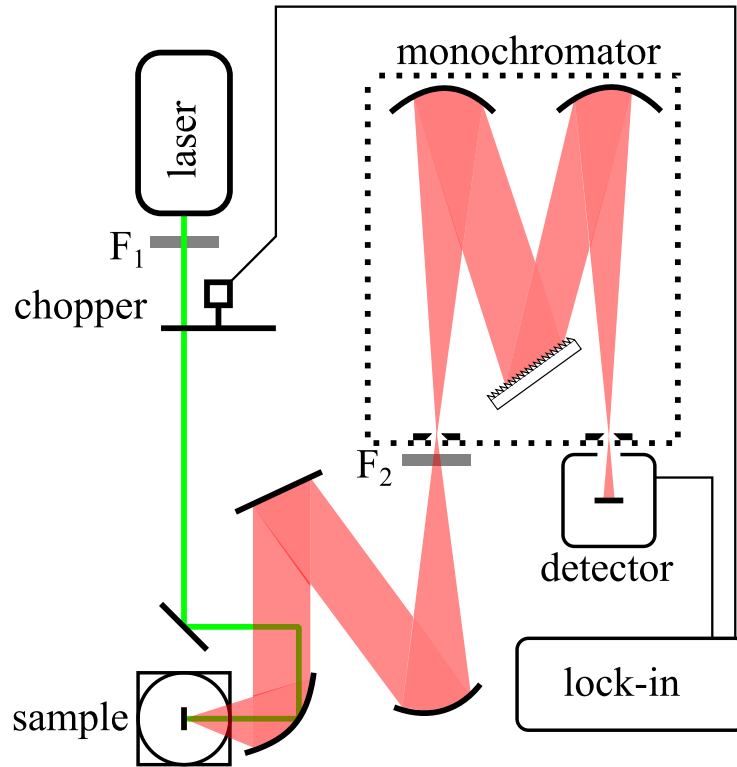


Figure 3.1.: Scheme of the scanning photoluminescence and spectroscopy apparatus.

toluminescence imaging. Here, the minority charge carriers are not excited by an external forward voltage and current but by photons. Trupke et al. [TBA05, TBSW06, TBA⁺06] reported first on photoluminescence imaging. Due to the excitation by light, photoluminescence measurements do not require any electrical contacts at the solar devices. Electroluminescence and photoluminescence imaging are extremely fast spatially resolved characterization techniques for large silicon wafers.

Trupke et al. introduced a method to convert relative photoluminescence or photoconductance signals into an absolute excess charge carrier concentration, which should simplify photoluminescence lifetime measurements. However, they could investigate wafers with a silicon nitride passivation layer after chemical polishing only. In their experiments, they used a cooled CCD camera and reached resolutions up to $130\ \mu\text{m}$ at an exposure period of 1 s - 5 s for band-to-band luminescence images. Haunschild et al. [HGKR09] made photoluminescence images in 300 ms of a $156 \times 156\ \text{mm}^2$ wafer with a resolution of $320\ \mu\text{m}$, though they only made band-to-band luminescence images after emitter diffusion.

Schubert et al. [SGT⁺08] applied a camera-based photoluminescence spectroscopy method for fast measurements, but they also had to passivate the mc-Si samples for their analysis.

They detected mainly D2- and as well, D1- and D3-bands, because they used a relatively broad band-pass filter around 1465 nm. They analyzed an $15 \times 15 \text{ mm}^2$ sample, which was cooled down to 78 K. Trupke et al. [TBA⁺07] mentioned that the defect-related luminescence signal prior to silicon nitride firing is too weak to yield acceptable signal to noise ratios with data acquisition times of $< 10 \text{ s}$ and low illumination intensities. Nevertheless, on the other hand they investigated string ribbon wafers, which is today not state of the art material for solar cells. Nowadays, solar grade material is mc-Si and umg-Si, grown by directional solidification, which can be characterized for defect-related luminescence at room temperature and comparatively low illumination intensity.

I performed photoluminescence imaging experiments by means of two different approaches for sample illumination: in a first experiment, using a pulsed laser system, a previous setup [SMA⁺11b] was optimized to yield band-to-band and defect-related luminescence images from whole solar wafers, originating from different stages of the production process of standard silicon solar cells. In a second experiment, I investigated the applicability of highly intense LEDs for photoluminescence imaging of whole wafers, especially for defect-related luminescence. These methods are briefly described in [SMA⁺11a]. Figure 3.2 depicts band-to-band (a) and defect-related (b) luminescence images with a resolution of about $50 \mu\text{m}$ and a recording time of a few seconds. The sample in this images was excited by laser. For comparison Figure 3.2(c) shows a photoluminescence map at 0.8 eV with a resolution of $50 \mu\text{m}$ at room temperature. The recording time for the photoluminescence map was about 13 hours.

Further development of the LED-based system yielded to a setup which is illustrated in Figure 3.3(a). The first setup of this type was equipped with *Cree, cool white* light emitting diodes. These diodes were arranged in a square array to illuminate the silicon wafers from the backside. The diodes exhibit a maximum intensity in a relatively narrow wavelength region around $\lambda = 450 \text{ nm}$ and a second, broader but less intense power distribution extending up to 750 nm, with a maximum at $\lambda = 540 \text{ nm}$. The light emitted from the diode-array was covering an $\approx 5 \times 5 \text{ cm}^2$ part of the wafer. The distance between the diodes and the backside of the wafer was around 2 cm, while the average light intensity was kept at 375 mW/cm^2 . To eliminate remaining IR-radiation, heat absorbing filters (*Schott KG 5*) were inserted between the diodes and the respective wafer. This setup was used for the investigations presented in chapter 4 (Photoluminescence imaging).

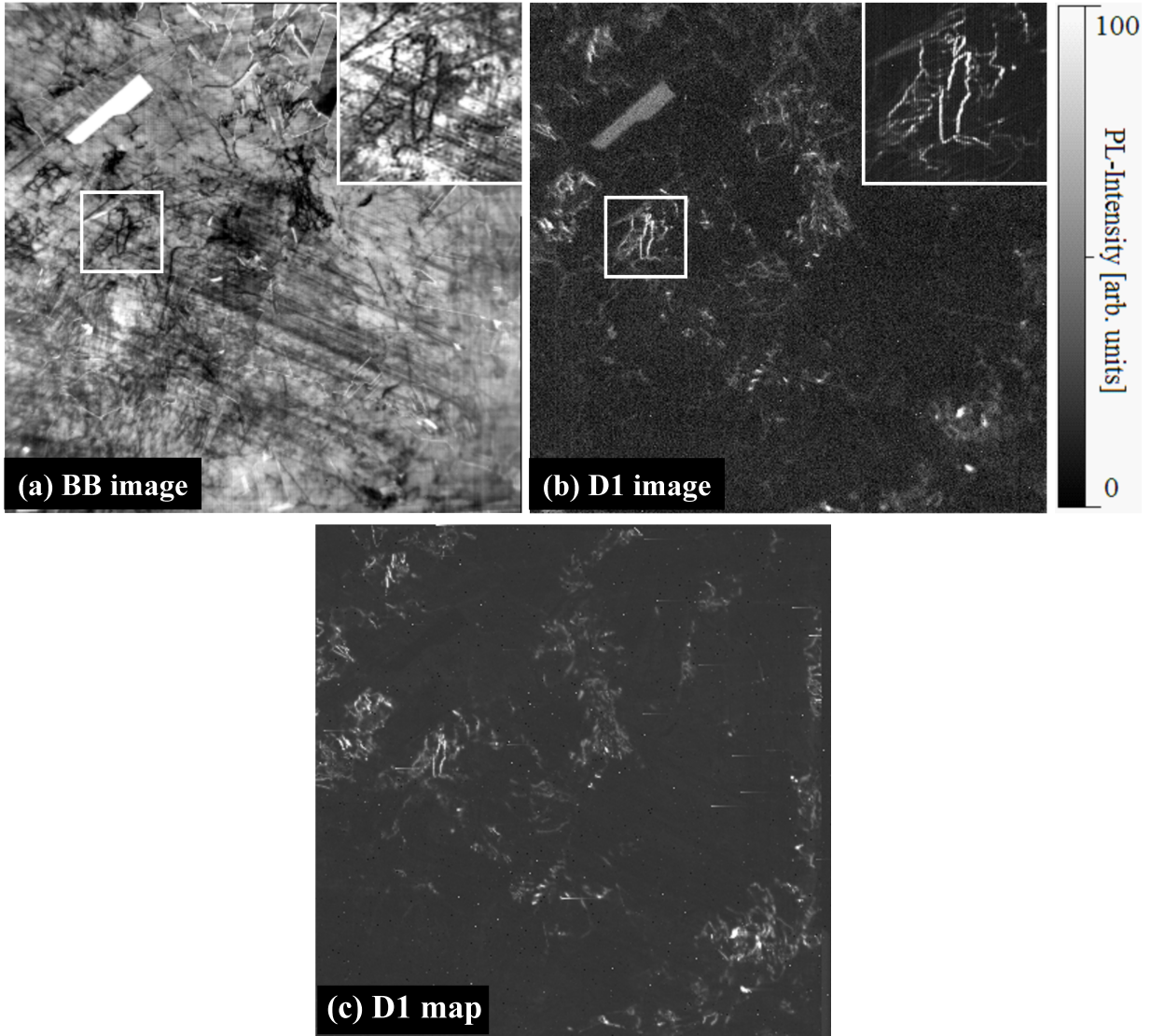


Figure 3.2.: Photoluminescence images of (a) band-to-band luminescence, (b) defect-related luminescence, and a photoluminescence map at 0.8 eV at room temperature (c) for comparison of the spatial resolution. The sample has a size of $5 \times 5 \text{ cm}^2$. Recording time for the images was a few seconds, whereas the recording time for the PL map was about 13 hours.

In a next step the “small” array of white LEDs was replaced by an array of nine *High Power LED660N-66-60* diodes. The experimental setup is the similar as that described above (Figure 3.3(a)). Each diode has a radiant intensity of 540 mW/sr at a current of 1.2 A. The radiant power of the diodes has its maximum at 660 nm. Heat protection filters

absorb the infrared radiation of the diodes, thus, no IR-radiation from the diodes will reach the InGaAs camera (*SU640SDV-1.7RT*). This setup was used for example for the photoluminescence images in chapter 5.

In Figure 3.3(c), a spectrum at a dislocation-rich region at room temperature is depicted; the blue graph shows the transmission curve of the filter used for the detection of the defect-related luminescence.

Electroluminescence imaging was done with the same detector, but the light source was replaced by a voltage source (cf. Figure 3.3(b)). On fully processed solar cells electroluminescence investigations can be done only. Electroluminescence was observed in forward as well as in reverse biased mode.

The recording time is the time of exposition and it depends on the intensity of emission and the camera sensitivity. The band-to-band (BB) images are recorded in 33 ms and the defect-related luminescence (DRL) images in approximately 500 ms.

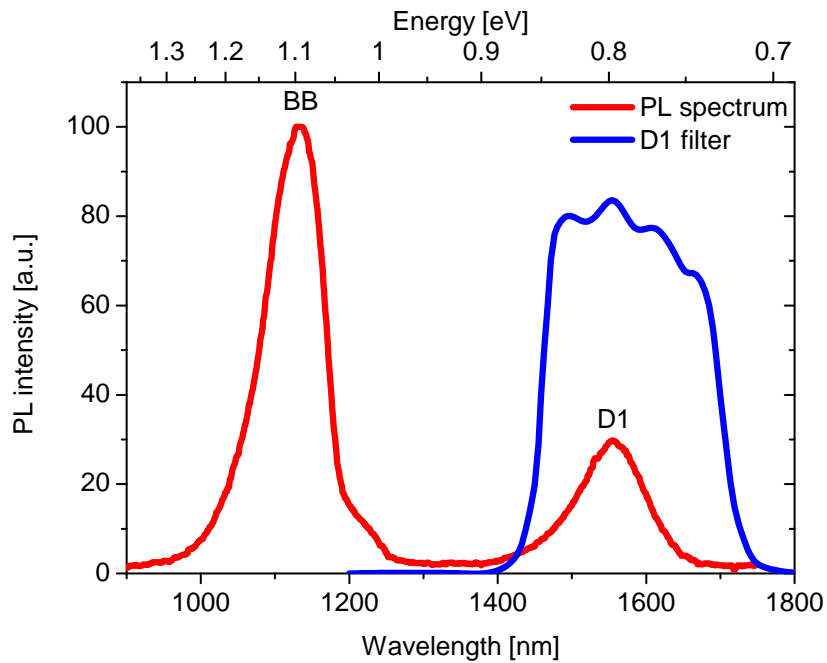
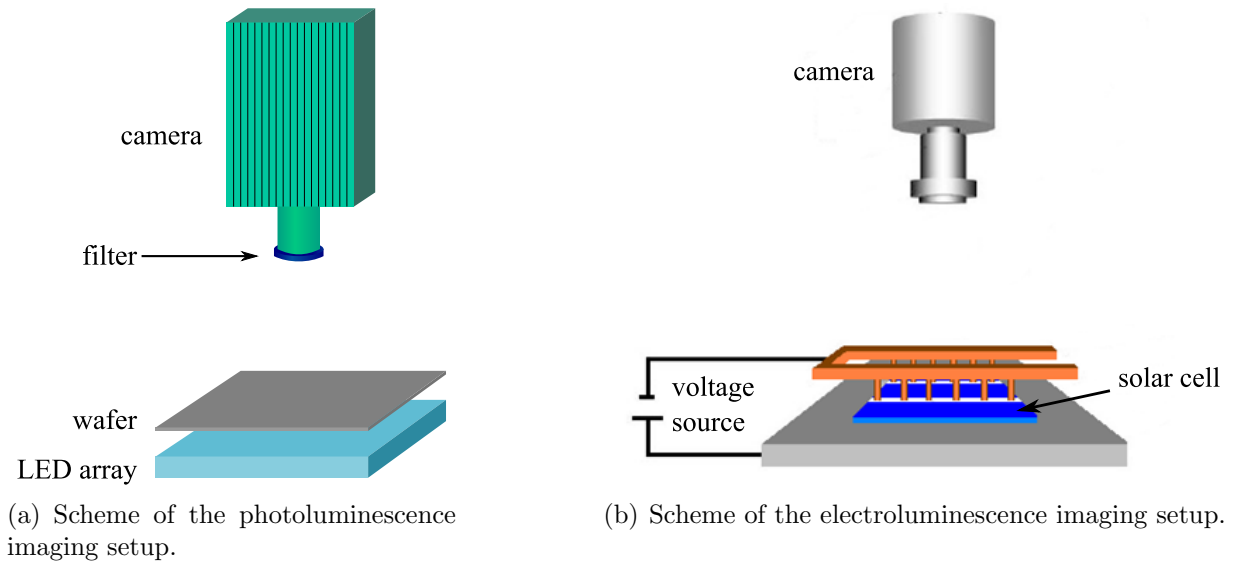
All of the recorded images are saved as raw data matrices. There is a distortion due to the camera lens. The dominating distortion is of barrel shape. A numerical procedure, based on orthogonal polynomial series expansion, can be used to correct the distortion. The procedure is available for *Octave*, *Freemat* and *MATLAB* and is called “RadialDistortion”. More about it could be found in reference [JP07]. The numerical data processing leads to blur in the image, mostly pronounced at the edges.

The raw and the processed data are converted into black and white images by using *Gwyddion*, but it is also possible with *MATLAB* or *Origin*.

3.3. Fourier-transform infrared spectroscopy

Optical transmission or absorption measurements are used to determine optical absorption coefficients and certain impurities. Certain impurities possess characteristic absorption lines due to vibrational modes, for example oxygen and carbon in silicon. Photons absorbed in a semiconductor can change the immediate environment around certain impurities producing local vibrational modes.

During transmission measurements light is incident on the sample and the transmitted light is measured as a function of wavelength as illustrated in Figure 3.4(a). The sample is characterized by reflection coefficient R , absorption coefficient α , complex refractive index $(n_1 - jk_1)$, and thickness d . Light of intensity I_i is incident from the left. The absorption coefficient is related to the extinction coefficient k_1 by $\alpha = 4\pi k_1/\lambda$. The transmitted light



(c) Spectrum at 300 K of a dislocated silicon sample with transmission curve of the filter used for D1 detection.

Figure 3.3.: Experimental setup for photoluminescence imaging (a), electroluminescence imaging (b), and a spectrum of a dislocated silicon sample exhibiting BB and D1 line at room temperature (red); the blue graph represents the transmission curve of the filter used for the detection of defect-related luminescence (c).

I_t can be measured absolutely or the ratio of transmitted to incident light can be formed. The transmittance T of a sample with identical front and back reflection coefficient and light incident normal to the sample surface is

$$T = \frac{(1 - R)^2 e^{-\alpha d}}{1 + R^2 e^{-2\alpha d} - 2R e^{-\alpha d} \cos(\phi)}, \quad (3.1)$$

where $\phi = 4\pi n_1 d / \lambda$ and the reflectance R is given by

$$R = \frac{(n_0 - n_1)^2 + k_1^2}{(n_0 + n_1)^2 + k_1^2}. \quad (3.2)$$

A normalized curve of I_t for polished silicon is shown in Figure 3.4(b).

Certain impurities in a semiconductor sample exhibit absorption. Examples are interstitial oxygen and substitutional carbon in silicon. Their density is proportional to the absorption coefficient at those wavelengths. The transmittance with absorption is

$$T = \frac{(1 - R)^2 e^{-\alpha d}}{1 - R^2 e^{-2\alpha d}}. \quad (3.3)$$

The absorption coefficient from Equation 3.3 is

$$\alpha = -\frac{1}{d} \ln \left(\frac{\sqrt{(1 - R)^4 + 4T^2 R^2} - (1 - R)^2}{2TR^2} \right). \quad (3.4)$$

R can be determined from that part of the transmittance curve where $\alpha \approx 0$. In some spectral regions there may be absorption due to lattice vibrations and free-carrier absorption for heavily doped substrates. [Sch06a]

For the Fourier-transform infrared spectroscopy (FTIR), an evacuated *ABB Bomem DA8* spectrometer is used. Differential FTIR measurements are applied. The spectrometer is equipped with a linear stage, which gives two advantages: first, drift/instabilities of the apparatus can be compensated, and second, it is possible to “scan” a sample. To reduce noise, a series of measurements per sample are carried out. Because of the long acquisition time, the occurring drift of the spectrometer has to be rectified. This is done by a periodical change of reference and sample during the measurement. Scanning, with congruent drift compensation, is done by measuring the reference, followed by the first point on the sample, then reference, followed by the second point on the sample et cetera. Therefore, the even spectra are these of the reference and the odd spectra these of different, well-defined points

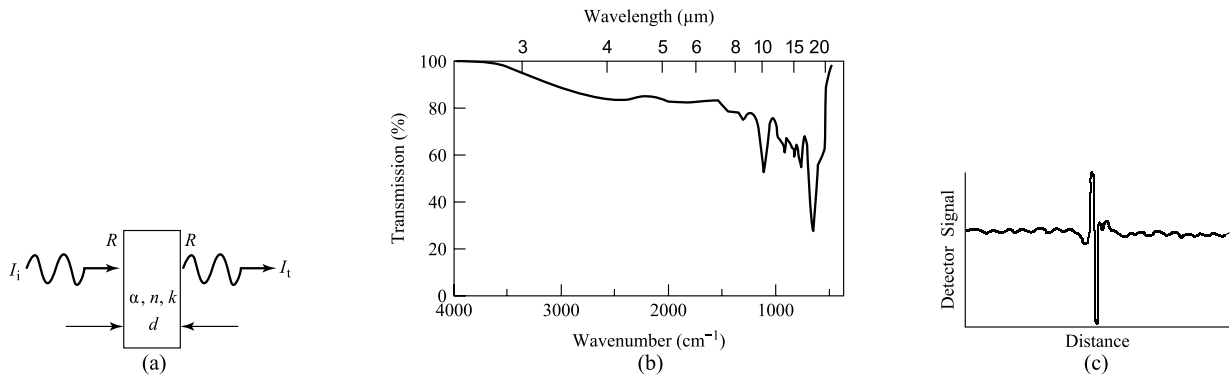


Figure 3.4.: (a) Schematic transmittance measurement, (b) normalized FTIR transmittance curve for a double-side polished Si wafer, (c) interferogram for the same wafer. After [Sch06a]

of the sample. A scheme is shown in Figure 3.5.

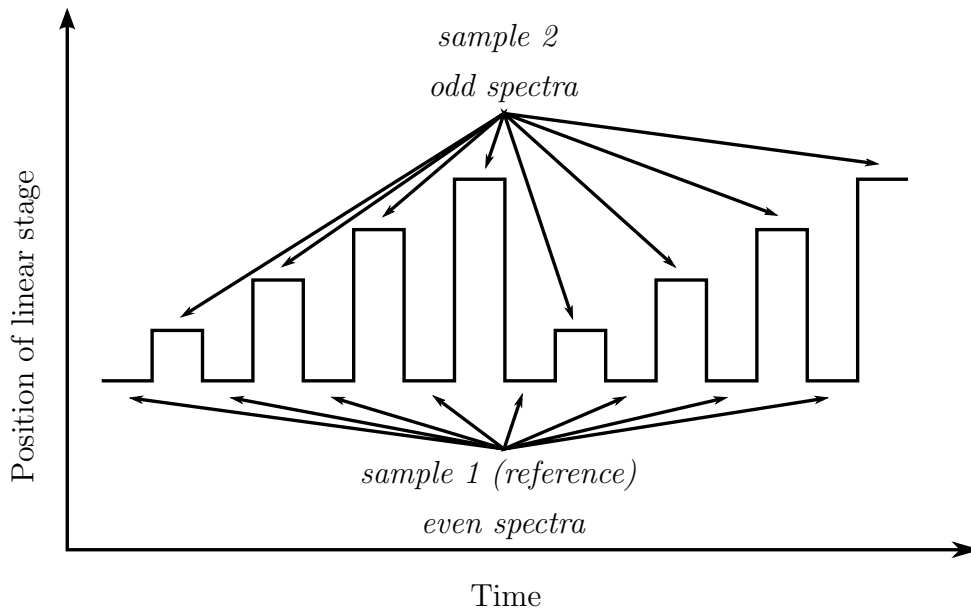


Figure 3.5.: Principle of the differential FTIR measurements. After [ARI06].

A liquid nitrogen cooled InSb detector is used to detect the transmitted radiation from the Globar. The spectra are detected in the range of $400 - 2000 \text{ cm}^{-1}$. The samples are measured at room temperature, thus the absorption lines of interstitial oxygen (O_i) and substitutional carbon (C_s) are at 1107 cm^{-1} and 605 cm^{-1} , respectively. Nitrogen (NN) should show an absorption peak at 963 cm^{-1} . The standard resolution is 1 cm^{-1} and the

aperture is set to 5 mm. These absorption peaks are superimposed on phonon excitations of the silicon substrate and should be subtracted from the spectrum of a carbon- and oxygen-free reference sample.

3.4. Electron-beam-induced current

EBIC measurements were performed with a *Zeiss EVO 40* SEM. Scanning with the electron-beam over the sample generates electron-beam-induced current. This EBIC signal was led to a current pre-amplifier and subsequently digitized to a PC with *Gatan* software for evaluation. The beam current was measured using a Faraday cup at the sample holder. Temperature data are gathered using a diode placed inside the sample holder close to the sample backside. Afterward, evaluation was performed using *Gwyddion* software for gathering profiles from recorded EBIC images, before exporting these raw data sets for further analysis in *Origin*.

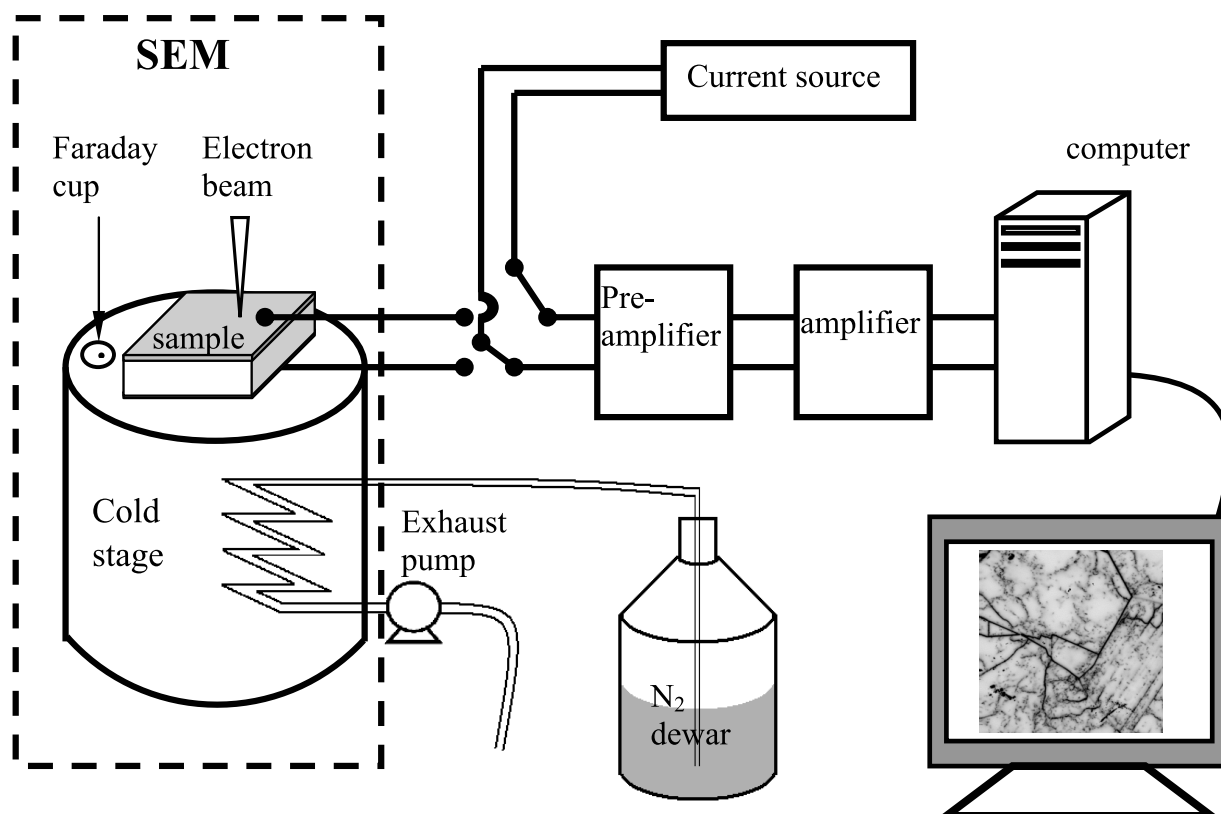


Figure 3.6.: Experimental setup of EBIC measurements. After [Jia09]

Part II.

Measurements and results

4. Photoluminescence imaging

With its conveniences of low cost and remarkable performance, multicrystalline silicon has a decisive disadvantage: it contains different types of defects, which should be engineered and monitored in the course of the cell production, in order to minimize their impact over the final device. Among those defects, dislocations and grain boundaries are identified as sources limiting the cell performance.

Either those crystal defects have the property to be electrically active, induced by their structure, by decoration with transition metals or oxide precipitates. At these defects, the minority charge carriers will recombine and subsequently do not account to the power generation. A technique, which gives a detailed access to the dislocation recombination activity and their lateral distribution, is the photoluminescence imaging. A system was developed to investigate solar wafers (cf. Section 3.2).

Several measurements and results presented here, have been reported previously in my Diploma-thesis [Man11].

4.1. Samples and measurements

In this section, photoluminescence images of multicrystalline silicon solar grade wafers at different processing steps are presented. The investigated wafers are neighboring wafers, that means they are from the same region of an ingot and have therefore a comparable structure. All of the wafers undergone the same process, but after each step one of them was withdrawn for characterization. The following figures show band-to-band (BB) and defect-related luminescence (D1)* images. The images show a part of the full wafer, the dimension is $52 \times 52 \text{ mm}^2$. The dimension of a wafer is $156 \times 156 \text{ mm}^2$, the thickness is found to be approximately $200 \mu\text{m}$. The measurements were performed starting at the

*Defect-related luminescence at around 0.8 eV is denoted here as D1 luminescence, which implies dislocations as its origin. However, besides dislocations, oxygen-related luminescence appears in this energy range too, which is discussed in subsection 5.1.2.

end of the manufacturing process (ARC deposition) and going gradually backwards to the textured wafer (cf. Figure 4.1).

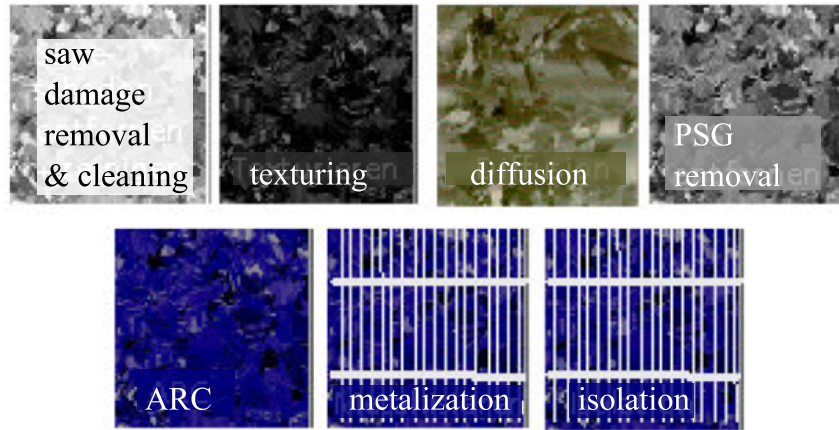


Figure 4.1.: Photographs of wafers after certain processing steps of a silicon solar cell.

Anti-reflection coating

As mentioned before I started to investigate the solar wafer after anti-reflection coating. The Si_3N_4 coating passivates the surface of the wafer, which suppresses surface recombination. Figure 4.2(a) shows the BB image of a $52 \times 52 \text{ mm}^2$ section of a wafer. The section shows a relatively large dark area, this area corresponds to a high density of defects (compare Figure 4.2(b)). As one can see, the D1 image (Figure 4.2(b)) gives a further detailed view of the distribution of defects. Furthermore, the D1 image reflects not all dark areas, supposed crystal defects, of the BB image. The D1 and BB images are essentially inverted; the dark BB areas appear bright in D1. However, there are exceptions in this anti-correlation due to non-radiative defect-related recombination. Surface recombination can be a candidate for a competing non-radiative process. The BB image shows surface damages, seen as dark horizontal stripes. These scratches or damages at the surface are no crystal defects and hence cannot be seen in the D1 image.

PSG removal

The preceding processing step was etching the phosphosilicate glass off. The wafer after PSG etch has already an emitter but its surface is not passivated intentionally. Figure 4.3(a) presents the BB image of a section of an entire wafer. Figure 4.3(b) shows the

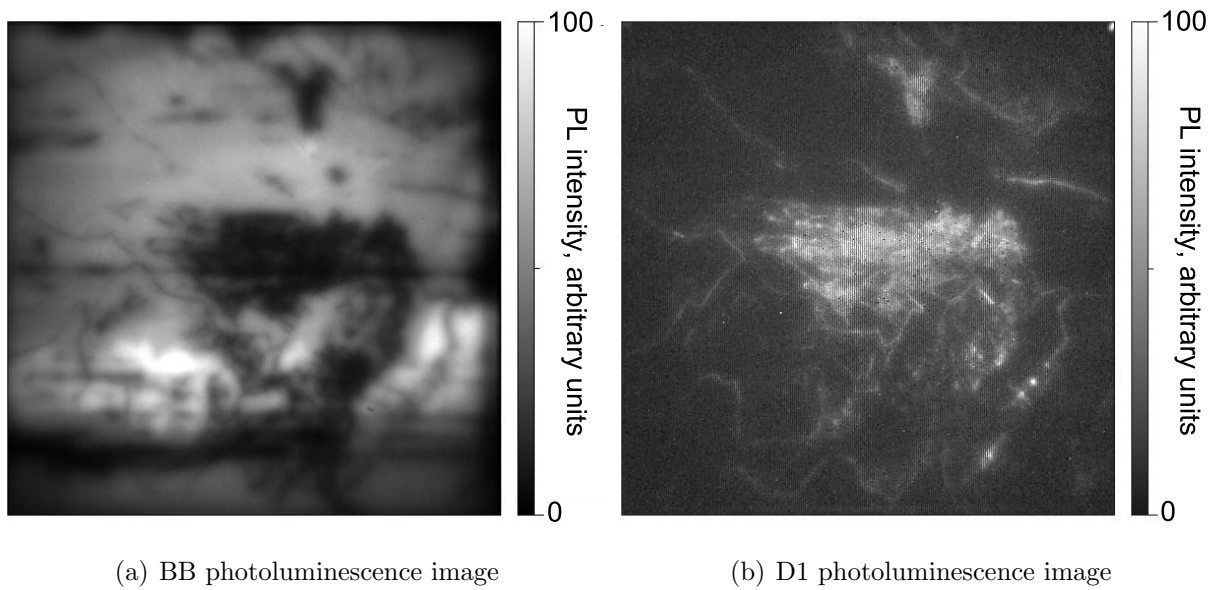


Figure 4.2.: Band-to-band and D1 images of a part of a wafer after Si_3N_4 coating.

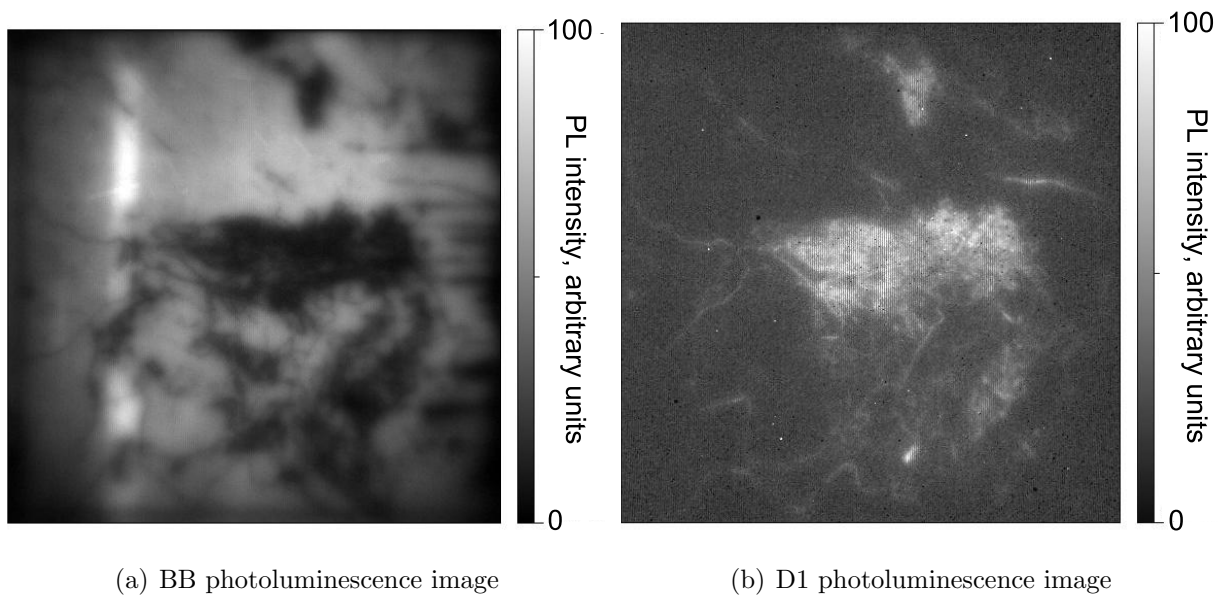


Figure 4.3.: Band-to-band and D1 image of a part of wafer after P-diffusion, the phosphosilicate glass has been removed.

corresponding D1 image. The Figures 4.3(a) and (b) offer a similar pattern like these in Figures 4.2(a) and (b); this is because neighboring wafers are imaged. In this figure, one can also see some of these surface damages in the BB images but no corresponding defect-related luminescence in these regions in the D1 image.

P-diffusion

At this processing step, the cell got a high-doped emitter on one side of the substrate. This is an essential step in the standard processing, because the cell needs a p - n -junction to be functional. Figure 4.4 shows the image of a section of a wafer with an existing PSG-layer. In comparison to the BB images of the wafers without PSG and after Si_3N_4 coating, Figures 4.3(a) and 4.2(a), respectively, the BB image appears much brighter. Moreover, the D1 image shows more noise than those in Figures 4.3(b) and 4.2(b). Nevertheless, these images show nearly the same pattern as the other images.

Texturizing

This wafer has a textured surface to get a better coupling of the light into the substrate. To get an image at this processing step a laser illuminating system was used, the other method was not successful. Because of the rough surface and missing passivation the resolution of the images in Figure 4.5 is rather weak. Most of the luminescence is scattered in all directions and not to the detector only. There are no clear structures visible, it gives just a roughly distribution of the defective areas.

4.2. Results and discussion

In this section, I will analyze and discuss the experimental results. The first feature one has to prove is, if the camera detects defect-related luminescence, especially D1 or luminescence in the range of D1 (e.g. oxygen precipitates). The next important issue to look at is what information the images provide. The change of the luminescence pattern after different processing steps will be considered.

4.2.1. Luminescence around 0.8 eV

First question is: does the camera detect defect-related luminescence? Thus, the transmission spectra of the filters are superimposed on a typical photoluminescence spectrum

4. Photoluminescence imaging

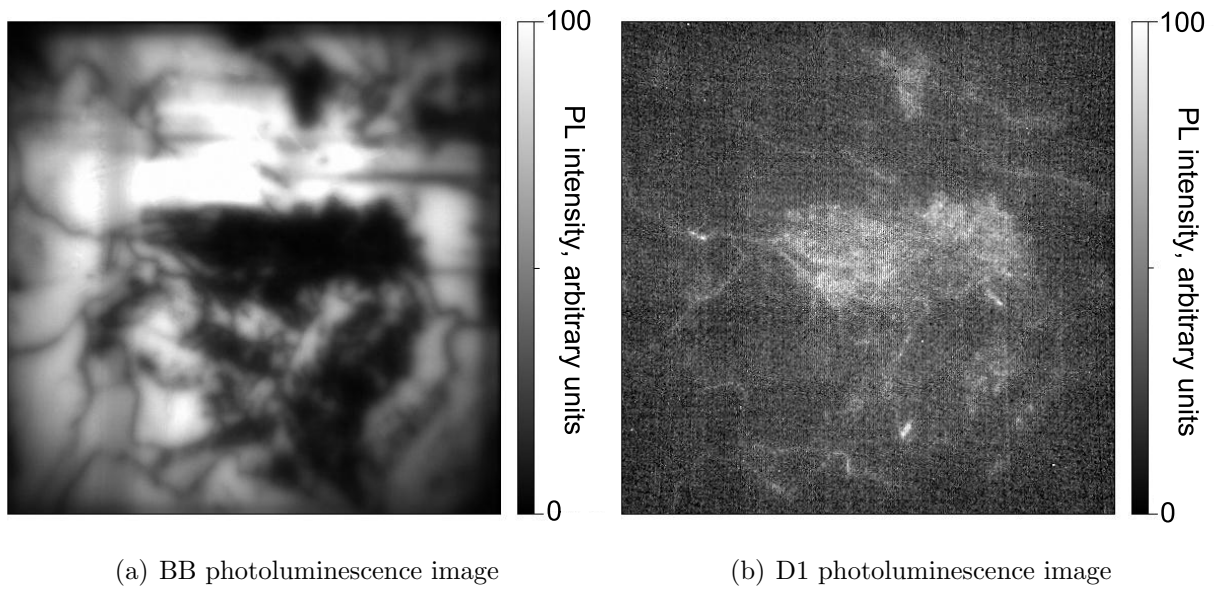


Figure 4.4.: Band-to-band and D1 image of a part of a wafer after P-diffusion, the phosphosilicate glass is still on the wafer.

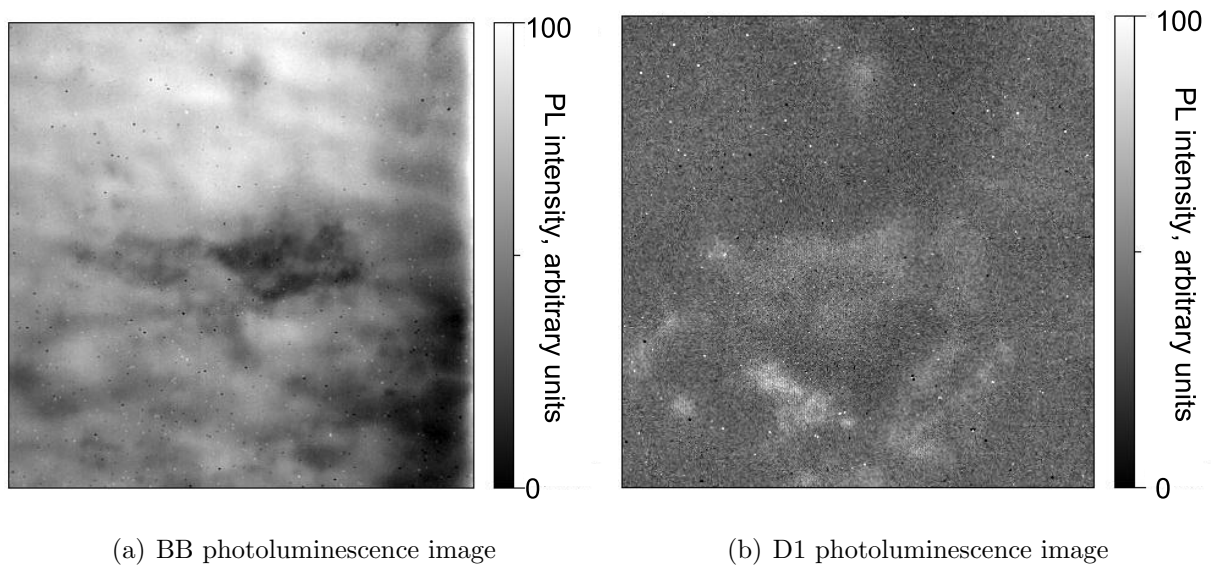


Figure 4.5.: Band-to-band and D1 image of a part of a textured wafer using a laser for illumination.

of such mc-Si or umg-Si wafers. This superimposition is displayed in Figure 4.6; the photoluminescence spectrum (black graph) is taken at the point the arrow in the “D1 map” (Figure 4.7) indicates. The D1 map was created using the scanning photoluminescence technique, whereas the monochromator was set to 1550 nm respectively 0.8 eV. The green graph shows the transmission spectrum of the long-pass filter, used as BB filter. The red graph represents the transmission spectrum of a band-pass filter having its transmission between 1450 nm and 1700 nm (FWHM). Thus, it covers the spectral range of D1 radiation, following this filter is named D1 filter. The sensitivity of the camera is limited to a spectral range of 0.9 - 1.7 μm (blue graph); the BB filter blocks only a small wavelength range of infrared radiation from the light source. Obviously, the band-to-band radiation is much more intense than the defect-related radiation. Hence, the impact of D1 radiation on the BB images can be neglected. The spectrum shown here was taken at a point where strong D1 luminescence appeared. Due to the relative large wavelength range, the D1 filter covers, this could maybe a reason for the good, contrast-rich D1 images.

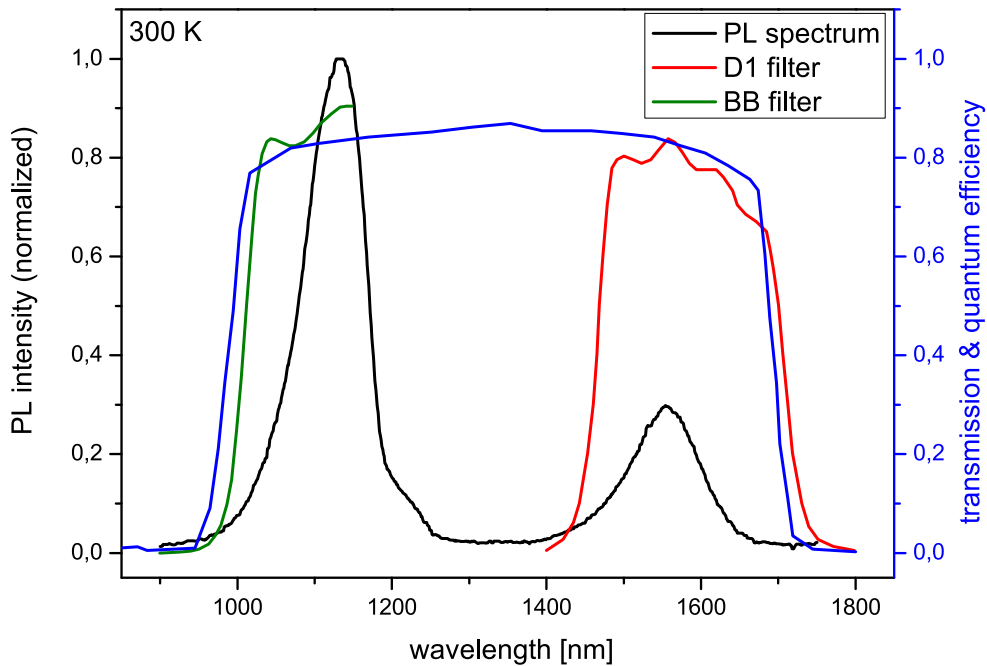


Figure 4.6.: Transmission spectra of the BB and D1 filters, and quantum efficiency vs. wavelength of the camera superimposed on a typical room temperature photoluminescence spectrum of the investigated wafer.

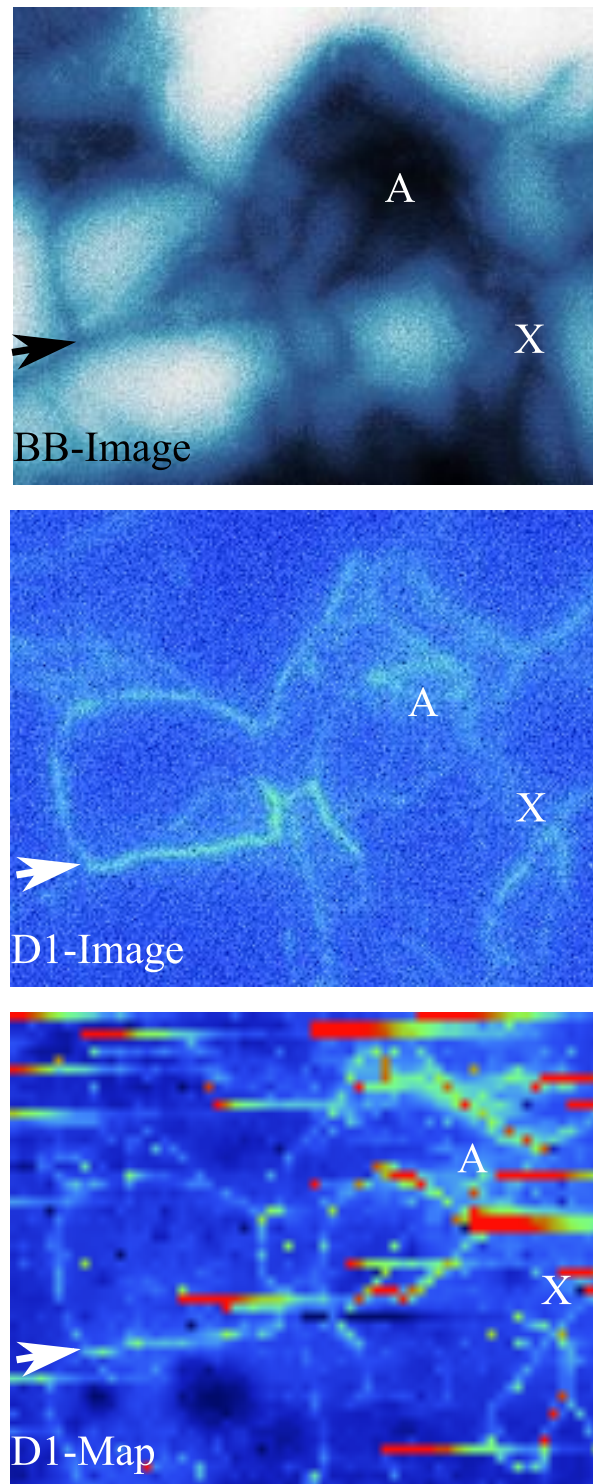


Figure 4.7.: Band-to-band and D1 photoluminescence image, and D1 photoluminescence map of an area of about 1 cm^2 . The arrows indicate a corner of a grain boundary to guide the reader. The red dots and stripes in the D1 map are artifacts.

The comparison of the photoluminescence images and maps let me conclude that both show the same luminescence at all. D1 luminescence is detected on the maps and the images. Furthermore, the noise at room temperature measurements for defect-related luminescence in the images is insignificant in contrast to the maps. This occurrence is a benefit for the imaging method.

Additional prove for the correct detection of D1 is obtained by considering the BB images and assuming anti-correlation between BB and D1 radiation [TOHR00]. The BB image and the D1 image show essentially inverted patterns. The dark regions in BB resemble the bright ones in the D1 image. By comparing D1 and BB images a large dark area, marked with an “A”, in the center of the BB image is observable. This should imply that the defect-related luminescence in this region has to be rather high. On the contrary, the D1 image shows only a few selected lines and a brighter “background”, but not a filled bright area. The D1 map apparently gives some more information, because in this range one can see a higher distribution of defect-related luminescence. One can say that in this grain could be a higher density of dislocations than in others, such as in the upper part of the images, where a very bright band-to-band luminescence occurs.

Moreover, not all of the grain boundaries in the D1 image radiate with the same intensity, what could be an indicator for possible contamination. If one assumes that some transition metals decorate the dislocations or they accumulate at the grain boundaries, they may produce deep traps in the band gap and hence a non-radiating recombination route is given. This recombination path, presumably Shockley-Read-Hall recombination, implies decreasing luminescence intensity. Another possible cause, why some grain boundaries appear brighter than other, could be a difference in the dislocation strain field or dislocation type. On the other hand, each of this mentioned factors could play a role for this behavior: as a reaction product of all of them.

4.2.2. Comparison of BB and D1 images

In Figure 4.8, the band-to-band and D1 images of three neighboring wafers after different processing steps are depicted. The three associated processing steps are: (i) after Si_3N_4 coating, (ii) a wafer with emitter after removal of the phosphosilicate glass (PSG), and (iii) a wafer with emitter and existing PSG layer.

In general, one can assume that D1 and BB luminescence anti-correlate, but there are exceptions of this common rule. In the following reasons for these exceptions are pointed out and explained.

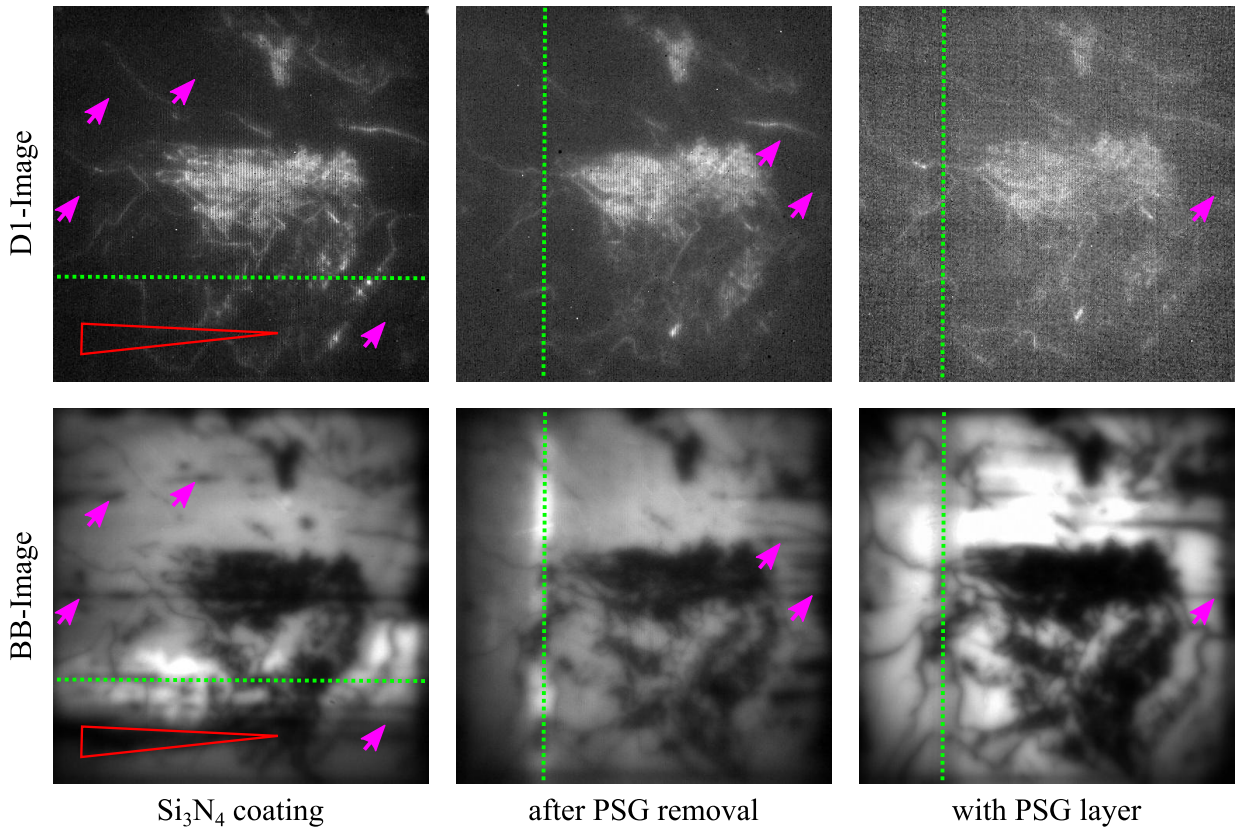


Figure 4.8.: Band-to-band- and D1 PL images of a $5 \times 5 \text{ cm}^2$ area of wafers after different processing steps. For the description of the indicators see text.

The magenta colored arrows indicate to several potential surface damages like scratches in the BB images. These damages lower the band-to-band luminescence, because at these regions occurs generally surface recombination. In the D1 images is no defect-related luminescence at these points detectable, hence, there is a further clue for a high non-radiating surface recombination rate. As well, the red triangle in the images of the Si₃N₄ coated wafer indicates an area where the band-to-band and the D1 radiation are quenched.

Green dotted lines in the images indicate areas of the wafer where remainders of the solution of the phosphorus diffusion the conveyor belts moistened and contaminated the backside of the wafer. Only in the BB images appear these stripes, which should be caused by the high intensity of band-to-band radiation in comparison to the defect-related radiation. In those wafers without PSG, so after PSG removal and Si₃N₄ coating, these stripes are brighter by a factor of two than in “clean” areas of the wafer, but in case of an existing PSG layer, these stripes are darker. The brighter appearance in the wafers

without PSG layer could be explained by a mirror effect at the backside of the wafers in these regions, in such a way that the light will be reflected a few times inside the wafer at these positions and subsequently amplified.

The brighter BB images of the wafer with PSG layer, in contradiction to the wafers without PSG layer, may occur due to the PSG layer itself. It might be possible that the emitted band-to-band radiation of silicon is reflected at the front surface (sunny side of the wafer), and consequently increases the detected signal. Another aspect could be that the PSG layer itself emits some radiation in the detected range, which also would explain the low contrast in the D1 image.

The images show a non-homogeneously distribution of light. The center of each image is brighter than the border areas of the image. This is caused by two technical problems: the first one is the small area of the LED array for illumination, which could be solved with a larger array of some more diodes; the second one is the small size of the filters placed between the sensor of the camera and the wafer. The aperture of the camera objective is larger than the diameter of the filters, because of this; one needs a ring to fix the filter inside the objective of the camera, which reduces the field of view of about one centimeter in diameter. Therefore, the outer area is darker.

In summary, one can say that the BB images show a few defects. However, on contrary only the D1 images show the real defect-related luminescence, which is much more interesting to research in this case, because surface defects give no information about the substrate. Therefore, it seems more reasonable to observe both types of images to get a better understanding of the luminescence characteristics and their information of the wafers.

4.2.3. Influence of different processing steps

This section is devoted on the possibilities to detect specific changes in the D1 and the BB images characterizing the process, which the wafers are subjected. Finding such differences one also obtains a tool for prediction and control the process in a non-destructive way. At first, the BB luminescence will be compared and then the behavior of the D1 luminescence will be discussed.

BB luminescence

The band-to-band luminescence intensity is proportional to the lifetime of minority charge carriers in a certain range of excitation levels. Accordingly, it is useful to get the distribution of BB luminescence of a whole wafer to get first information of defect-density of the device.

The overall lifetime distribution increases with ongoing production. This can be seen in the different bright BB images of the three different wafers in Figure 4.9. The brightness correlates directly with the BB luminescence intensity, and therefore with the lifetime of the minority charge carriers. At first glance, the image of the wafer after PSG etch seems to be brighter than the silicon nitride coated, but looks darker than the image of the wafer with PSG layer. This leads to the assumption that the minority charge carrier's lifetime decreases with proceeding fabrication steps. However, if one has a closer look, the dark areas in the images are getting smaller with proceeding fabrication. The dark areas in the BB images can be indicated as defective areas, particularly as areas with increased defect-related luminescence intensity.

Before the PSG layer is removed, there is a large amount of extremely good regions. For the PSG sample, the histogram shows a local maximum at the right end of the scale, which means, that the lifetime of minority charge carriers is rather high. Nevertheless, on contrary this histogram shows on the left side an accumulation of regions with very low lifetimes. By processing further, the extremely good regions decrease, but the bad regions decrease as well. The coexistence of those two phenomena leads to an overall assimilation in average. The very good and very bad regions getting lower and the "main stream" move to the middle and gets broader.

After PSG removal, an increase of surface recombination is possible. Thus, the PSG layer itself acts like a surface passivation. With the loss of this surface passivation, the minority charge carriers have the possibility to recombine at the surface. Another aspect could be a stronger reflectance of the etched surface. Thus, less light will be absorbed in the bulk material and accordingly less minority charge carriers are generated.

Further processing (step from Emitter to ARC) leads to an increase of the mean intensity population. The silicon nitride coating passivates the surface; hence, surface recombination is suppressed. Furthermore, the anti-reflective impact of the coating yields to an increase of absorbed photons, and subsequently an increase of generated carriers. Consequently, the BB intensity is evened out among the cell. The dislocations partially become passivated by the hydrogen in the coating, too. This decreases the amount of bad regions. The hydrogen atoms bind quasi-free charge carriers of dislocations and thus deactivate their impact on

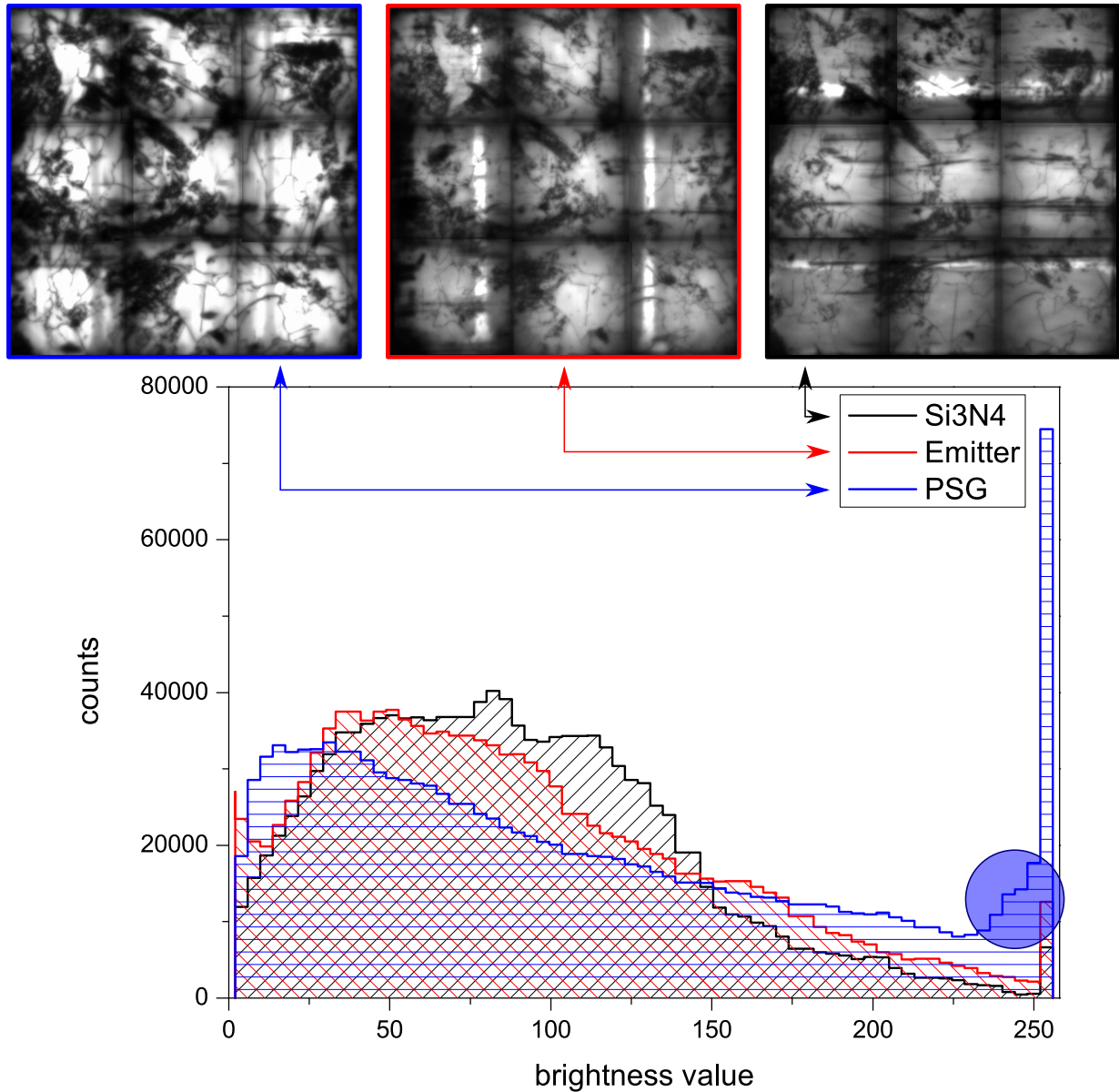


Figure 4.9.: Histograms of band-to-band luminescence signal of different wafers. All images were made under the same conditions; no contrast correction was applied. (PSG denotes the wafer with PSG layer, Emitter denotes the wafer after PSG etch, and Si₃N₄ denotes the wafer with silicon nitride coating.)

defect-related recombination.

D1 luminescence

Additionally to the BB luminescence, the D1 luminescence was observed as well. The D1 gives a further access to the recombination activity and characteristics of minority charge carriers in solar cells.

By analyzing the D1 images, a decrease of defect-related luminescence during the fabrication process is observed. The images and the corresponding histograms in Figure 4.10 substantiate this. It is important to note that the peak position displays the mean intensity strength, and the peak height shows how large the area is, which emits the radiation with the certain intensity.

The histograms have at first glance a similar shape. Their distributions have a positive skew. That means the right tail is longer; the mass of the distribution is concentrated on the left of the figure. Accordingly, the amount of darker regions is prevalent in the corresponding images. This is quite clear, because the areas with low defect-related luminescence intensity should prevail in solar cells. The right tail of a distribution is a sign for existence of one or more peaks to the right of the main distribution.

The PSG sample shows the highest density of regions with an intense of D1 luminescence. The high density could be explained by a possible strong interaction between the PSG layer and the substrate. At the interface a network of extend defects is created and causes defect-related radiation. Besides that network, the ingrown defects affect an increase of the D1 luminescence intensity. The histogram of this sample would support this. One can say that the histogram's shape is build up by two or maybe three peaks. Hence, it can be deduced, that the D1 luminescence in this sample is originated from at least two different populations of dislocations.

Removal of the PSG layer leads to an overall decreasing defect luminescence. Now the interface network is off and thus this part of radiation is decreased. Because the HF dip does not remove all of the PSG, leftovers can account, in much lower degree than the layer, to a defect-related radiation. A closer look to the sample images (PSG and Emitter) indicate that some new defects may just “appear”. These defects could be located deeper in the substrate and are excited only now. The two peaks, which form the shape of the distribution in the corresponding histogram, are an indication for such consideration.

Further processing of the wafer, especially deposition of silicon nitride, affects decreasing defect-related luminescence. On the one hand, the SiN_x coating yields to higher light ab-

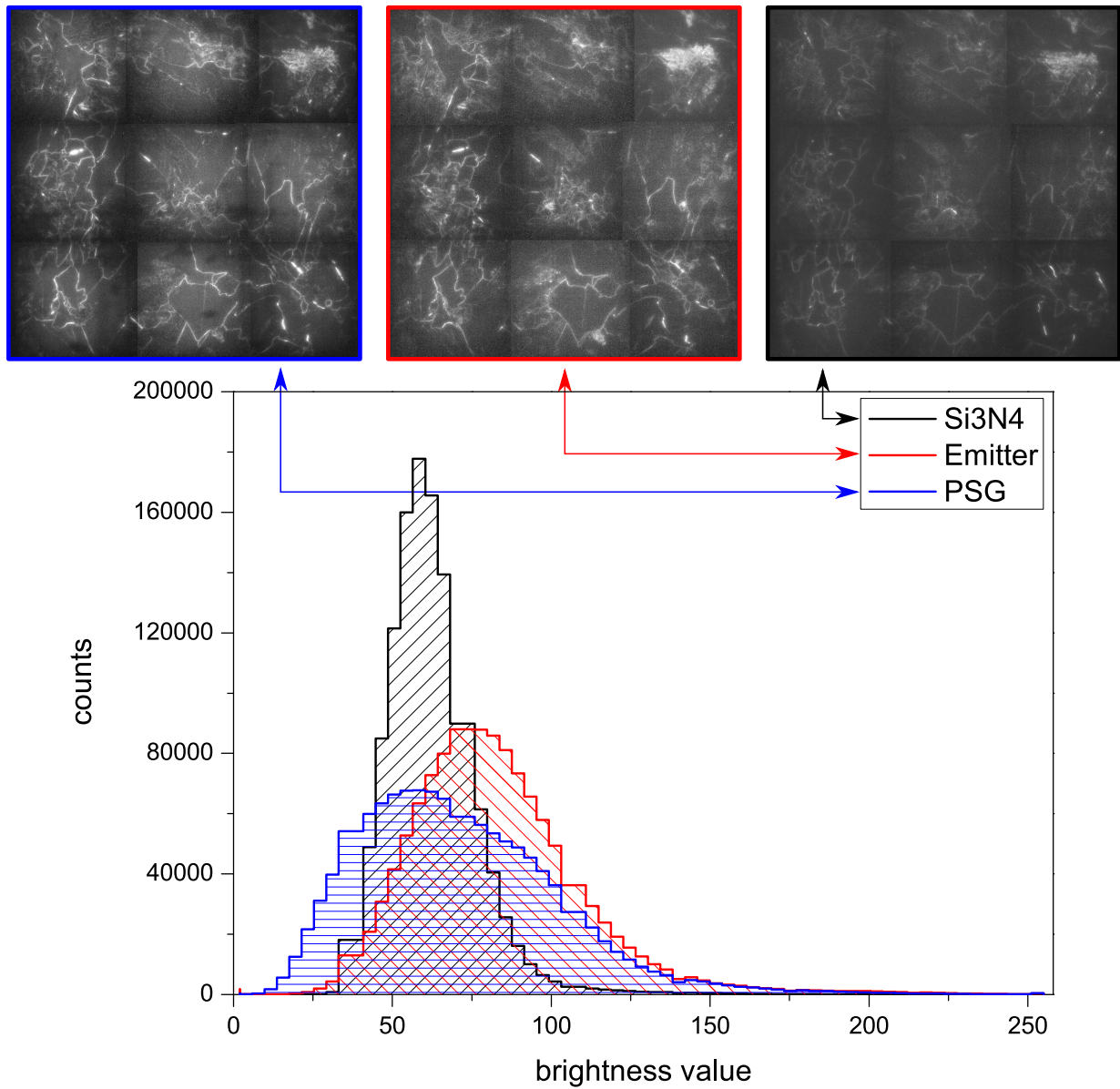


Figure 4.10.: Histograms of D1 luminescence signal of different types of wafers. The images are contrast corrected, thus the position and width of the peaks are shifted. (PSG denotes the wafer with PSG layer, Emitter denotes the wafer after PSG etch, and Si3N4 denotes the wafer with silicon nitride coating.)

4. Photoluminescence imaging

sorption in the substrate; hence, an increase of charge carrier generation is expected. This would lead to an increase of luminescence at all. However, on the other hand, the passivating effect of the hydrogen at the extended defects seems to be much stronger. Therefore, the overall D1 luminescence decreases. Moreover, the surface is passivated too. Thus, possible radiation centers near the surface (e.g. at the PSG remainders) are deactivated and consequently do not contribute to the luminescence. The histogram supports the decrease of defect-related luminescence. The distribution gets narrow and the flat decline on the right indicates low luminescence, but in a wide range of intensities. Thus, there are recombination centers, which radiate with a broad distribution of intensity values.

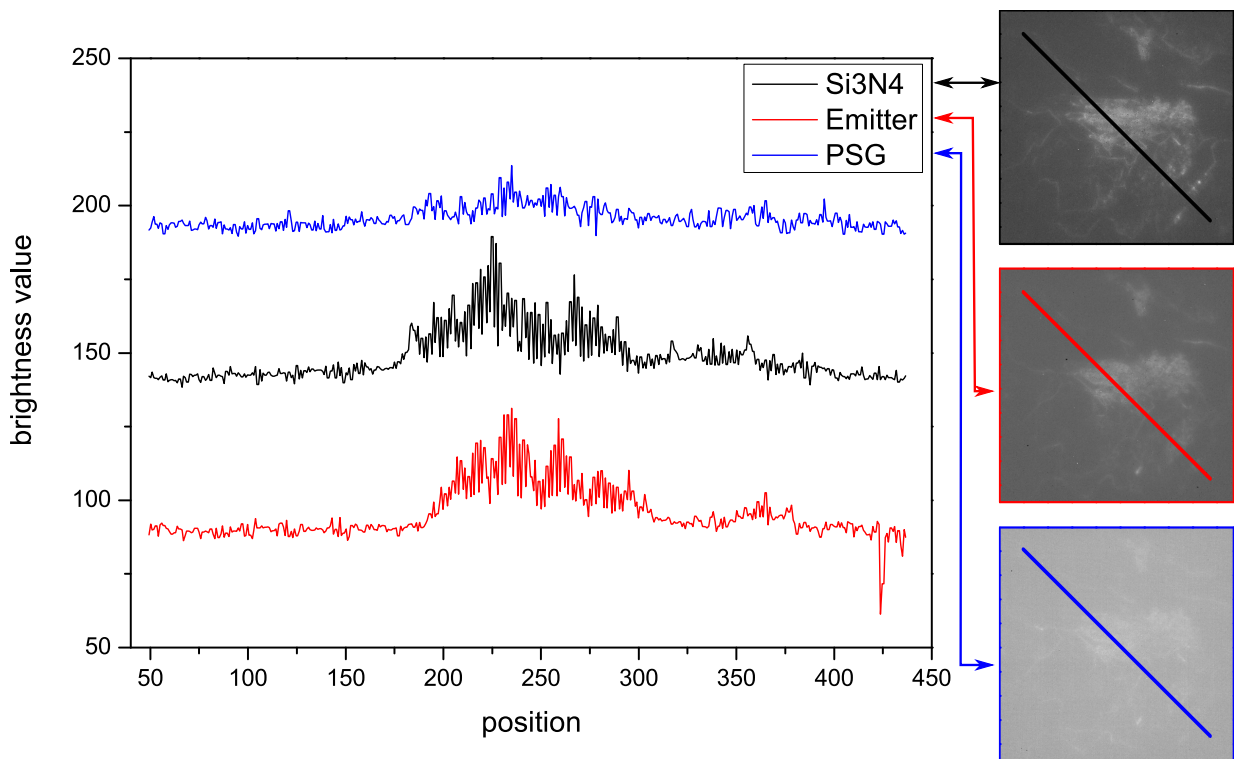


Figure 4.11.: Profiles of D1 images of wafers at different fabrication steps. The lines in the images indicate the range of the taken profiles. The images are not contrast corrected, so that one gets an impression of the distribution of the raw data.

The profile graphs in Figure 4.11 indicate that the PSG layer affects a not proper light coupling. The wafer with PSG layer (blue) has a low profile, which is an indicator for a low luminescence signal and the low contrast. After removing the PSG layer (red), the signal increases drastically. The difference between the profiles of the silicon nitride coated wafer (black) and the wafer after PSG removal are sufficient low. The one and only difference is

the shift of the absolute brightness value, which could be explained by the behavior of the camera. The background signal varies from frame to frame.

In summary, one can say that during the processing an effective upgrade of the material quality occurs. In a microscopic scale, this upgrade is caused by a change in the defect activity. As far as dislocations are concerned, there is a mutual relation between their recombination activity and luminescence. The dislocations are differently susceptible to modification of their activity by the processing. The above reasons reveal that a change in the material should cause a change in the D1 luminescence intensity distribution.

4.3. Summary

The developed system has the advantage to observe band-to-band (BB) and defect-related (D1) radiation at room temperature on large-scale wafers at different stages of their processing. The studies showed that the processing of a wafer causes a significant change in the images of its luminescence. The BB as well as D1 luminescence images deliver different and in many aspects supplementary information, which is specific for the processes that the wafer has been subjected. It has been shown that especially D1 luminescence provides much more information than the BB. Conclusions about the defect activity and their evolution over the fabrication course can be drawn by analyzing those images. Using D1 and BB, the surface recombination activity impact can be excluded from the analysis to a significant extend. Such approach is much more reliable than using the standard practice of imaging BB only [TBSW06].

The BB mean intensity is a qualitative characteristic of the lifetime of minority charge carriers, particularly the higher the intensity the higher the lifetime. The BB images show a map of the distribution of lifetime of the minority charge carriers. The BB distribution histograms give information of good and bad regions in a solar wafer in more detail. These histograms give a quantitative access to the BB intensities and therefore to the minority charge carrier lifetimes.

The D1 mean intensity indicates the strength of the electrical activity of the dislocations. A higher intensity leads to the conclusion that the defects are quite active. Consequently the lifetime of the minority charge carriers is reduced and thus the cell efficiency. The D1 images give an overview of the amount of such efficiency limiting defects. Furthermore, one gets with these images and their distribution histograms comprehensive details of their distribution over the cell and strength of luminescence.

4. *Photoluminescence imaging*

By analyzing only BB images one can misinterpret the data, because they show surface damages as “defective” areas as well. The D1 images show only the defective areas which are related to dislocations and grain boundaries. Hence, it is necessary to analyze both, the BB and the D1 photoluminescence images.

5. Spectroscopic photoluminescence

In this chapter, spectroscopic photoluminescence measurements of different samples are presented. The first part contains investigations of solar wafer material. Various defect-related luminescence lines are studied. The second part deals with silicon thin film on glass samples. Finally, the results of bulk and thin film multicrystalline silicon are compared.

5.1. Multicrystalline silicon

The investigated materials are unprocessed multicrystalline silicon solar wafers. First investigations were done by photoluminescence or electroluminescence imaging on neighboring full processed solar cells, to locate outstanding regions. These prominent sample areas are prepared for spectroscopic analysis and have a size of about 1 cm^2 .

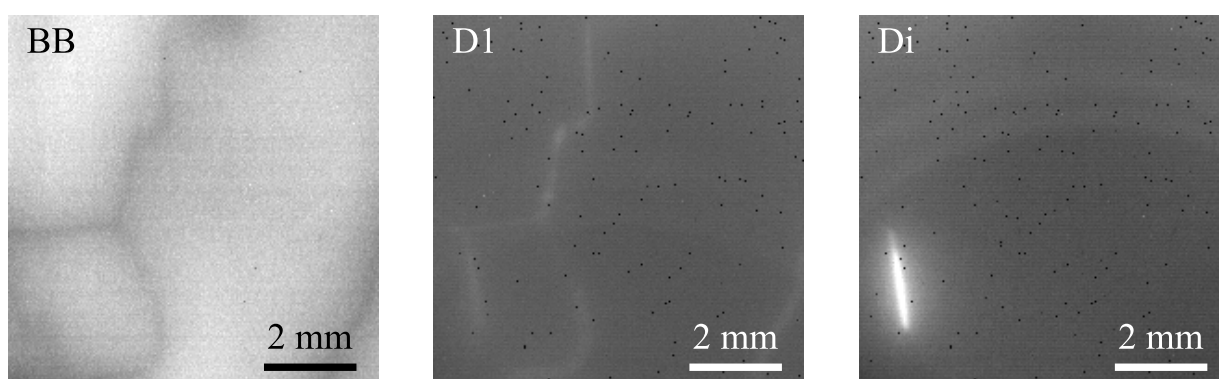
Extended defects in multicrystalline silicon solar cells are important factors limiting the solar cell performance [SAT⁺07, HDTO06, SRLW07, KRW06, JMU13]. To improve the cell performance it is necessary to understand their properties and study their recombination activity. Non-destructive techniques are widely used to identify defect sites in solar wafers and determine the local charge carrier lifetime [OTK⁺00, TBSW06]. A current method is the imaging of the photo- and electroluminescence of entire solar wafers and cells, respectively. This is usually performed at room temperature, and typically, two regions of the silicon spectrum are monitored. One is the band-to-band (BB) radiative transition at around 1.1 eV, the other one is at around 0.8 eV. The first is strong in defect-free regions and its intensity correlates with the local minority charge carrier lifetime [OTK⁺00]. The latter is specific for areas rich in dislocations and grain boundaries. This emission is regarded as the D1 of the dislocation spectrum. [MSAK12]

In this work, two luminescence lines are investigated in more detail. The first one is called “Di” line, which is located near the D3 line in the luminescence spectrum of silicon; the second one is labeled here as oxygen-related luminescence, which is near the D1 luminescence.

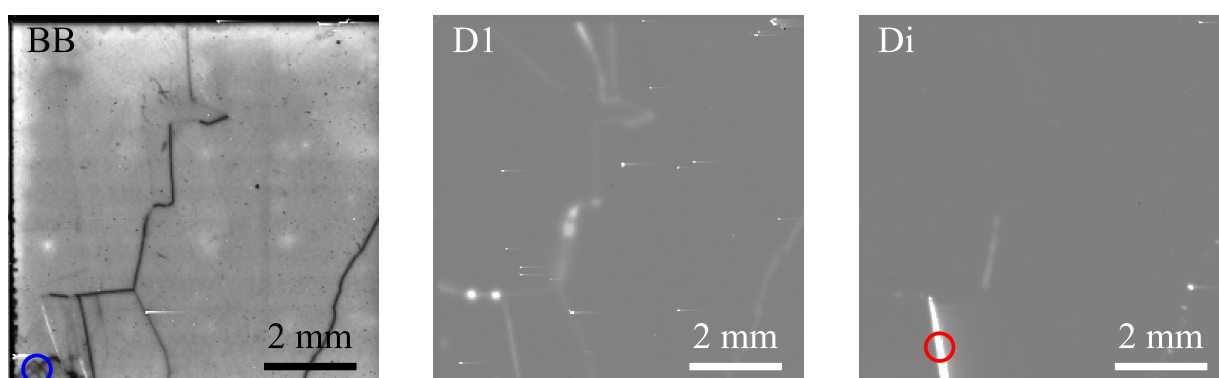
5.1.1. Di luminescence

During the last years, a new luminescence line in multicrystalline silicon has been detected. The luminescence band is nearby the well-known D3 line, but it is much more intense than the “classic” D3 luminescence. Furthermore, it is detectable at room temperature as well, whereas the D3 line is detectable at temperatures below 130 K only and appears together with the D4 line. First time it was reported in [Arg07].

At liquid nitrogen temperature, the Di line has its maximum in the range of 1333 nm (0.93 eV), D3 has its maximum at about 1310 nm (0.95 eV). At room temperature, it can be found at about 1365 nm (0.91 eV). To differentiate from the D3 line it is referred as “Di” line. [KAS⁺13]



(a) Room temperature photoluminescence images of a part of a solar wafer depicting the band-to-band, D1 and Di luminescence.



(b) Photoluminescence maps at 80 K of the same area as depicted in 5.1(a).

Figure 5.1.: Room temperature photoluminescence images of an area of a solar wafer showing Di luminescence (a) and the corresponding 80 K photoluminescence maps (b). The colored circles denote the regions where the spectra in Figure 5.2 are taken from.

The Di radiation and its distribution across solar wafers and cells can be obtained by

photo- and electroluminescence imaging by applying an appropriate filter in front of the InGaAs camera. The Di luminescence is very intense, even at low excitation. It is not absorbed in silicon and appears spatially localized at specific grain boundaries. An example photoluminescence image is shown in Figure 5.1(a). Here a small part of a full solar wafer is shown. In the left image the band-to-band, in the center the D1, and in the right image the Di luminescence are recorded. In the BB image, the grain boundary emitting Di luminescence is not dark, because the filter, used for BB luminescence detection, is an edge filter, particularly a high pass filter that opens at about 1000 nm. Thus, the strong Di luminescence is detected by the camera as well. For the D1 and Di luminescence images band pass filters with appropriate wavelengths are used. The corresponding photoluminescence maps at 80 K are shown in Figure 5.1(b). For the photoluminescence maps the monochromator was set to a defined wavelength before scanning, specifically for BB 1125 nm (1.10 eV), for D1 1525 nm (0.81 eV) and for Di 1333 nm (0.93 eV). The blue circle in the BB map (lower left corner) and the red circle in the Di map indicate the areas where the spectra in Figure 5.2 are taken.

Usually, Di luminescence appears as a high intense single peak with a maximum located at around 0.93 eV. Figure 5.2 presents three photoluminescence spectra demonstrating the difference between the ordinary D3/D4 and the Di luminescence: at room temperature and 80 K at a position with Di luminescence and at a position with D3/D4 luminescence. The spectrum in blue was taken at 80 K at a position where besides the band-to-band luminescence only the D3/D4 doublet at 0.95 eV and 1.0 eV with nearly equal height and width was observed. The spectrum in red was also taken at 80 K, but at a location emitting Di radiation. It shows a very intense luminescence at 0.93 eV; note that this spectrum is compressed by a factor of 10. At room temperature (black curve), the Di radiation is still present and exceeds the band-to-band intensity. The spectral positions of the Di and BB peaks are equally red-shifted upon heating due to the shrinkage of the band gap. The difference between the peak maxima of BB and Di is around 0.17 eV over the temperature range from 80 K to 300 K.

Based on the temperature dependence of the recombination rate one can estimate the energy position of the band gap levels involved in the recombination. The activation energy of Di recombination was determined by a fit of the temperature dependent PL intensity to a model for a transition between an electronic state in the band gap and the semiconductor bands. [SWS⁺85] The model takes into account that the minority electrons trapped at a certain level in the band gap can be activated thermally back to

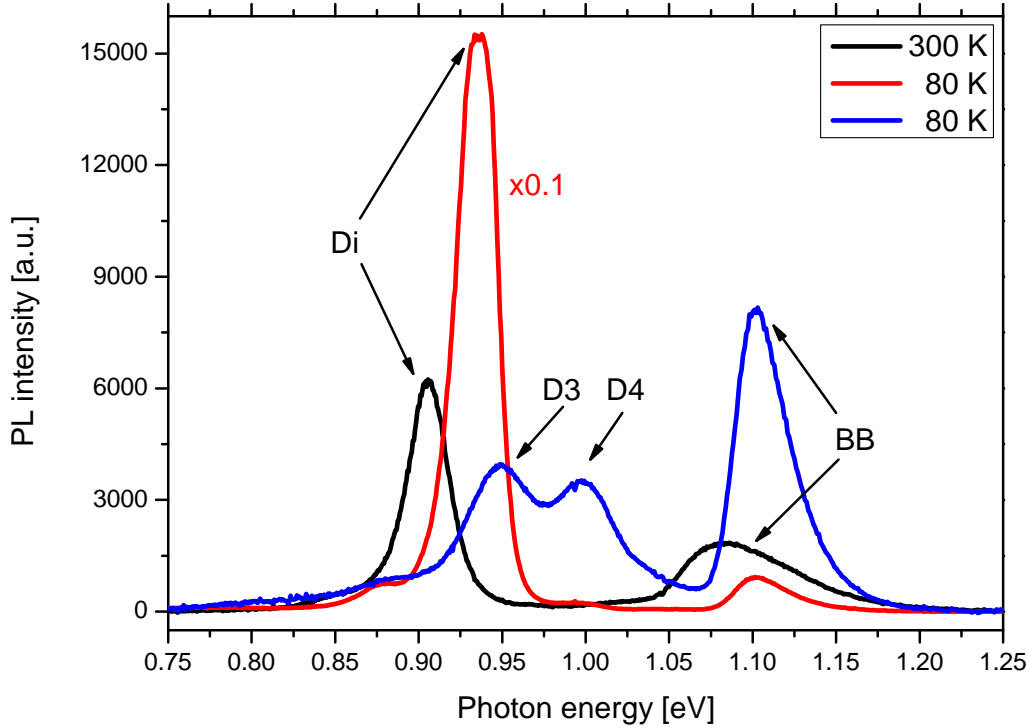


Figure 5.2.: Photoluminescence spectra at room temperature (black) and 80 K (red) at a position with Di luminescence and a 80 K spectrum at a position with ordinary D3/D4 luminescence (blue). Note that the amplitude of the 80 K Di spectrum (red) is reduced 10 times.

the conduction band. It is clear that upon decreasing temperature, the activation process would be suppressed, and, accordingly, the probability for transition of those electrons into the valence band will increase. The energy offset of the defect level can be determined by fitting the experimentally measured recombination rates at different temperatures with [SWS⁺85, Pan75]:

$$R = \frac{1}{1 + CT^{3/2} \exp(-E_A/k_B T)}. \quad (5.1)$$

The recombination rate R is given by the intensity of the photoluminescence signal, C is a constant accounting for the degeneracy factor of the level and the density of states in the band, $k_B T$ is the thermal energy, and E_A is the energy offset between the defect level and the conduction band edge. A value of 120 meV for the activation energy E_A was obtained, which is in good agreement with the previously reported 115 meV [Arg07]. For

PL it is found that the activation energy E_A is in the range between 105 meV and 150 meV; a sample plot is shown in Figure 5.3. It is assumed that a recombination of the minority charge carriers through the estimated level 120 meV beneath the conduction band in p -type silicon is present. [KMK⁺13]

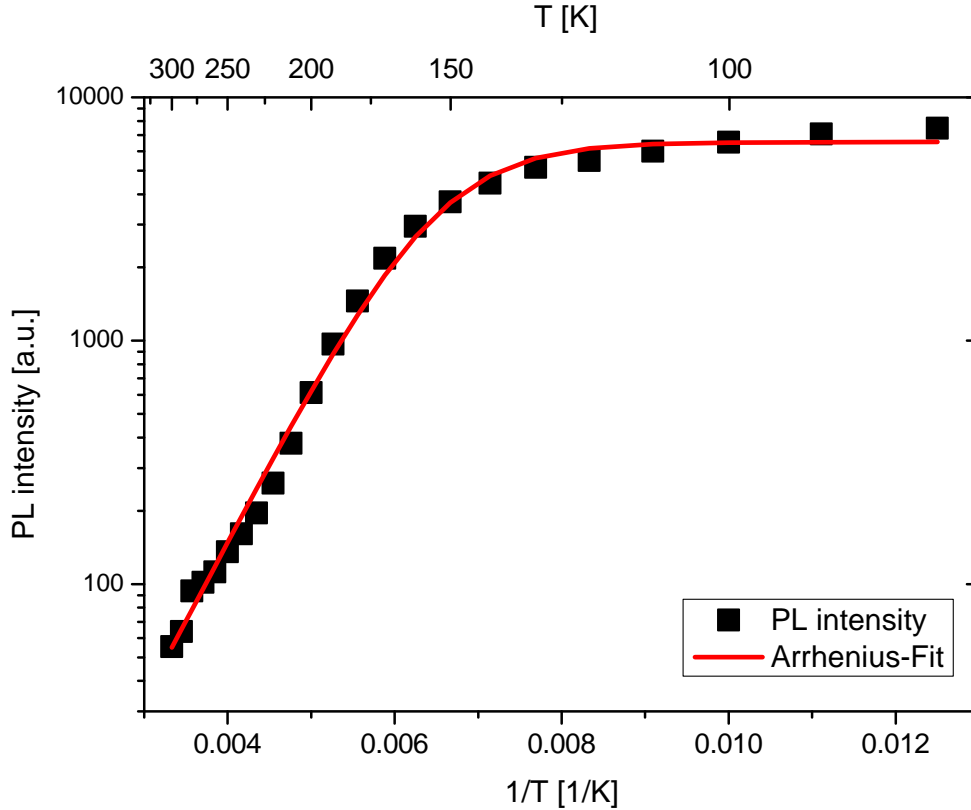


Figure 5.3.: Arrhenius plot for the radiative recombination activity (PL) with a best fit to the model for a grain boundary emitting strong Di radiation. Calculated activation energy: $E_A = 130$ meV.

The energy barrier of 120 meV, obtained by temperature dependent PL, CL and EBIC analysis (cf. [KAS⁺13, KMK⁺13]), would support the involvement of Frank partials as well. It has been found that Frank partials introduce similar level in the band gap of silicon [KLP77, BKP⁺97]. The estimated activation energy of the level involved in the transition is in agreement with those given in by the groups of Kimerling and Bo [KLP77, BKP⁺97]. Moreover, the photon energy of the radiative transition is also in good agreement with that theoretically estimated for transition at Frank partials. Indeed, the band gap narrowing

due to the strain field around Frank partial dislocation [LRR⁺92] results in an energy of 0.9 eV, the value is fairly well consistent with the experimentally observed 0.93 eV photon energy of Di emission.

In the majority of cases, this line appears singly besides the band-to-band transition, but in some cases, a second broad peak, centered at 1600 nm, is observable at 80 K. This second peak will be described in the following.

5.1.2. Oxygen-related luminescence

Still under discussion is the origin of the D1 line in silicon. Room temperature investigations only are not feasible to detect the origin of the luminescence in the range between 1500 nm and 1650 nm. Here, low temperature measurements are necessary. In the wavelength range mentioned before different peaks at low temperature can be detected, depending on its origin. Photo- or electroluminescence imaging at room temperature could show all defects emitting light in the range between 1500 nm and 1650 nm. Low temperature measurements, at about 80 K, show differences in the temperature behavior of the detected peaks. On one hand one can find the typical D1 line, which shifts to higher energies during cooling, on the other hand another peak is found, which shifts lower energies during cooling. In Figure 5.6 two sample spectra are given, which show the peak at 0.77 eV (1600 nm). The black curve shows only one peak besides the band-to-band transition, whereas the red curve shows additionally a Di peak. The new peak at 0.77 eV is denoted as OP.

It is still not clear if the D1 and OP luminescence bands have the same origin. In my opinion there has to be a difference between them, because of the different photon energies and intensities, and the temperature behavior. Figure 5.5 illustrates that. In the upper left image, a band-to-band luminescence map at 80 K is shown to give an overview of the distribution of recombination active grain boundaries of the sample. The upper right image shows the distribution of the Di luminescence at 80 K in the same sample. The lower images depict the luminescence intensity maps at 80 K at 0.81 eV (left) and at 0.77 eV (right), respectively; note the same measurement conditions and scales on the lower images. In this sample, the Di luminescence appears on some defined grain boundaries or in regions of grain boundaries, where no other luminescence is detectable. The two marks A and B in the lower images show the positions of the spectra shown in Figure 5.6.

It is apparent that the luminescence intensities of the 0.81 eV and 0.77 eV maps are different. Furthermore, one can see that the D1 luminescence has a line character at the

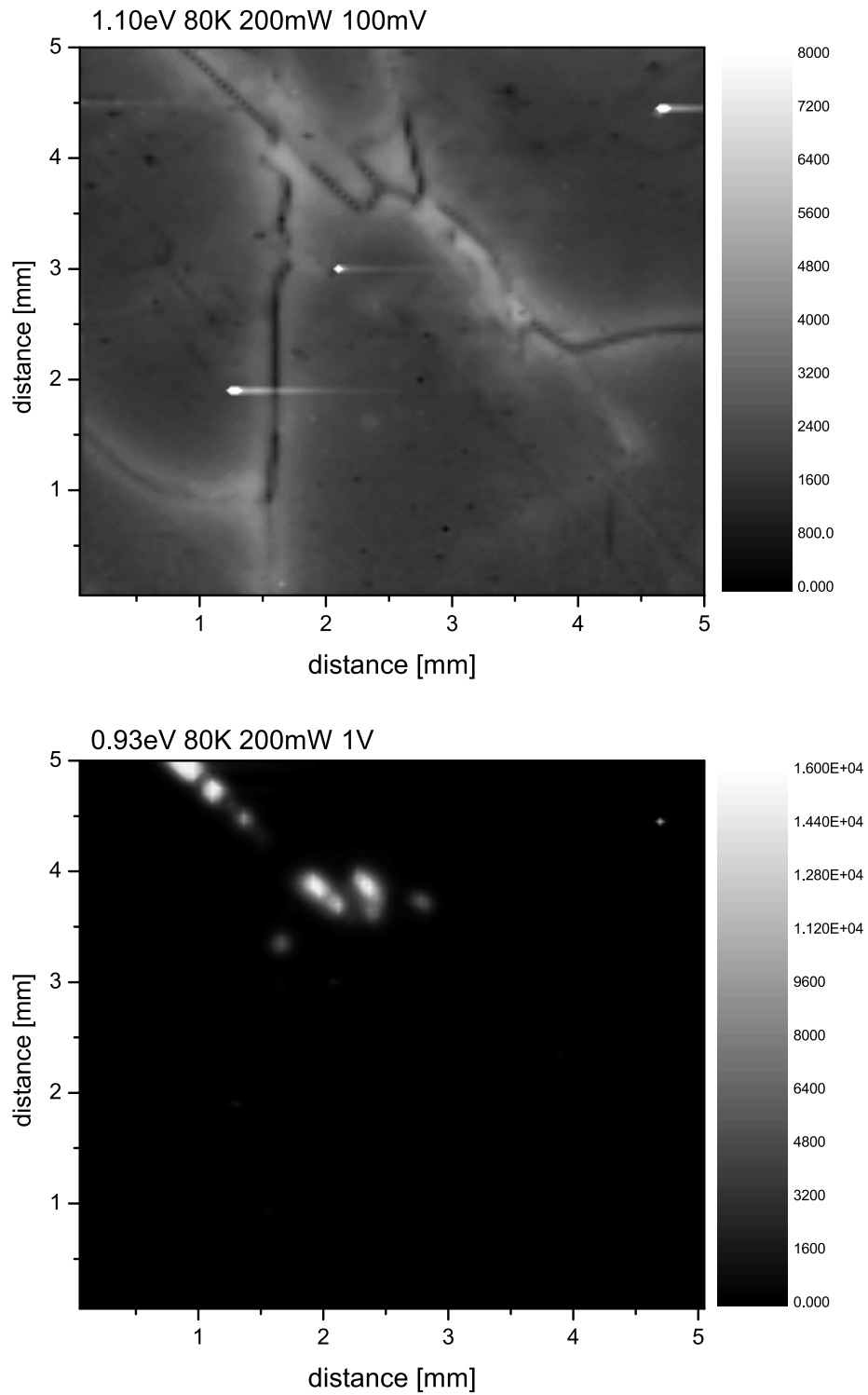


Figure 5.4.: Photoluminescence maps at 80 K showing band-to-band luminescence (top) and Di luminescence (bottom). The corresponding D1 and OP photoluminescence maps are given in Figure 5.5.

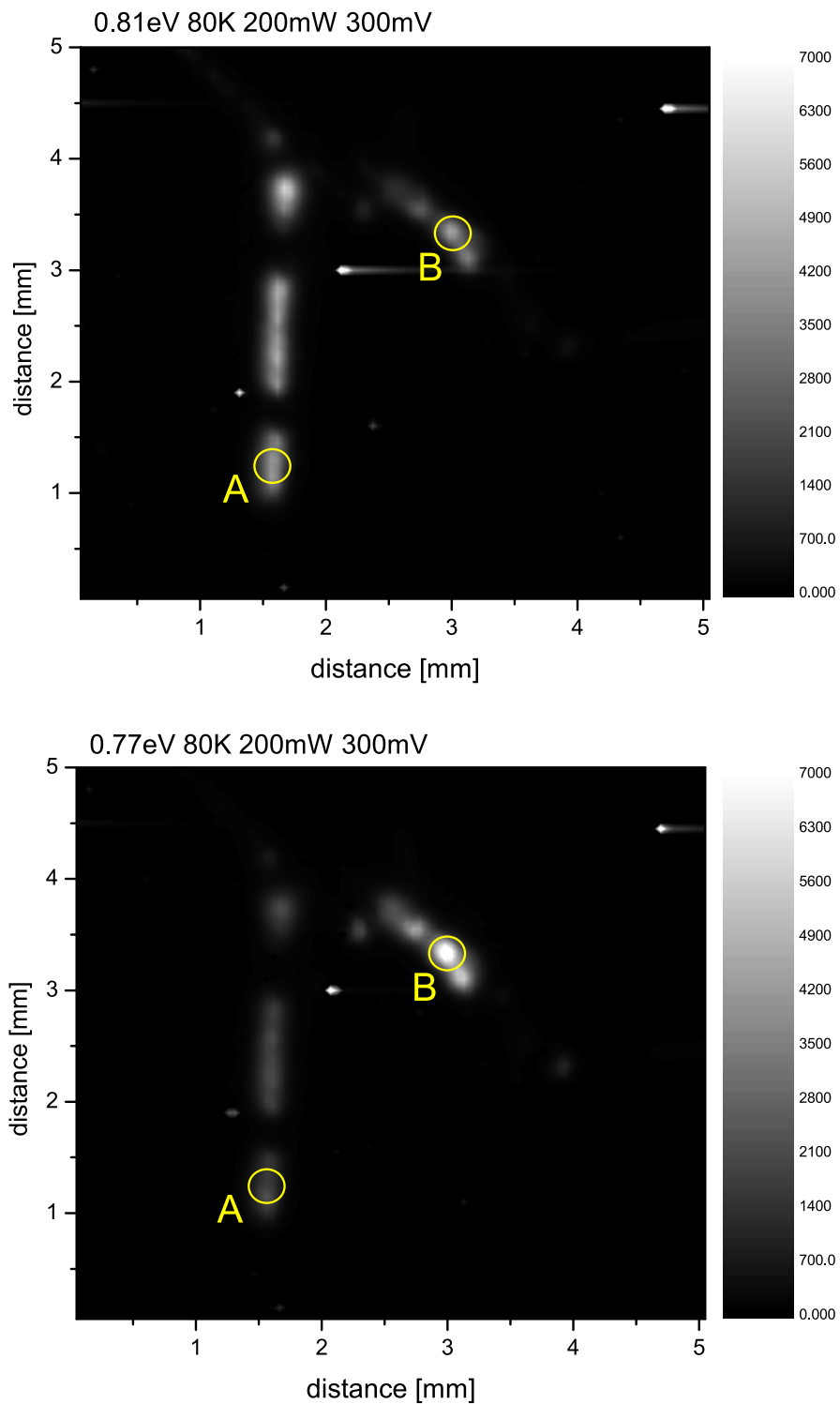


Figure 5.5.: Photoluminescence maps at 80K showing D1 luminescence (top) and OP luminescence (bottom). Corresponding BB and D1 map can be found in Figure 5.4 The two marks A and B show the positions for the recorded spectra shown in Figure 5.6.

grain boundaries, whereas the OP luminescence appears rather “dot-like”. This “dot-like” appearance is typical for this kind of luminescence. Due to the width of the peaks, it seems probable that these peaks are convolution of several lines. Thus, the peaks were deconvolved, which is shown in Figures 5.7(a) and 5.7(b) for the OP and D1 peak, respectively. The peak center of the OP peak in Figure 5.6 is found to be at 0.778 eV, whereas the peak center of the D1 peak is at 0.810 eV. For the deconvolution of the OP peak, three lines are necessary, the centers are located at 0.740 eV, 0.777 eV and 0.811 eV, where the 0.777 eV peak is the main peak and the 0.811 eV should be the D1 line. The Di line is located at 0.92 eV in this case. Deconvolving the D1 peak leads to three sub-peaks as well. The centers are located at 0.777 eV, 0.807 eV and 0.845 eV. The first one should belong to oxygen and the second and main peak is D1 radiation. The third peak belongs to D2 radiation or is oxygen-related as well.

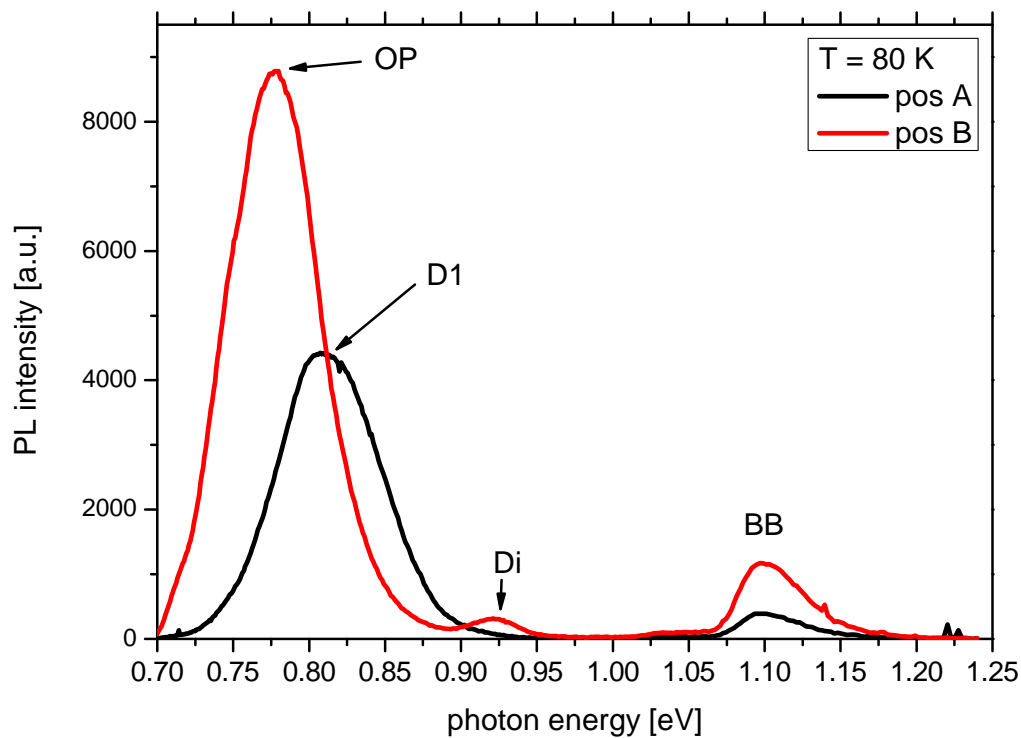
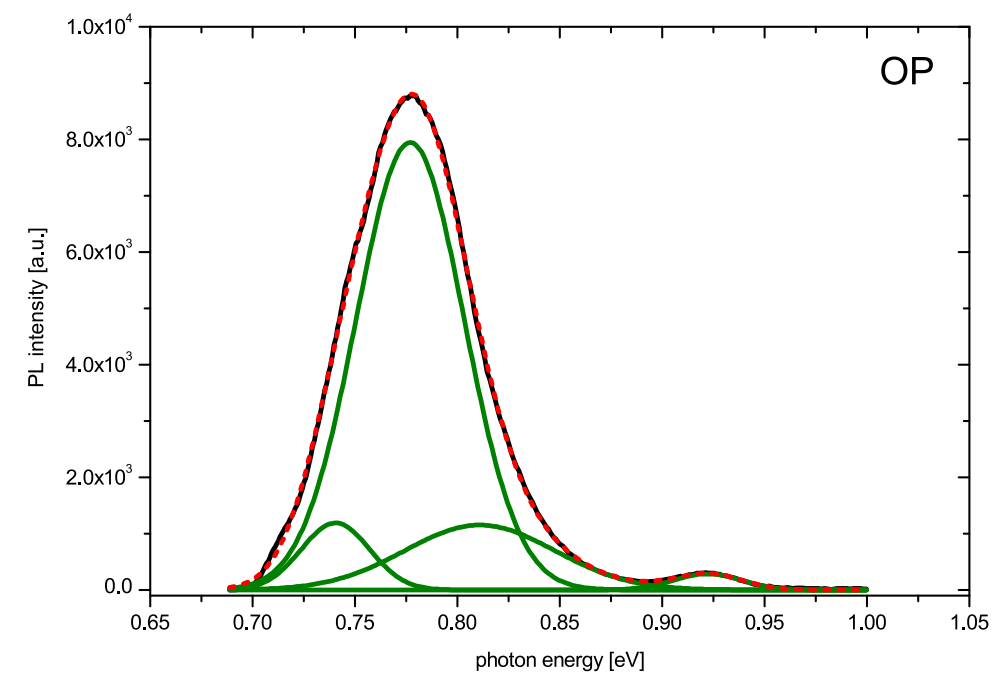
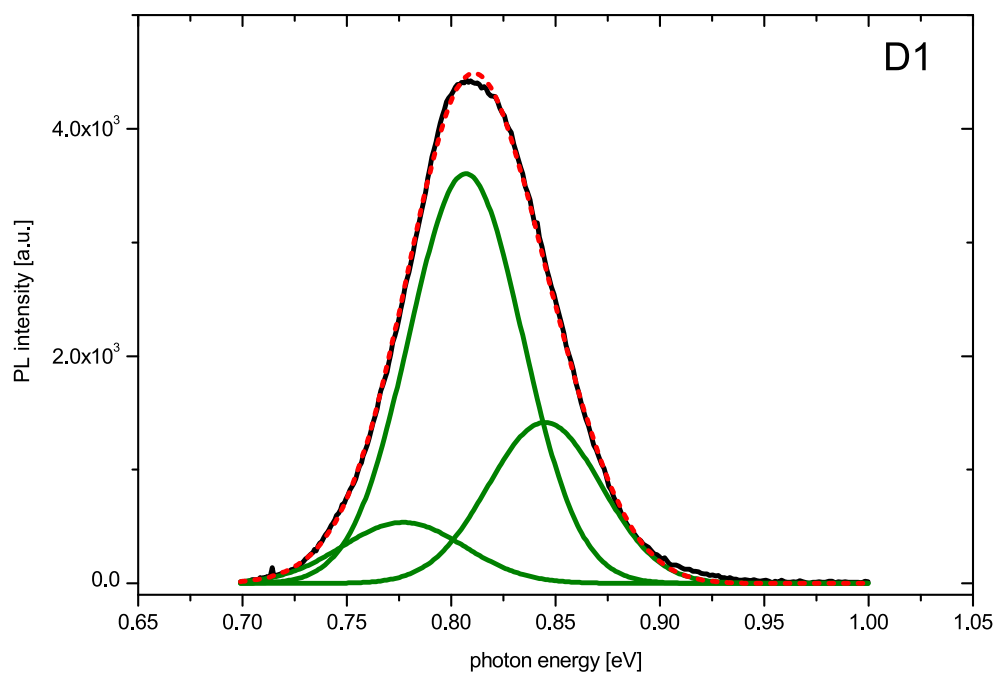


Figure 5.6.: Photoluminescence spectra at 80 K of the two marked positions in Figure 5.5..

Minaev and Mudryi [MM81] investigated heat-treated Cz-Si crystals by low temperature



(a) Deconvolution of the OP peak.



(b) Deconvolution of the D1 peak

Figure 5.7.: Photoluminescence spectra of two different position (cf. Fig. 5.6) showing the OP and D1 peaks, and deconvolution of the OP peak (a) and the D1 peak (b). The black lines in (a) and (b) are the measured data, the red dashed lines are the sum of the green lines, which denote the sub-bands.

photoluminescence. They found in the 15 K luminescence spectrum two bands called the “P”-line at 0.7667 eV and the “H”-line at 0.9259 eV. They concluded that these bands are due to thermally induced defects, i.e. oxygen thermal donors. These bands have been observed in luminescence spectra of Cz-Si irradiated by high-energy particles, too. Further, they suggested that vacancies in the oxygen containing thermal defect generation process are involved.

Later, Kürner et al. [KSDT89] reported about low temperature luminescence lines located at 0.767 eV and 0.79 eV denoted as the “P”- and “C”-line, respectively. They assume that both lines are affected by oxygen and/or vacancies and carbon. It could be possible that these lines are comparable with the lines found here, but here, multicrystalline silicon was observed which was not intentionally heat treated or annealed.

First observations of Tajima et al. [TTA92] on Cz-Si lead to the detection of a deep level emission at 0.77 eV at room temperature. Later, Tajima et al. [TTW95, IST+08, TIO+12] observed the 0.777 eV line at multicrystalline silicon, too, but they found it at room temperature and not at liquid nitrogen temperature as it was observed in this work. Inoue et al. [IST+08] suggested that the 0.78 eV band at room temperature is associated with oxygen precipitation, and that the intra-grain defects are dislocation clusters decorated with not only heavy-metal but also oxygen impurities. Pizzini et al. [PLB+04] mentioned that in all sub-bands of the D1 line oxygen could play a role, but the type of dislocations, where oxygen phases could agglomerate, are relevant as well.

Kenyon et al. [KSP+03] studied the influence of implanted impurities on luminescence in the region of the D1 luminescence band. They deposited layers of $\text{Si}_{0.9}\text{Ge}_{0.1}$ onto single-crystal silicon substrates by MBE to induce dislocations in the silicon substrate. The samples have been subsequently implanted with iron, erbium or oxygen to study the effect of implanted impurities on D-band photoluminescence at around 0.8 eV at liquid nitrogen temperature. After deposition, the samples were divided into two sets. Both sets were etched; one remaining a 100 nm SiGe, on the other set the entire SiGe layer was removed. In the former case, with a thin SiGe layer, the unimplanted sample showed a broad peak at around 0.810 eV with a less intense side band at 0.86 eV, which corresponds to D1 and D2 luminescence. Oxygen implantation produces a shift in peak energy to around 0.825 eV, and the low-energy side of the peak were enhanced. The deconvolution of this peak yielded to three lines, one due to dislocations, centered at 0.820 eV, and two bands centered at 0.778 eV and 0.850 eV, respectively. On the sample with fully removed SiGe layer, no D1 luminescence was detectable. Here they observed bands at 0.780 eV and 0.850 eV only;

these lines correspond to the positions of the former sample. The unimplanted sample of this set showed no luminescence in this region. A comparison of the lines found in this work and by Kenyon et al. is given in Table 5.1, note that all measurements were made at around 80 K. Remarkably, the lines found by [KSP⁺03] et al. for the oxygen-implanted sample fit well to the “D1” line found in mc-Si in this work. Assuming the data of Kenyon et al. and the data from this work, two lines belong to oxygen-related luminescence, i.e. at around 0.78 eV and 0.85 eV, whereas the line at around 0.81 eV is responsible for the D1 luminescence.

	Kenyon et al. [KSP ⁺ 03]		this work	
	w/ SiGe	w/o SiGe	defect	line deconvolution
no implantation	810 meV (D1) 860 meV (D2)	no luminescence	“D1”	777 meV (oxygen-related) 807 meV (D1) 845 meV (oxygen-related?)
oxygen implantation	778 meV 820 meV 850 meV	780 meV 850 meV	“OP”	740 meV 777 meV (oxygen-related) 811 meV (D1)

Table 5.1.: Comparison of deconvolved lines for oxygen related luminescence after Kenyon et al. and lines found in this work at about 80 K.

Additionally, temperature dependent measurements were conducted and it was found, that the oxygen-related peak shifts unexpectedly in the opposite direction as the band-to-band peak. This behavior, shown in Figure 5.8, is opposing to that mentioned by Tajima et al. [TIO⁺12]. Thus, the oxygen-related defect is not linked to the band edges, because it does not shift parallel with the band edge narrowing due to temperature rise. Since the D1 peak shifts parallel with the band-to-band peak and the oxygen-related peak in the opposite direction during heating from 80 K to 300 K, both peaks “meet” at about 0.80 eV at room temperature. Thus, with room temperature luminescence imaging and spectroscopy it is not possible to differentiate between both lines.

Another hint for the involvement of oxygen could be the appearance of the Di line in some cases. It is known that oxide precipitates are formed by agglomeration of interstitial oxygen O_i . A small oxide precipitate, especially if it is not spherical, has a stress field that helps to nucleate the stacking fault of the interstitials. Thus, the oxide precipitates are surrounded by large stacking faults. Both processes, the oxide precipitation and the stacking fault formation, occur simultaneously; new precipitates may be nucleated at the

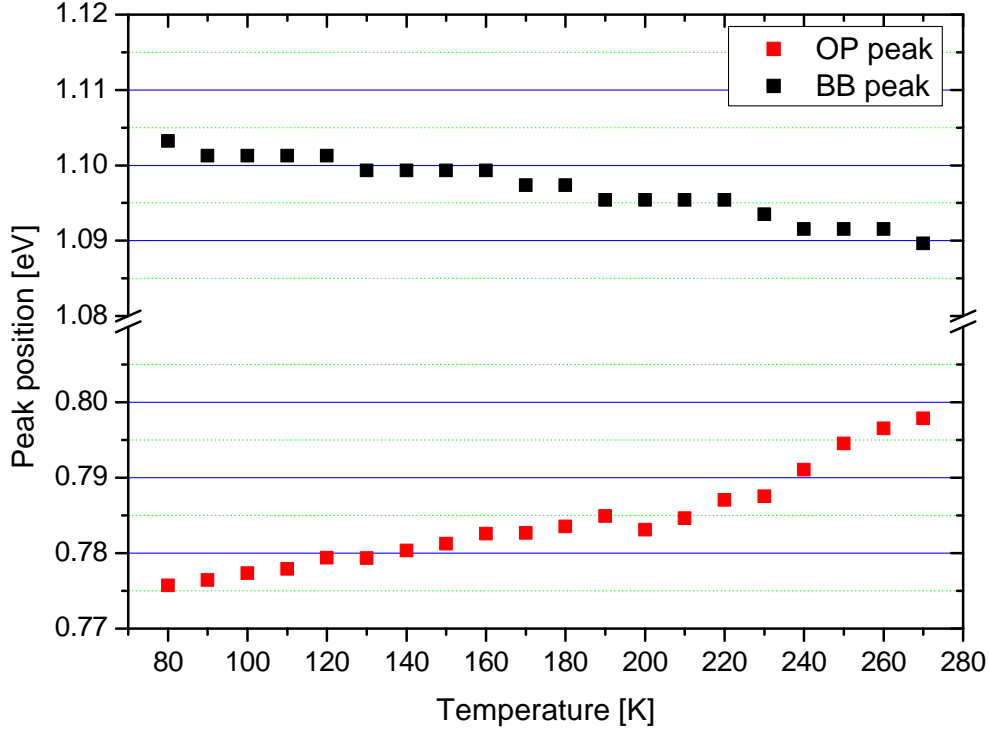


Figure 5.8.: Peak positions in temperature dependent photoluminescence investigations of the OP peak (red) and the band-to-band peak (black).

Frank dislocation and vice versa [Foe14]. These Frank partials were found on specific grain boundaries emitting strong Di luminescence, cf. section 5.1.1.

The OP peak shift follows in principle an inverse of the Varshni formula, which can be seen in Figure 5.9. The equation was set to

$$y = \frac{A}{E_g(T)} - B, \quad (5.2)$$

wherein

$$E_g(T) = E_g(0) - \frac{\alpha T^2}{T + \beta} \quad (5.3)$$

with $E_g(0) = 1.17$ eV, $\alpha = 4.73 \cdot 10^{-4}$ eV/K, $\beta = 636$ K, and T the temperature. The cause of the deviation of the data point at $T \geq 200$ K should be the cryostat, because at those temperatures the cryostat is not stable.

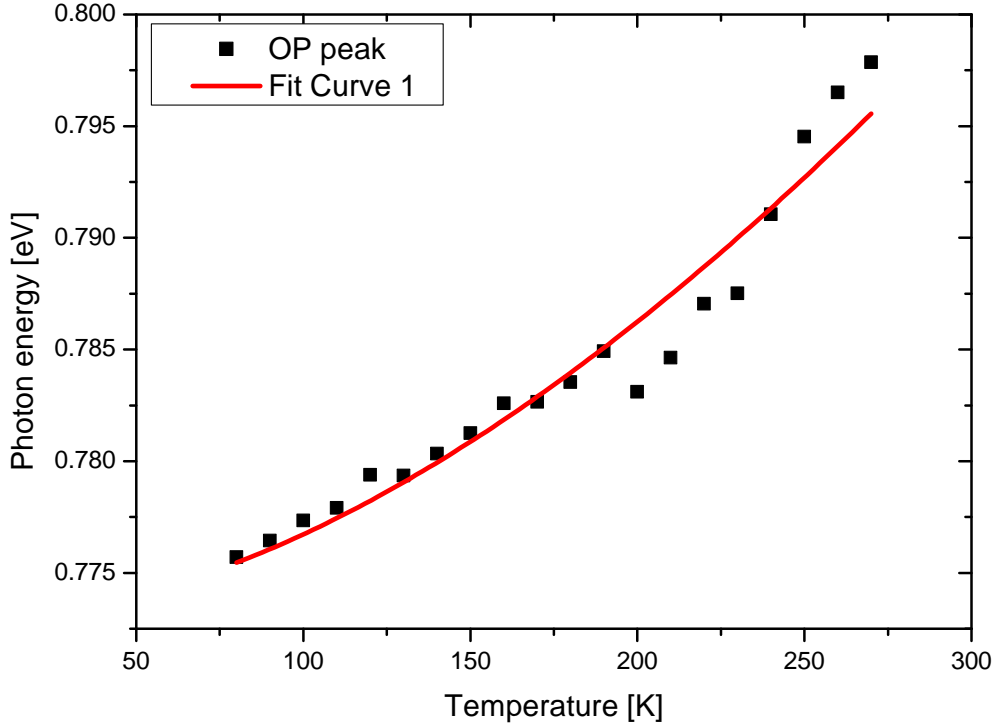


Figure 5.9.: OP peak position (black) and an inverse plot of a varied Varshni fit.

On the contrary an independent temperature behavior of oxygen-related defects or oxygen precipitates (P line) is reported in the literature [MM81, BFM12, TTA92]. Those are depicted in Figure 5.10.

D1 luminescence by way of comparison

Electroluminescence investigations of dislocation loops suggest a two-level model for the D1 luminescence. It was deduced by Kittler et al. [KMA⁺09] from analysis of data measured as a function of temperature and excitation level. Accordingly, a shallow level $E_s \approx 0.09$ eV from one band edge and a deeper level $E_d \approx 0.29$ eV from the other band edge are found. The sum $E_g = E_s + E_d + E_{D1}$ (with $E_{D1} \approx 0.8$ eV) is close to the energy of the silicon band gap. A scheme of the two-level model is shown in Figure 5.11. Here the shallow level is below the conduction band and the deep level above the valence band. It is well-accepted that shallow dislocation levels (or shallow 1d-bands) are caused by the dislocation strain

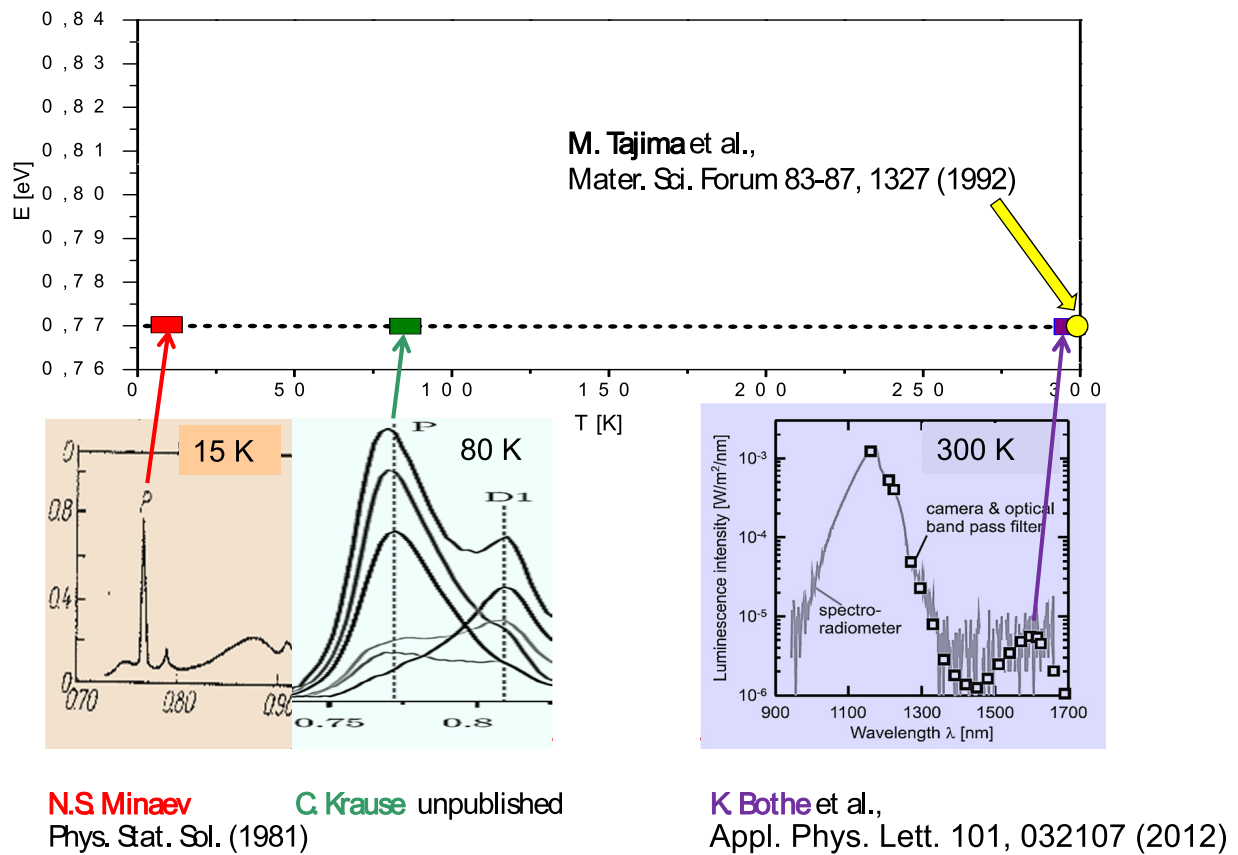


Figure 5.10.: Luminescence of oxygen-related defect / oxygen precipitates from literature. The P line seems not to depend on the temperature. After [KAR⁺14].

field (e.g. [VVK08]). DLTS analysis of thin film solar cells made from microcrystalline silicon confirms the existence of these levels [MK12]. A robust donor level, 0.27 eV above the valence band, was found and could be clearly related to D1 luminescence.

The temperature behavior of the D1 line $E_{D1}(T)$ is expected to correspond with the gap temperature behavior $E_g(T)$, under the assumption that the energy of the shallow and deep level do not depend on T . Therefore, the sum $\Delta = E_s + E_d$ does not depend on T and one gets

$$E_{D1}(T) = E_g(T) - \Delta. \quad (5.4)$$

Experimental data shown in Figure 5.12 confirm this assumption quite well.

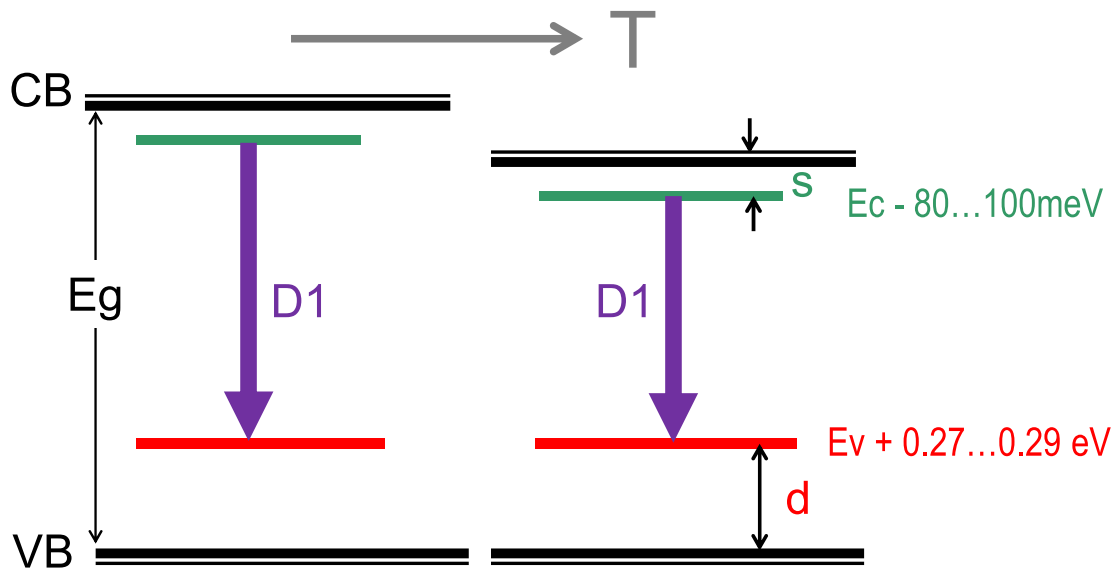


Figure 5.11.: D1 two level model. D1 emission between shallow level (s) below conduction band and deep level (d) above valence band. The D1 temperature behavior follows $E_g(T)$. After [KAR⁺14].

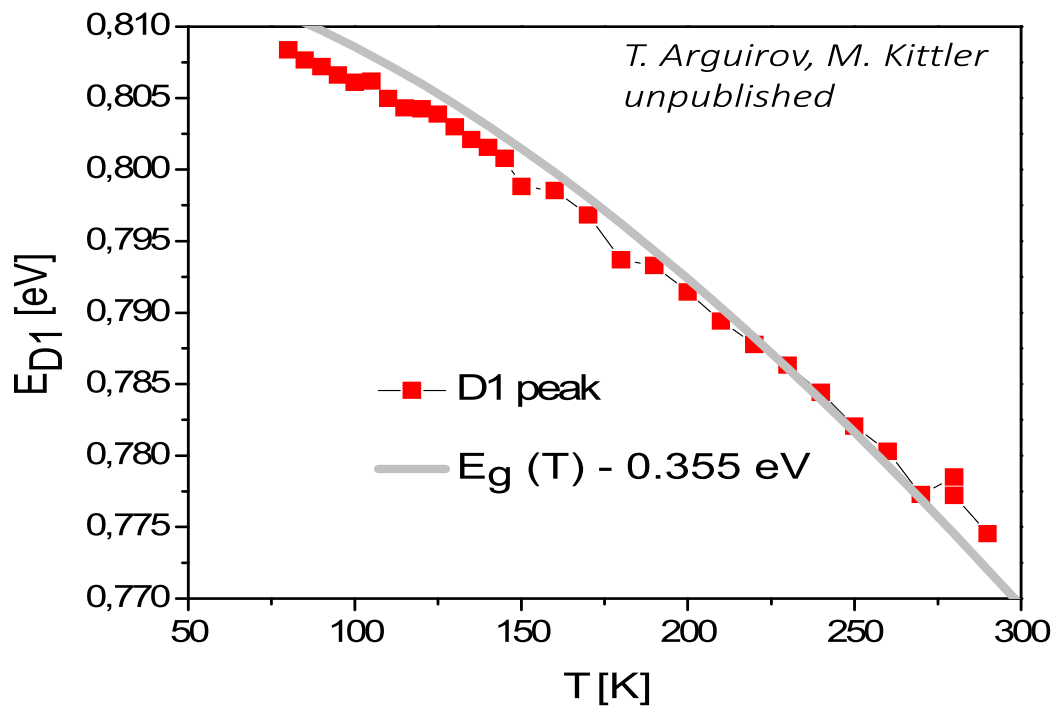


Figure 5.12.: D1 temperature behavior $E_g(T) - 0.355 \text{ eV}$ was found for end-of-range-defects in diodes prepared by boron implantation into n -type Si. For the calculation of $E_g(T)$ Thurmond's relation was used [Thu75]. After [KAR⁺14].

A wide variety of energies can be found in the literature for the D1 peak position ranging between about 0.76 eV and nearly 0.84 eV. Kveder et al. [KBS⁺04] report the temperature behavior $E_{D1}(T) = E_g(T) - 0.363 \text{ eV}$ for the D1 peak position of dislocations produced by plastic deformation of float-zone silicon. For dislocation networks - produced by Si wafer direct bonding - for the D1 peak position larger energy values were observed by Arguirov [Arg07], which follow $E_{D1}(T) = E_g(T) - 0.335 \text{ eV}$. Figure 5.13 shows the domain formed by T -dependencies reported in [KBS⁺04] and [Arg07], showing an energetic width of $W \approx 30 \text{ meV}$. The appearance of the 30 eV wide domain can be explained by the influence of an electric field and elastic stress on the D1 peak position.

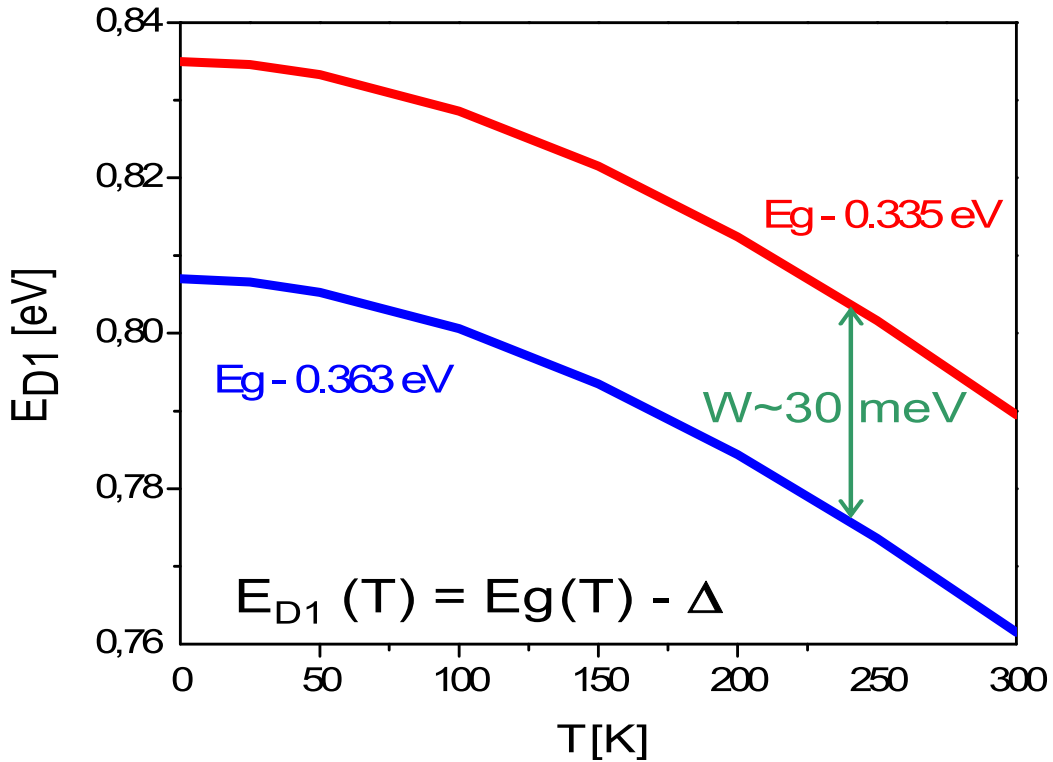


Figure 5.13.: Experimentally observed domain of D1 peak position exhibiting an energetic width of $W \approx 30 \text{ meV}$. Most of the reported D1 positions fall into this domain. After [KAR⁺14].

Present luminescence data suggest clear difference of the temperature behavior of the D1 line, the P line and the oxygen-related line found in this study (cf. Figure 5.14). The dislocation-related D1 line shows a $\approx 30 \text{ meV}$ wide domain and the P line seems not to be influenced by temperature change. Hence, in this work a blue shift of the oxygen-related peak with increasing temperature was observed. A proof for the P line is still missing,

especially regarding the influence of electric fields and/or elastic stress. For a possible statistical analysis of the supposed oxygen-related luminescence comparative investigations of Fourier-transform infrared spectroscopy and photoluminescence were conducted, which is explained in chapter 7.

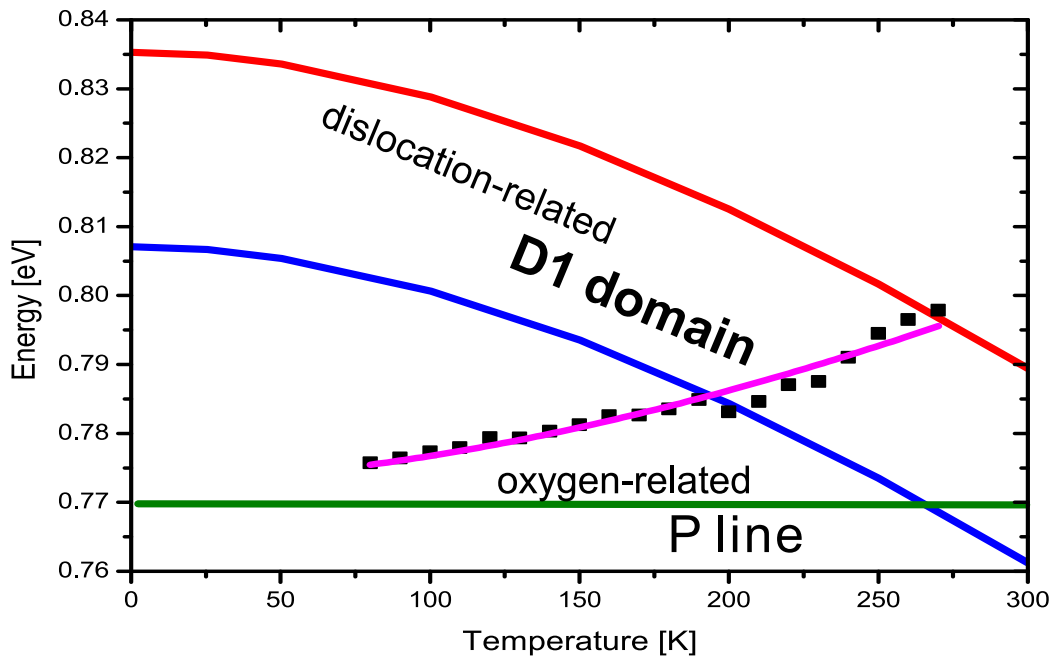


Figure 5.14.: Comparison of D1 and P line luminescence and the new oxygen-related luminescence line (black squares).

5.2. Polycrystalline silicon thin film on glass substrate

In this section, silicon thin film material on glass substrates is investigated by photoluminescence mapping and spectroscopy. These silicon thin films have a thickness of about $10\ \mu\text{m}$. They are produced as described in Section 1.4, but they are only at the stage after crystallization. Due to the thickness of the silicon layer, the crystals seem similar to that of multicrystalline wafer material. Differences are the directional solidification of the crystals and the barrier layer, which influences the recombination at the interface between silicon layer and barrier layer. According to this, one could expect that the investigation should be similar to that on bulk wafer material, but little differences in investigation techniques exist. One important point is the glass substrate, the cryostat gives only the temperature of the specimen table, but glass is a poor heat conductor, consequently the

real temperature of the silicon layer is not sure, but the difference cannot be larger than 10 K. Measuring from the opposite side would eliminate this circumstance, but then the glass signal would dominate in the silicon spectrum. Another point is the injection energy of the laser, one has to be very careful with laser power, and otherwise one could destroy the layer or initialize re-crystallization.

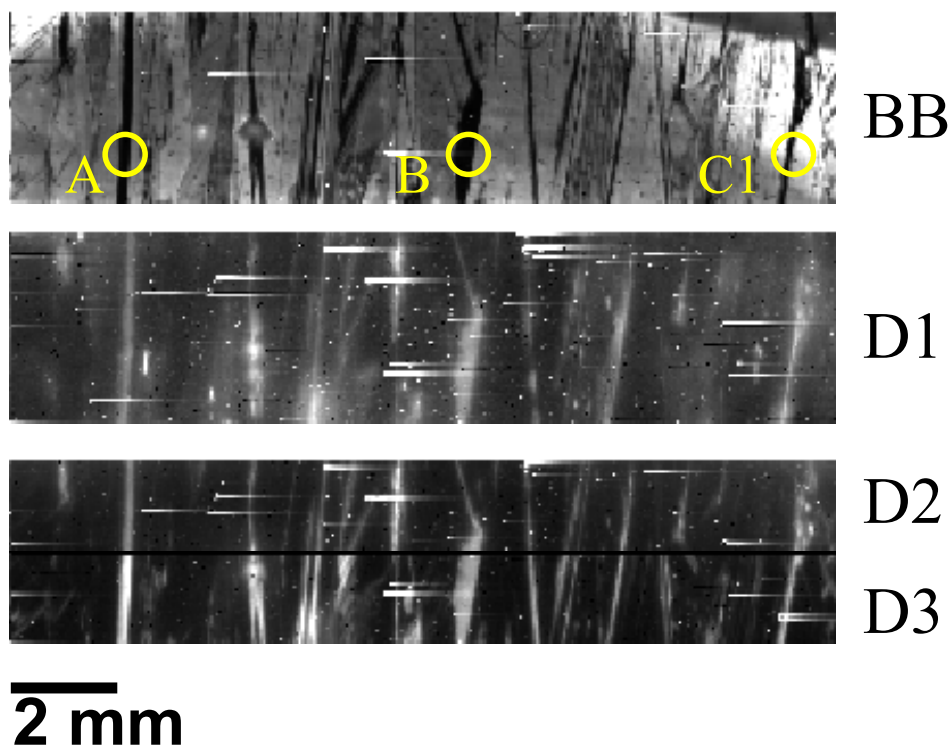
In this section, two different samples are shown and discussed. The first sample was crystallized once, whereas the second one has been crystallized twice. The second crystallization was performed in a direction perpendicular to the first crystallization. Both samples were then investigated at about 80 K by scanning photoluminescence and additionally some spectra were taken.

5.2.1. One crystallization step

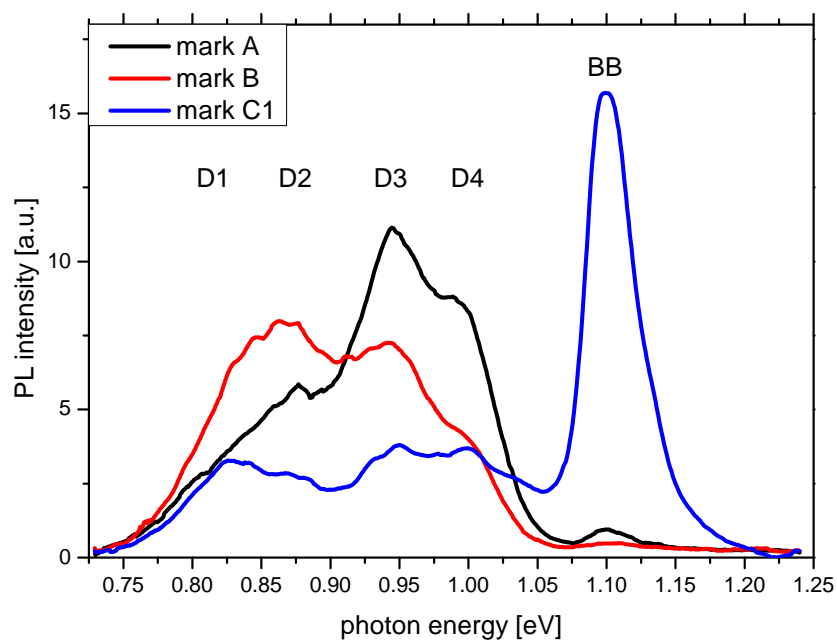
The sample discussed here has undergone only one crystallization process. In Figure 5.15(a), the photoluminescence maps at 80 K are depicted. The upper map is the band-to-band map (1.10 eV), the middle is the D1 map (0.81 eV), and the lower is a composition of D2 (0.87 eV) and D3 (0.94 eV), where the upper part shows D2 and the lower D3. These maps show the same region of the sample. The horizontal white stripes are artifacts and the yellow marks indicate the areas where spectra are taken, which can be seen in Figure 5.15(b). Comparing the band-to-band and the defect-related luminescence maps, an almost anti-correlation is visible. The band-to-band map correlates with the lifetime of the minority charge carriers. The dark regions in the band-to-band map indicate dislocation-rich regions, too. This can also be seen in the defect-related luminescence maps. The defective regions are not only grain boundaries, as typical for bulk multicrystalline silicon, there are as well a few dislocation-rich grains.

Considering that the gray scales for all maps are the same, differences in the intensities of the defect-related luminescence are observable. This could be an evidence for different types of dislocations or other defects in the respective regions. For instance, comparing the marked areas “A” and “B”, the difference in the D3 luminescence intensity is remarkable. This is also apparent from the spectra shown in Figure 5.15(b). At point “A” the D3 line is dominating, whereas in point “B” the D2 and D3 lines have almost the same intensity. Furthermore, the band-to-band luminescence is in these regions nearly completely suppressed. In regions with dominating D3/D4 luminescence, clean dislocations are dominant.

In region “C1”, the band-to-band luminescence is rather intense, whilst the defect-related luminescence intensities are weaker than in points “A” and “B”. The reason for that is that



(a) Photoluminescence maps at 80 K of the sample with one crystallization step with marks for the taken spectra. The horizontal stripes are artifacts.



(b) Photoluminescence spectra at 80 K at the marked positions in Figure (a).

Figure 5.15.: Photoluminescence maps and spectra at 80 K at the marked positions in Figure (a).

the laser spot did not hit the defective region here; it is located closer to the defect-free grain. In addition, here defect-related luminescence can be detected, whereby the four lines D1 to D4 have nearly the same intensity.

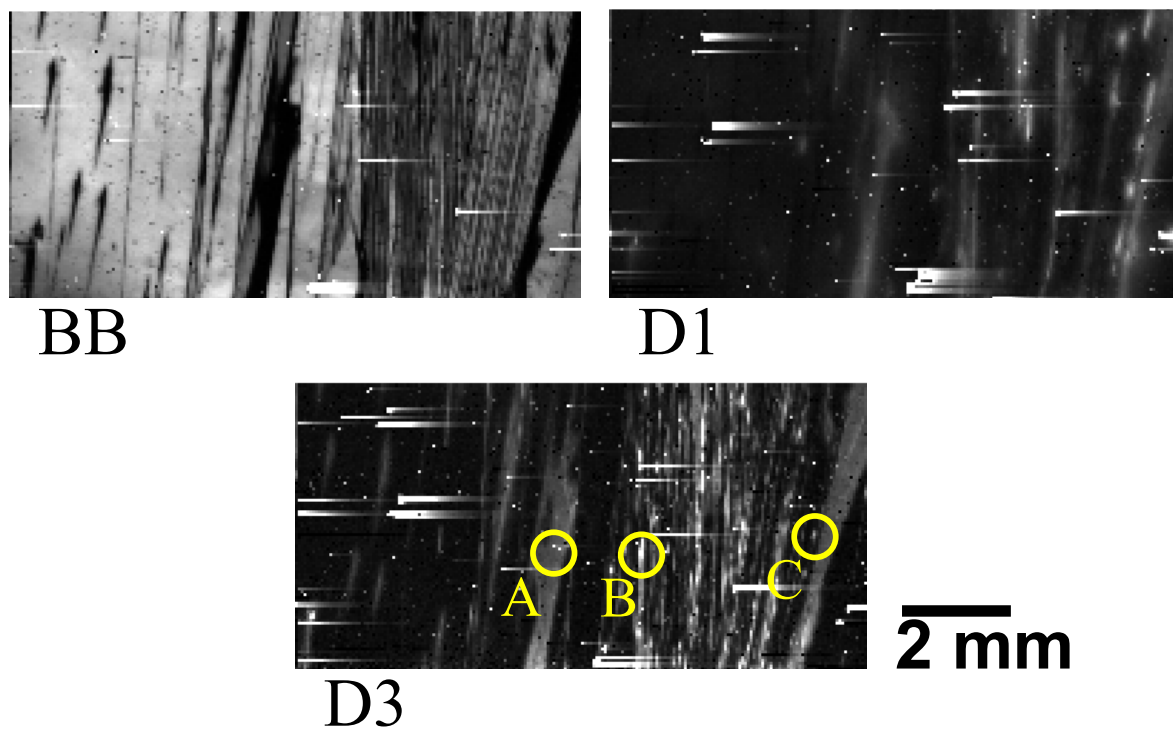
5.2.2. Two crystallization steps

Here a sample is discussed, which was crystallized two times. Figure 5.16(a) shows the photoluminescence maps at 80 K. The upper left is the band-to-band map (1.10 eV), the upper right is the D1 map (0.81 eV), and the lower depicts D3 (0.94 eV) luminescence. These maps show the same region of the sample. The horizontal white stripes are artifacts and the yellow marks indicate the areas where spectra are taken, which can be seen in Figure 5.16(b). Similar to the sample, which was crystallized once, by comparing the band-to-band and the defect-related luminescence maps, an almost anti-correlation is visible. The band-to-band map depicts the lifetime of the minority charge carriers. The dark regions in the band-to-band map indicate dislocation-rich regions. This can also be seen in the defect-related luminescence maps. Here the defective regions are mainly grain boundaries, and some dislocation-rich grains can be found.

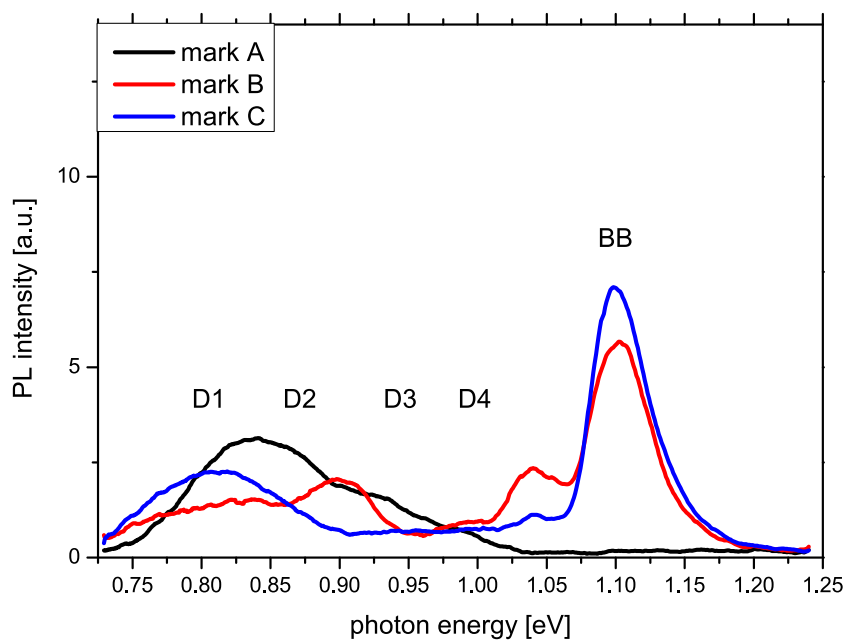
The gray scales in these maps are the same as well. The spectrum at position “A” shows no band-to-band radiation, this could mean, that this grain and/or grain boundary is very dislocation-rich and furthermore very high contaminated with transition metals. The defect-related luminescence at these points gives no hint, which kind of dislocations may be present. The spectrum at point “B” (cf. Fig. 5.16(b) red curve) looks more like a composition of “Di” and “OP” luminescence (cf. Subsections 5.1.1 and 5.1.2). It could be possible that at this point during crystallization, the silicon layer was damaged strongly and some impurities from the glass substrate incorporated after re-crystallization. The broad peak in the D1 region of the spectrum at mark “C” seems to be correlated to oxygen-related luminescence, due to the shoulder at the red side of the spectrum. Dominating D1/D2 luminescence stands for complex dislocation structures, particularly with contamination.

5.3. Summary

A new, very intense, defect line in multicrystalline silicon could be observed. This so-called “Di” line is located near the D3 line, but can be detected even at room temperature. With decreasing temperature, the luminescence intensity of the Di line increases rather strong. The peak position shifts parallel with the peak position of the band-to-band luminescence



(a) Photoluminescence maps at 80 K of the sample after two crystallization steps with marks for the taken spectra. Horizontal stripes are artifacts.



(b) Photoluminescence spectra at 80 K at the marked positions in Figure (a).

Figure 5.16.: Photoluminescence maps spectra at 80 K at the marked positions in Figure (a).

during cooling. The difference of both peaks is about 0.17 eV in the range between 80 K and 300 K. Cathodoluminescence and EBIC investigations indicate, that grain boundaries emitting Di luminescence, are strongly recombination active. Based on the temperature dependence on the recombination rate the energy position of the band gap levels involved in the recombination could be estimated. It is assumed that a recombination of the minority charge carriers through an estimated level of 120 meV below the conduction band in *p*-type silicon is present.

Still under discussion is the luminescence in silicon in the range of 0.8 eV. It has been shown that in this region D1 luminescence and oxygen-related luminescence is detectable. The deconvolution of the D1 and oxygen-related peaks in the silicon spectrum reveals that in most cases both kinds of defect coexist. For D1 luminescence, a peak at 810 meV is observed, whereas peaks at 780 meV and 850 meV are responsible for oxygen.

Another hint for the involvement of oxygen could be the appearance of the Di line. Oxide precipitates are formed by agglomeration of interstitial oxygen. A small oxide precipitate has a stress field that helps to nucleate stacking faults. Thus, the oxide precipitates are surrounded by large stacking faults. Both processes, the oxide precipitation and the stacking fault formation, occur simultaneously; new precipitates may be nucleated at the Frank dislocation and the other way around. These Frank partials were found on specific grain boundaries emitting strong Di luminescence.

Polycrystalline silicon thin films on glass substrate can be investigated almost like bulk multicrystalline silicon, because of the thickness of 10 μm of the silicon film. The 532 nm laser light has a penetration depth of about 3 μm . One has to be careful with the laser power in order to that the silicon layer would not be destroyed. Furthermore, the sample temperature cannot be determined exactly, because of the glass substrate. Room temperature measurements are unrewarding, because of high surface recombination, whether at the surface or the interface.

In contrast to bulk silicon, defective regions are not only grain boundaries, very defect-rich grains can be found in silicon thin films as well. These defect-rich grains exhibit almost all of the silicon defect lines D1 to D4 at liquid nitrogen temperature. A second crystallization procedure seems to decrease the intensity of defect-related luminescence in defective regions of the material.

6. Electroluminescence imaging

In this chapter, electroluminescence measurements with an InGaAs camera are presented (cf. Section 3.2). Here two different cell types are studied: (*i*) multicrystalline silicon solar cells and (*ii*) cells made of polycrystalline silicon on glass substrate are investigated under forward and reverse bias.

6.1. EL on mc-Si solar cells in forward and reverse bias mode and EBIC

It is well known that breakdown sites in multicrystalline silicon solar cells can cause a damage of entire solar modules. When a cell in a module is broken or shaded, the cell may become reverse biased by other cells in a string. This can lead to hot spots within the cell, which may cause a thermal destruction of the module. Three types of breakdown appearing in different reverse bias ranges are described so far. Between -4 and -9 V there is early breakdown (type 1), which is induced by aluminum contamination at the wafer surface. Between -9 and -13 V defect-induced breakdown (type 2) dominates. This breakdown site is attributed to metal-containing precipitates lying within recombination active grain boundaries. Beyond -13 V, avalanche breakdown (type 3) can be found. It is supposed that this breakdown type occurs at etch pits produced during cell process [BBB⁺11]. However, the origin of breakdown behavior in silicon solar cells is still discussed.

In this work, potential relationships between the luminescence caused by breakdown and defect-related luminescence, especially D1, are studied. Indeed, microscopic imaging is an essential tool for establishing a relation between extended defects and breakdown sites.

6.1.1. Samples and measurements

Solar cells made of upgraded metallurgical grade silicon are investigated. To perform microscopic investigations samples were cut out of standard industrially processed solar

cells to a size of $12 \times 12 \text{ mm}^2$. The setup was applied as described in section 3.2, whereby the electroluminescence setup was equipped with an optical microscope for microscopic images. The achievable resolution was about $1.5 \mu\text{m}$. Spectra of the reverse bias electroluminescence (ReBEL) were measured by a spectrometer equipped with a 300 L/mm grating and an InGaAs CCD detector operating at -70°C . For spectroscopic photoluminescence analysis, the setup in section 3.1 was used.

6.1.2. Results and discussion

A typical spectrum of ReBEL and room temperature defect-related PL is shown in Figure 6.1. The ReBEL spectrum shows a broad peak between 1000 and 1800 nm. The PL spectrum of a defective area in the sample is given in Figure 6.1, too. The band-to-band transition is denoted as BB and D1 denotes dislocation-related luminescence. It is noteworthy, that at room temperature the D1 line is detectable only [KOT⁺99]. The radiation caused by the breakdown is obviously not a result of a band-to-band or defect (dislocation) related transition. Moreover, it is assumed that the spectrum shown, is limited by the detection system, and actually extends much farther into the long wavelength range.

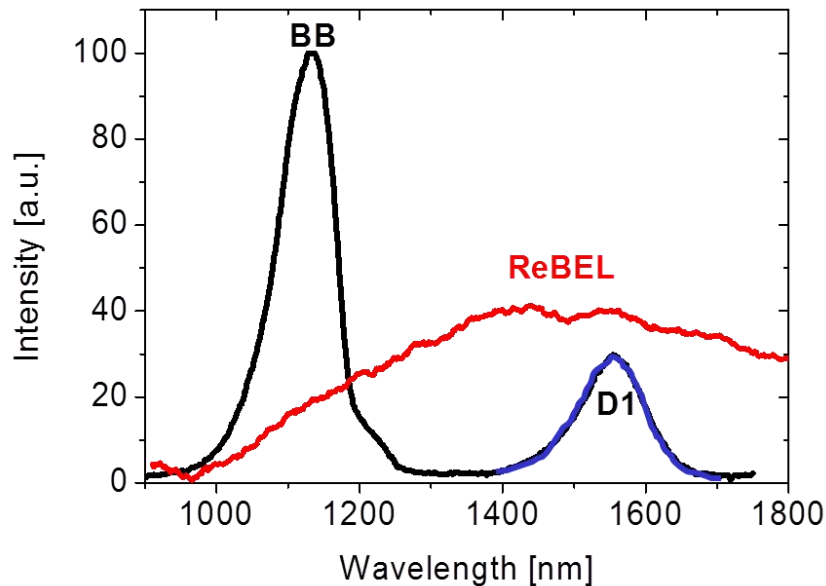


Figure 6.1.: Photoluminescence and reverse bias electroluminescence spectrum of a defective area in multicrystalline silicon. The red curve shows the ReBEL spectrum at room temperature. The black curve depicts a PL spectrum at room temperature on a dislocation-rich region.

An example of luminescence imaging is given in Figure 6.2. The images were taken on a standard 6-inch solar cell made of upgraded metallurgical grade silicon. Figure 6.2(a) shows a band-to-band electroluminescence image under forward bias. As the band-to-band intensity correlates with the lifetime of the minority charge carriers, the dark regions indicate defect-rich regions of short charge carrier lifetime in the solar cell. Some of these regions show strong defect-related luminescence [Figure 6.2(b)], but the ReBEL in these regions is rather weak [Figure 6.2(c)]. On the contrary, regions with strong ReBEL show low defect-related luminescence only. The cell exhibits breakdown sites upon reverse biasing. Different breakdown types, based on their voltage dependence, were detected. The regions of their appearance are indicated with colored rectangles in the Figure.

The different breakdown types have, as mentioned before, various voltage dependencies. In Figure 6.3, the ReBEL intensity is shown for various voltages. Breakdown type 1 shows almost linear voltage dependence. The diode breakdown starts at about -5 V . At -8 to -9 V , extended regions of breakdown sites start to emit ReBEL with exponential voltage dependence. This breakdown type 2 occurs at grain boundaries, which emit less intense D1 luminescence. At higher reverse bias, at about -12 V , breakdown type 3 appears which has exponential voltage dependence, too. This breakdown type can appear in regions with strong D1 luminescence and in regions where no D1 luminescence is detectable at all (cf. Figure 6.2).

A superposition of D1 luminescence and ReBEL at higher magnification of region 3 from Figure 6.2 reveals a well-established spatial separation of D1 luminescence and luminescence caused by breakdown type 3 (Figure 6.4). The D1 luminescence appears with a dendritic line character, whereas the breakdown luminescence appears with a point like character. In regions of strong D1-radiating defects, breakdown type 3 only and no type 1 or type 2 is observed.

For a more detailed investigation, small samples were cut out of regions where strong D1 luminescence is detected. Microscopic images at different magnifications can be seen in Figure 6.5. In each image is a highlighted detail, which is presented thereunder at higher magnification. An area of apparent coincidence of type 3 breakdowns and D1 emitting defects was selected [Figure 6.5(a)]. An about 10 times magnified picture shows a clear separation between forward and reverse bias emitting sites [Figure 6.5(b)]. A 100 times magnification shows two point like sources of reverse bias emitted light [Figure 6.5(c)]. Those two points are at a crystal defect, which definitely appears dark under forward biasing. The distance between defects emitting ReBEL and the grain boundary

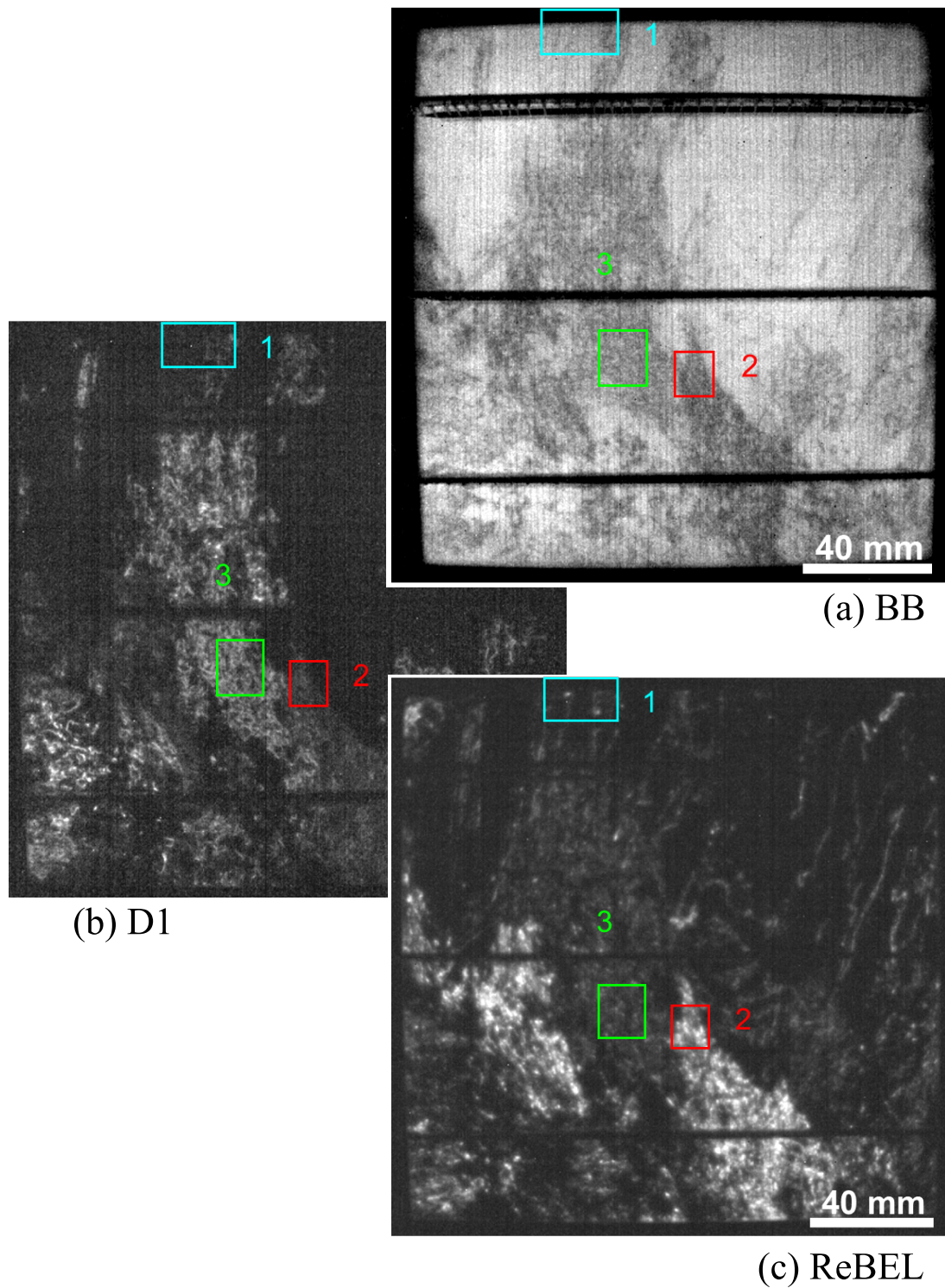


Figure 6.2.: Electroluminescence images of a solar cell. (a) Distribution of the band-to-band electroluminescence (forward bias), (b) distribution of the defect-related electroluminescence (forward bias), and (c) distribution of the reverse bias electroluminescence (ReBEL). The marked areas indicate the different breakdown types.

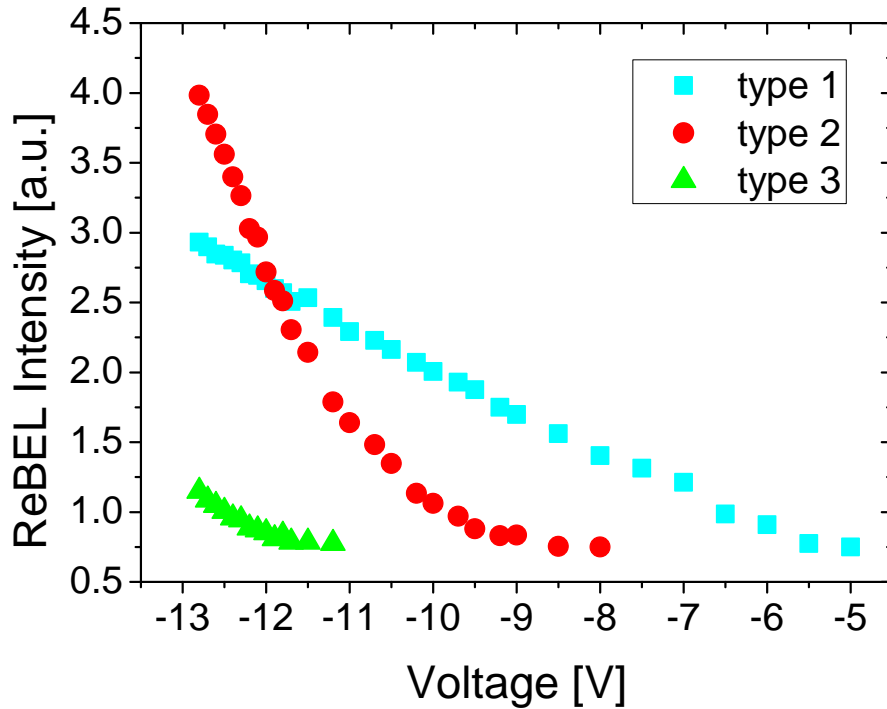


Figure 6.3.: ReBEL intensity versus applied voltage of different breakdown types, according to Figure 6.2.

was estimated to about $5 \mu\text{m}$.

To estimate the overall recombination activity of breakdown sites an EBIC investigation was conducted in co-work with Ch. Krause. Figure 6.6 shows a typical micrograph of an area with a grain boundary and a breakdown site. The EBIC micrograph is recorded at 30 keV and 100 pA. In the proximity of a dark appearing grain boundary, a point-like defect with dark contrast as well is seen (red arrow). From comparison of luminescence and EBIC investigations, this position is indicated as a breakdown site of type 3. According to the contrast value, both features seem to exhibit rather strong recombination activity. A shadow around the grain boundary indicates a $10 \mu\text{m}$ wide zone of enhanced recombination. The shadowed zone is a region, where charge carriers generated near the grain boundary recombine predominantly at the grain boundary instead of moving toward the surface $p-n$ junction and contributing to the EBIC. The width of the shadowed zone is essentially determined by the diffusion length of the minority charge carriers.

This demonstrates, that sites of type 3 breakdown are spatially separated from defects emitting D1 luminescence, not as supposed by Bothe et al. [BRH⁺09]. Basically, two

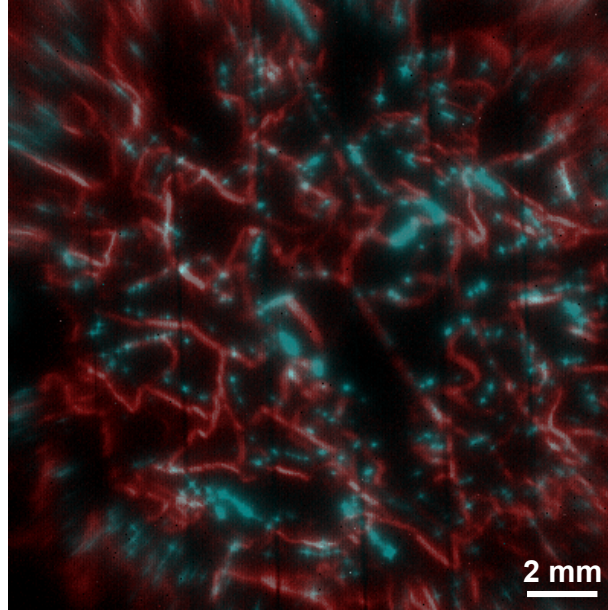
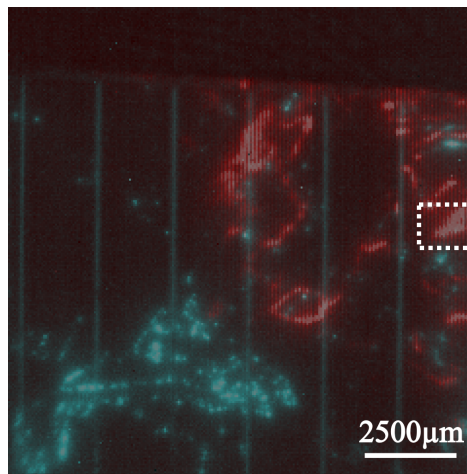


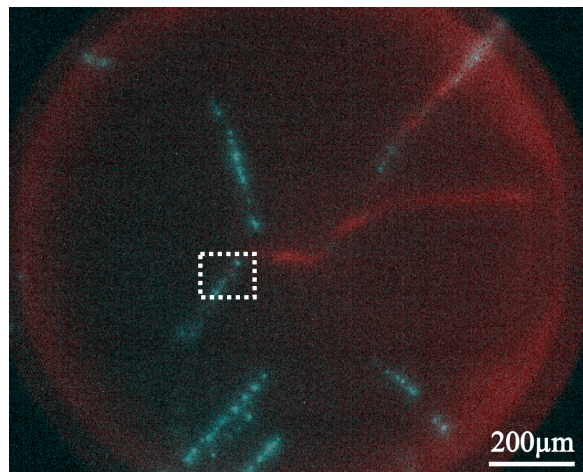
Figure 6.4.: Superposition of defect-related luminescence (red) and ReBEL (cyan) signal in region 3 of Figure 6.2. The resolution is about $50 \mu\text{m}$.

mechanisms may explain such anti-correlation: (*i*) defects emitting D1 luminescence suppress the formation of the specific defect that causes breakdown and (*ii*) defects causing breakdown lead to a reduced D1 luminescence. The appearance of D1 luminescence indicates the presence of dislocations/grain boundaries. One can assume that spots with D1 luminescence are characterized by a high density of dislocations. Since dislocations represent gettering sites for impurities, a lower level of dissolved impurities and a smaller size of impurity precipitates are expected in regions of high dislocation density. Assuming that precipitates are involved in breakdown, this may explain the first mechanism. As to the second mechanism, breakdown sites have been shown by EBIC to be regions of high (non-radiative) recombination. Accordingly, the concentration of minority charge carriers is locally reduced at/near breakdown sites, leading locally to a smaller rate of radiative recombination. In addition, the defect states responsible for D1 luminescence may be affected by impurities as well. Unfortunately, based on the results presently available the acting mechanism cannot be identified. Further investigations are necessary to unravel the origin of the observed anti-correlation between D1 luminescence and breakdown of type 3.

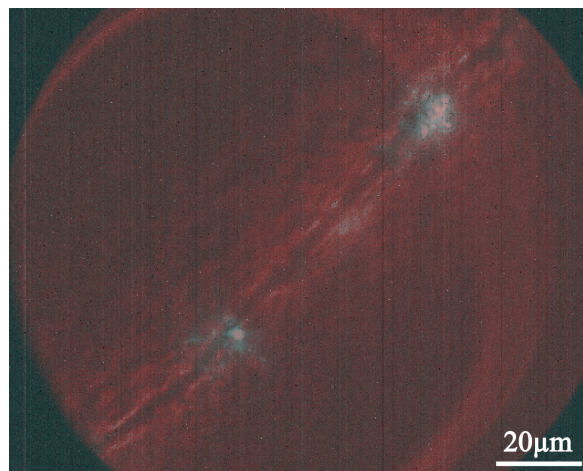
Compared to early reports [New55, CM56] no light emission in the visible range (400 - 800 nm) can be observed (cf. Figure 6.1). ReBEL in the near-infrared part of the electromagnetic spectrum has not been reported up to now. Furthermore, a recent report show



(a)



(b)



(c)

Figure 6.5.: Superposition of defect-related luminescence (red) and ReBEL (cyan) signal at different magnifications. The rectangle in (a) marks the area which is given in (b) and the rectangle therein represents the area given in (c).

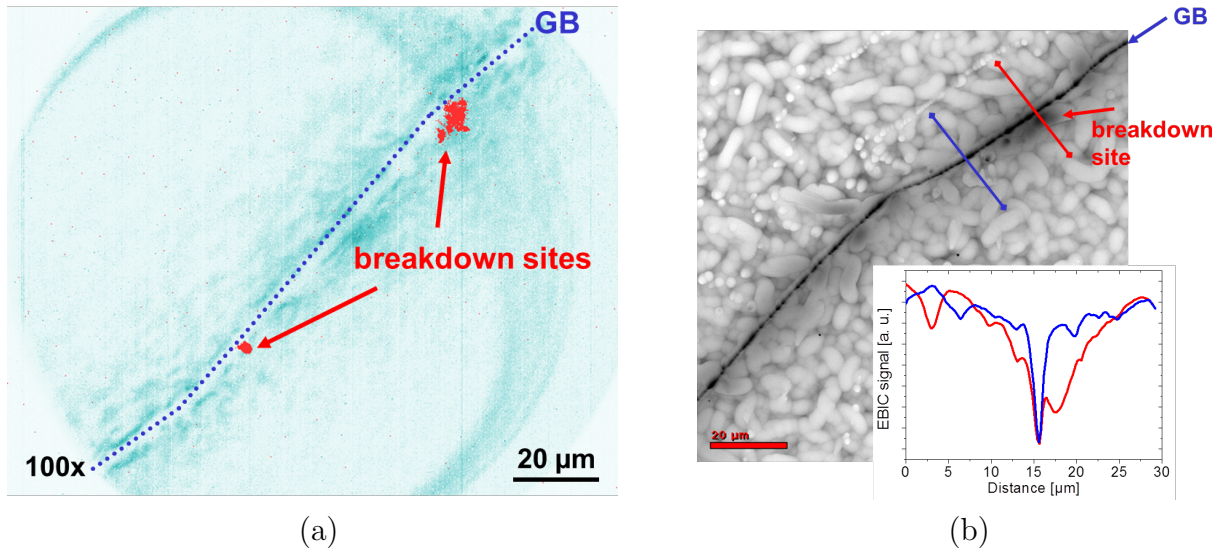


Figure 6.6.: Comparison of high resolution luminescence and EBIC graphs. (a) Superposition of defect-related luminescence (cyan) and ReBEL (red) signal [cf. Figure 6.5 (c)]. (b) EBIC micrograph of a typical breakdown region at room temperature. In the proximity of a dark grain boundary a point-like dark contrast is seen (red marked). It spatially correlates with the appearance of a type 3 breakdown site. Note that the maggot-like structures are caused by the surface roughness resulting from the cell process. The EBIC micrograph is recorded at 30 keV and 100 pA. The inset shows the extracted profiles at the respective marked regions.

as well ReBEL spectra in the visible range [KKG⁺09], which could not be confirmed here.

The classification of the breakdown types 1 to 3 (cf. Figure 6.3) is very similar to recent works [KKG⁺09, BRH⁺09, BBB⁺11].

6.2. EL on silicon thin film on glass cells in forward and reverse bias mode

Due to the development of imaging techniques for bulk silicon, the idea is to investigate silicon thin films with the same methods. This means in this case observing the band-to-band luminescence, defect-related luminescence and reverse bias electroluminescence as well. If the same techniques would work on thin film material, one had only to apply the “old” technique to the “new” thin film solar cells. Thus, one has quite easy monitoring techniques for polycrystalline silicon thin film on glass in cell production.

6.2.1. Samples and measurements

Two different modules of polycrystalline silicon on glass were investigated by electroluminescence imaging. The cells are prepared as described in Section 1.4. On each module, nine solar cells with different finger pitch of the top contact are prepared (cf. Figure 6.7(a)). A schematic of such a cell is depicted in Figure 6.7(b). The difference between the modules is the barrier layer between glass substrate and silicon. Module 1 has SiO_x as a barrier, whereas module 2 has a stack of three layers: SiO_x - SiN_x - SiO_x . None of the modules is intentionally textured, but this is irrelevant since the excitation is electrical and not optical. Each cell has a size of $10 \times 6 \text{ mm}^2$, the grid distances are $200 \mu\text{m}$, $400 \mu\text{m}$, and $666 \mu\text{m}$. All measurements were obtained at room temperature.

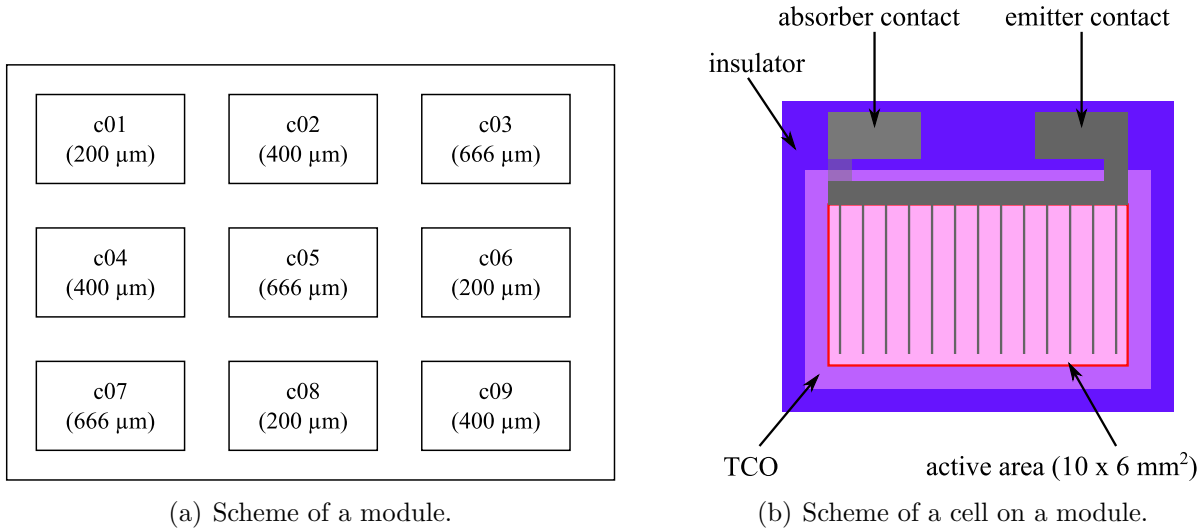
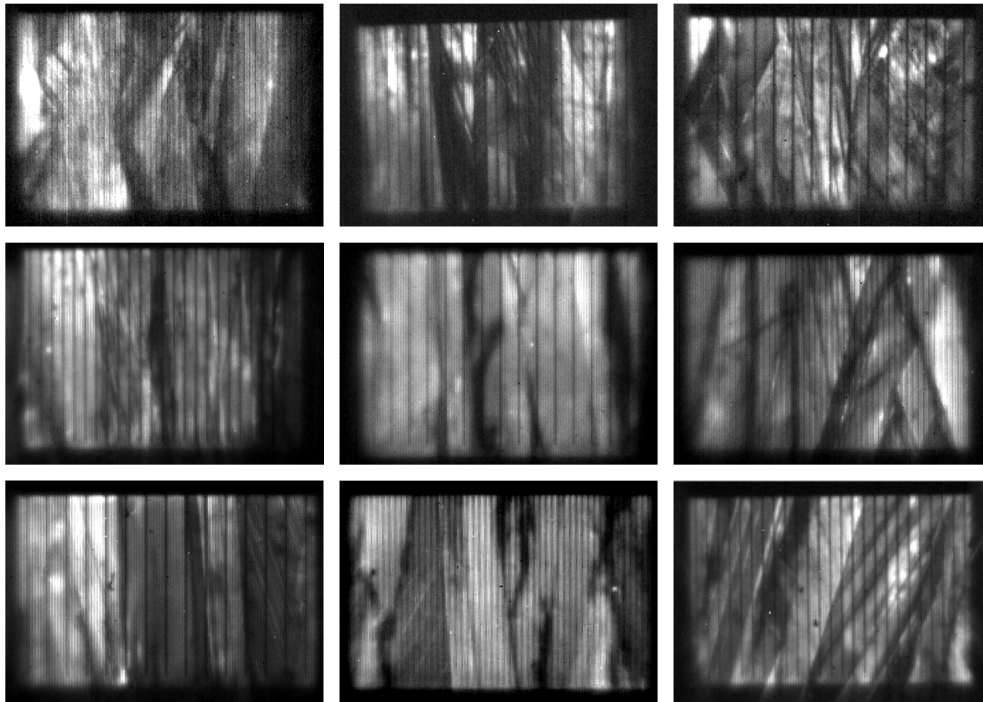


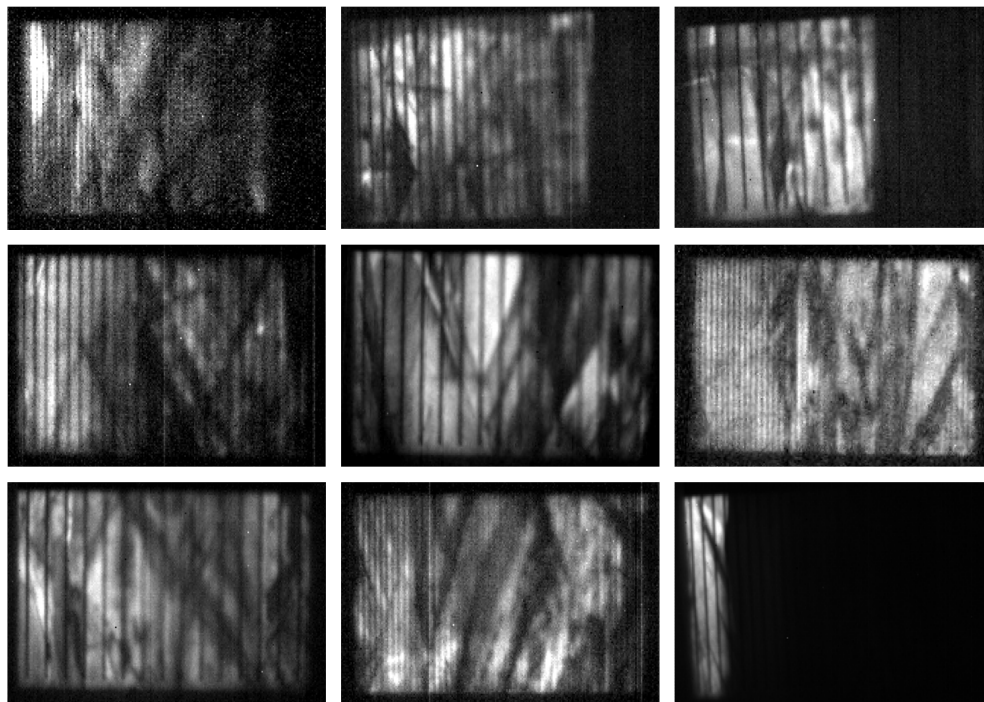
Figure 6.7.: Schematic of (a) a thin film module with cell labels and front contact grid distance in brackets, and (b) a cell on a module.

6.2.2. Results and discussion

As a first investigation, the band-to-band electroluminescence of each cell was recorded. The cells are excited with constant current, which was set to 80 mA; the voltage varied slightly from cell to cell, but was in the range of 1 V. In Figure 6.8, the images of the cells are compared for each module, worth to note here is, that the scales of the images are not comparable. Apparent from the images is that on module 2 (cf. Figure 6.8(b)) several cells (esp. c02, c03, and c09) partially shunt.

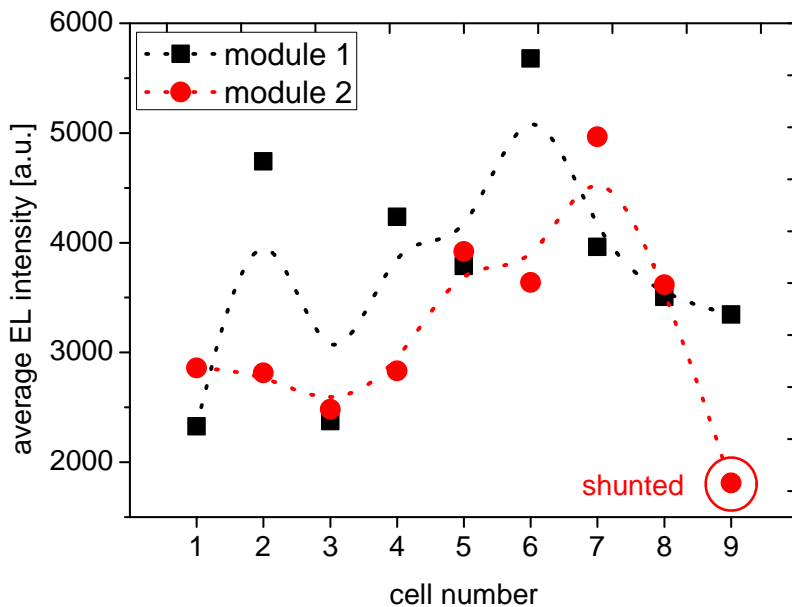


(a) BB electroluminescence images of module 1.

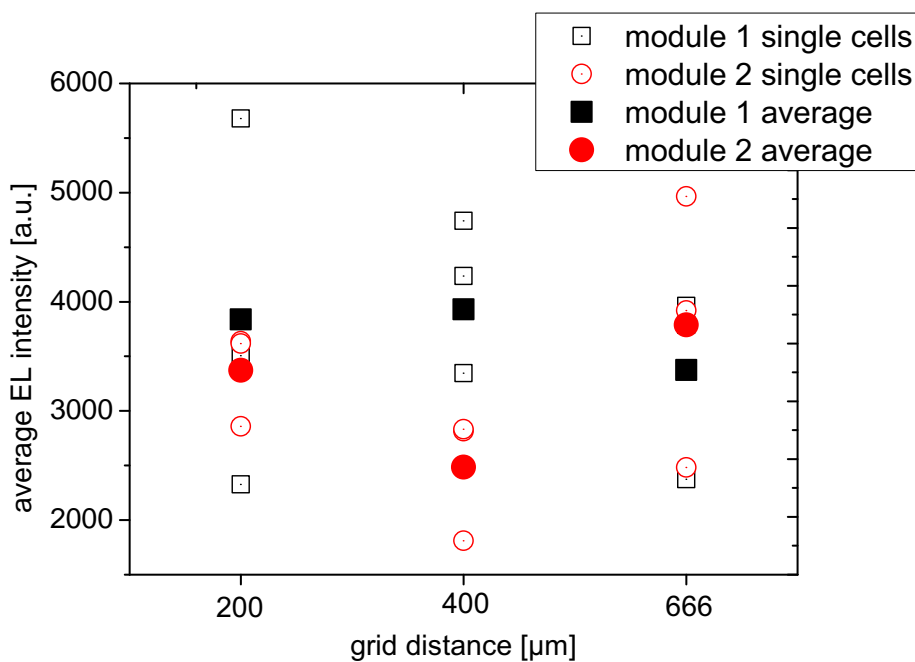


(b) BB electroluminescence images of module 2.

Figure 6.8.: Room temperature band-to-band electroluminescence images of (a) module 1 and (b) module 2, respectively. The scales of the images are different. The corresponding labels and grid distances for the cells are given in Figure 6.7(a).

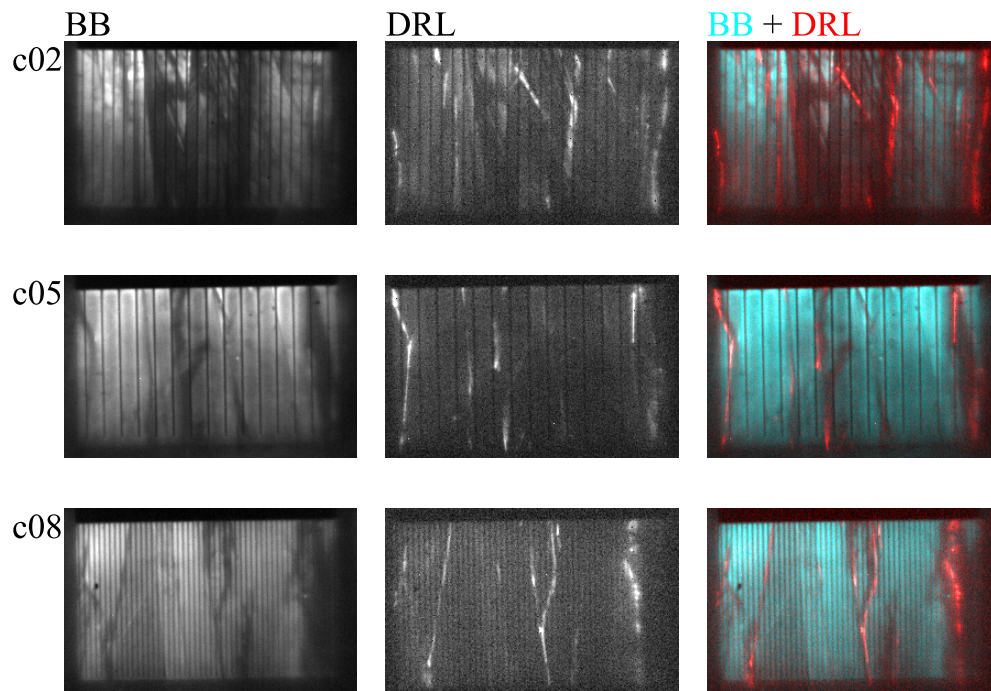


(a) Average electroluminescence intensity of each cell.

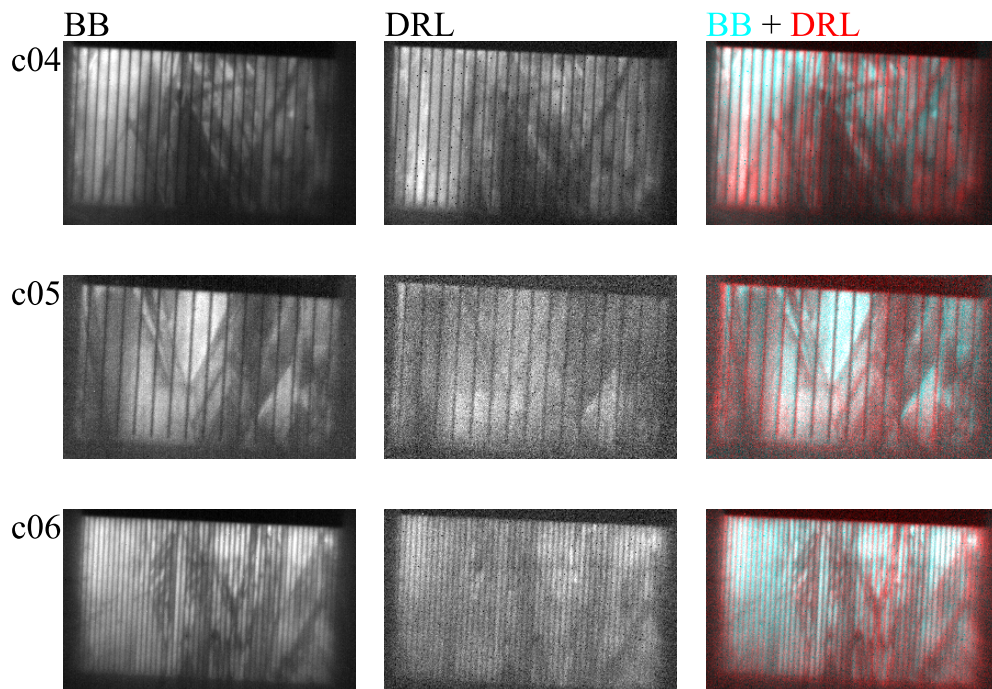


(b) Electroluminescence intensity as a function of grid distance.

Figure 6.9.: Average electroluminescence intensity of each cell (a), and electroluminescence intensity as a function of grid distance (b).



(a) Luminescence images of module 1.



(b) Luminescence images of module 2.

Figure 6.10.: Room temperature band-to-band (BB) and defect-related (DRL) luminescence images of selected cells of (a) module 1 and (b) module 2, respectively. The right-sided images are superpositions of BB (cyan) and DRL (red) images color coded. The scales of the images are incomparable. The cell labels are given, corresponding grid distances for the cells can be found in Figure 6.7(a).

The average band-to-band electroluminescence intensity of each cell is shown in the graph in Figure 6.9(a). The black squares and red circles indicate the cells on module 1 and module 2, respectively; the dotted lines guide the readers eyes only. The overall BB electroluminescence intensity on module 1 is slightly higher than in module 2. A reason for this difference is whether the difference in the interlayer or the silicon layer quality in general. Because both modules have many regions with reduced band-to-band electroluminescence intensity, which means defective areas, the interlayer seems to play a major role on the average electroluminescence intensity. This implies that the single SiO_x layer is more suitable for the cell structure than the stack of $\text{SiO}_x - \text{SiN}_x - \text{SiO}_x$. On the contrary, the stack is more favorable during cell process, because the silicon absorber layer adheres better than on the single SiO_x layer.

Another cause for the reduced average BB electroluminescence intensity is of course the grid distance. The more fingers are placed on a cell the higher is the “shadowing effect”, in other words, the grid blocks partially the radiated light, and thus, the camera detects a lower signal.

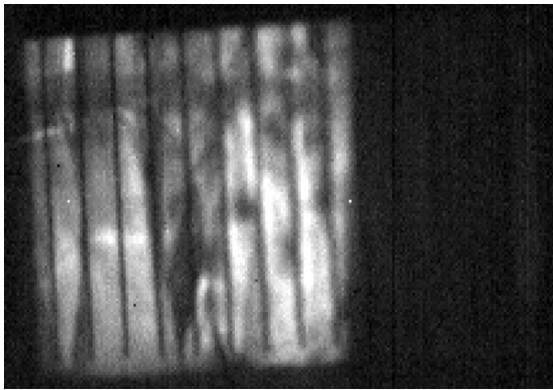
Additionally to the band-to-band luminescence images defect-related luminescence has been recorded. Here the same excitation conditions were used as during recording of the band-to-band luminescence images, but the acquisition time was drastically enhanced. This is necessary because of the low intensity of the defect-related luminescence at room temperature.

In Figure 6.10, one can see selected cells of each module. Cells of module 1 are depicted in Figure 6.10(a), whereas cells of module 2 are shown in Figure 6.10(b). On the left side in both of the Figures, the band-to-band luminescence image is shown, in the middle the defect-related luminescence and on the right side a superposition of band-to-band and defect-related luminescence images. In the superimposed images, cyan stands for the band-to-band luminescence and red for the defect-related luminescence.

An eye-catching result is the dominant defect-related luminescence in module 2. A typical defect-related luminescence image, compared to bulk material, should look much more like the defect-related luminescence images in module 1. The origin of this spatially extended defect-related luminescence in module 2 could be the triple layer. It might be possible that this structure induces plenty lattice mismatches and consequently dislocations in the silicon layer. These dislocations would cause the enhanced defect-related luminescence.

Besides the forward bias electroluminescence, the reverse bias mode was conducted as well. Surprisingly reverse bias electroluminescence was detected very rarely, particularly it

was found on one silicon thin film cell at all. In Figure 6.11, the band-to-band and reverse bias electroluminescence images of this cell are shown. The breakdown sites appear at the electrical contacts and the cell edges only. There seems to be no hint that breakdown sites and dislocation-rich regions correspond. Hence, one can suppose that breakdown type 1 is observed here.



(a) Band-to-band electroluminescence image (forward bias).



(b) Reverse bias electroluminescence image.

Figure 6.11.: Room temperature band-to-band (BB) electroluminescence image of a selected cells (a) and the corresponding reverse bias electroluminescence image (b).

6.3. Summary

In bulk multicrystalline silicon solar cells, three breakdown types of different voltage dependence could be found. Type 1 shows an almost linear breakdown behavior starting at -5 V . This type is very rarely present at solar cells. Breakdown type 2 starts at -8 V to -9 V bias. At these sites, defects emitting low D1 radiation only and they are located within grain boundaries. At about -12 V breakdown type 3 emits infrared radiation only; no radiation in the visible part of light could be detected.

It has been demonstrated that defects emitting ReBEL of type 3 are different to defects emitting D1 luminescence. In regions of defects emitting rather strong D1 luminescence, breakdown type 3 is detected only. Microscopic luminescence investigations showed a distinct spatial separation between defects emitting strong defect-related luminescence (D1) and defects emitting ReBEL. Microscopic electroluminescence and EBIC investigations seem to indicate that these breakdown sites heavily deplete the excess charge carriers.

Therefore, these charge carriers cannot recombine radiative at the neighboring extended defects. This would explain the missing D1 luminescence at breakdown sites.

Silicon thin film solar cells are investigable by electroluminescence in the same way as bulk mc-Si solar cells. Different barrier layers induce different lattice mismatches, which result in an enhanced or reduced defect structure and subsequently defect-related luminescence.

Reverse bias electroluminescence is detectable on thin film solar cells as well, but very rarely only. It is supposed that on thin film cells breakdown type 1 is observed only.

7. Comparative analysis of PL and FTIR

In this chapter, combined investigations of photoluminescence and Fourier-transform infrared spectroscopy (FTIR) are described. These combined investigations were motivated by the idea of finding a correlation between the oxygen content and the D1 or oxygen-related luminescence. Due to higher oxygen content at the bottom of a block, an agglomeration of oxygen-related luminescence is expected. Furthermore, a correlation between carbon content and the distribution of luminescence lines was expected, but could not be found. Nevertheless, a possible correlation between nitrogen content and the appearance of D3/D4 luminescence was observed. The first section deals with results investigated by FTIR, whereas the second section shows the photoluminescence measurements. In the third section, the photoluminescence and FTIR results are compared and discussed. The last section gives a short summary of the results.

7.1. FTIR

In this section the results of the Fourier-transform infrared absorption measurements of two different multicrystalline silicon blocks are presented. The diagrams of the impurity concentrations of substitutional carbon (C_s), interstitial oxygen (O_i) and the nitrogen-nitrogen bonding (NN) are shown for the two blocks. The concentration of the different impurities in the blocks is shown in Figure 7.1.

Substitutional carbon is given in black, for block 1 in solid squares, for block 2 in dot-centered squares. Block 1 shows an uncommon behavior in the C_s distribution. There is a “jump” in the middle of the block. In the bottom part, the concentration raises from $0.70 \times 10^{18} \text{ cm}^{-3}$ to $1.28 \times 10^{18} \text{ cm}^{-3}$. In the top part, the concentration raises from $0.73 \times 10^{18} \text{ cm}^{-3}$ to $1.51 \times 10^{18} \text{ cm}^{-3}$. In block 2 the C_s increases from $0.48 \times 10^{18} \text{ cm}^{-3}$ to $1.02 \times 10^{18} \text{ cm}^{-3}$ to the middle of the block and decreases then to $0.77 \times 10^{18} \text{ cm}^{-3}$ with increasing block height, which is also an uncommon behavior for the C_s distribution, since C_s content should increase with increasing block height.

7. Comparative analysis of PL and FTIR

For interstitial oxygen, red circles are used, block 1 has solid circles, and whereas dot centered circles are used for block 2. The O_i in block 1 decreases from $6.13 \times 10^{17} \text{ cm}^{-3}$ to $0.50 \times 10^{17} \text{ cm}^{-3}$ with increasing block height. In block 2 O_i decreases from $4.82 \times 10^{17} \text{ cm}^{-3}$ to $0.82 \times 10^{17} \text{ cm}^{-3}$ with increasing block height. Both concentrations show a common behavior, except the data point at the bottom of block 2. There the O_i concentration is a bit lower than at the next data point.

Green triangles represent the nitrogen, solid triangles for block 1 and dot centered for block 2. The nitrogen concentration in block 1 increases from $2.05 \times 10^{15} \text{ cm}^{-3}$ to $5.78 \times 10^{15} \text{ cm}^{-3}$ to a block height of 67 mm and decreases then to $0.82 \times 10^{15} \text{ cm}^{-3}$ to the block lid. In block 2, the NN concentration raises $3.74 \times 10^{15} \text{ cm}^{-3}$ to $18.2 \times 10^{15} \text{ cm}^{-3}$ to a block height of 82 mm and drops down to $5.83 \times 10^{15} \text{ cm}^{-3}$ afterward.

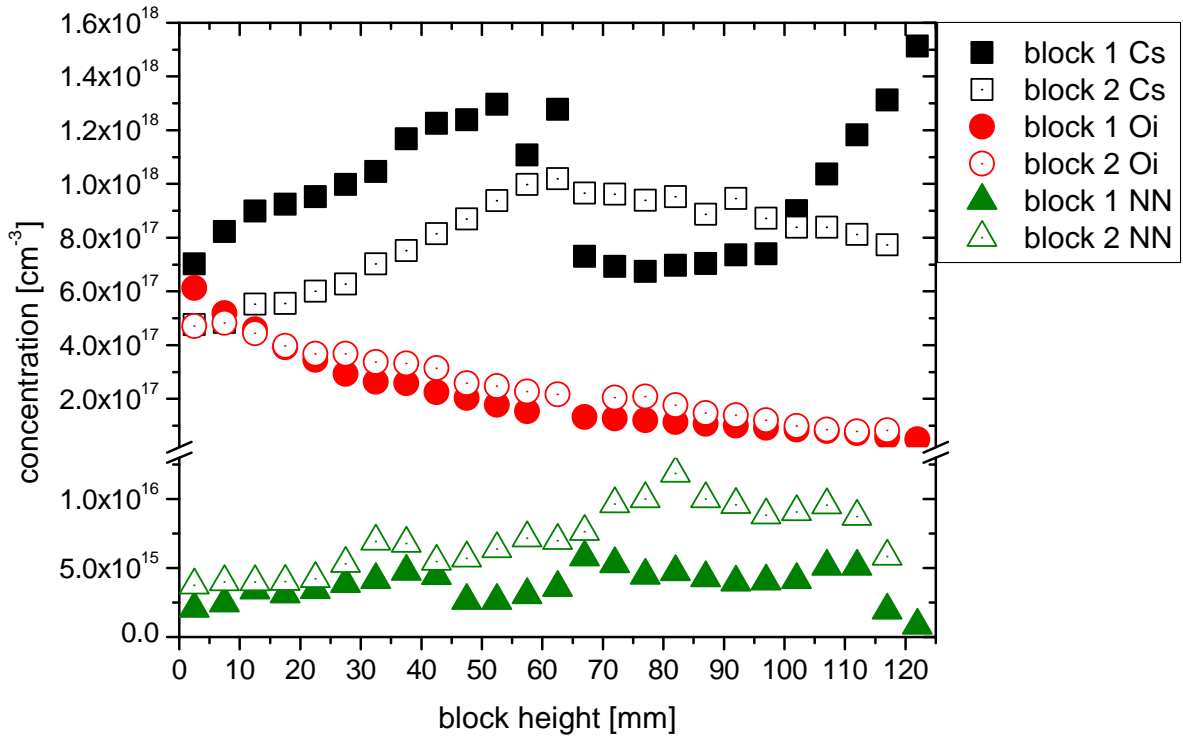


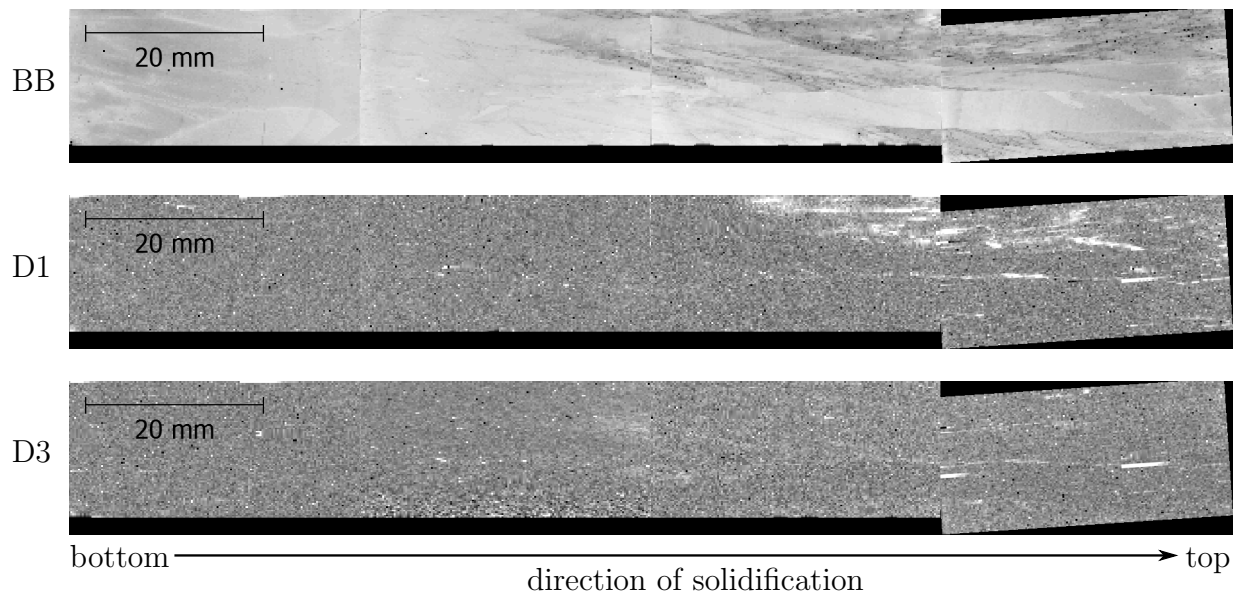
Figure 7.1.: Concentration distribution of substitutional carbon (C_s), interstitial oxygen (O_i) and nitrogen-nitrogen bonding (NN) of the two blocks. Solid symbols for block 1 and dot centered symbols for block 2.

7.2. PL measurements

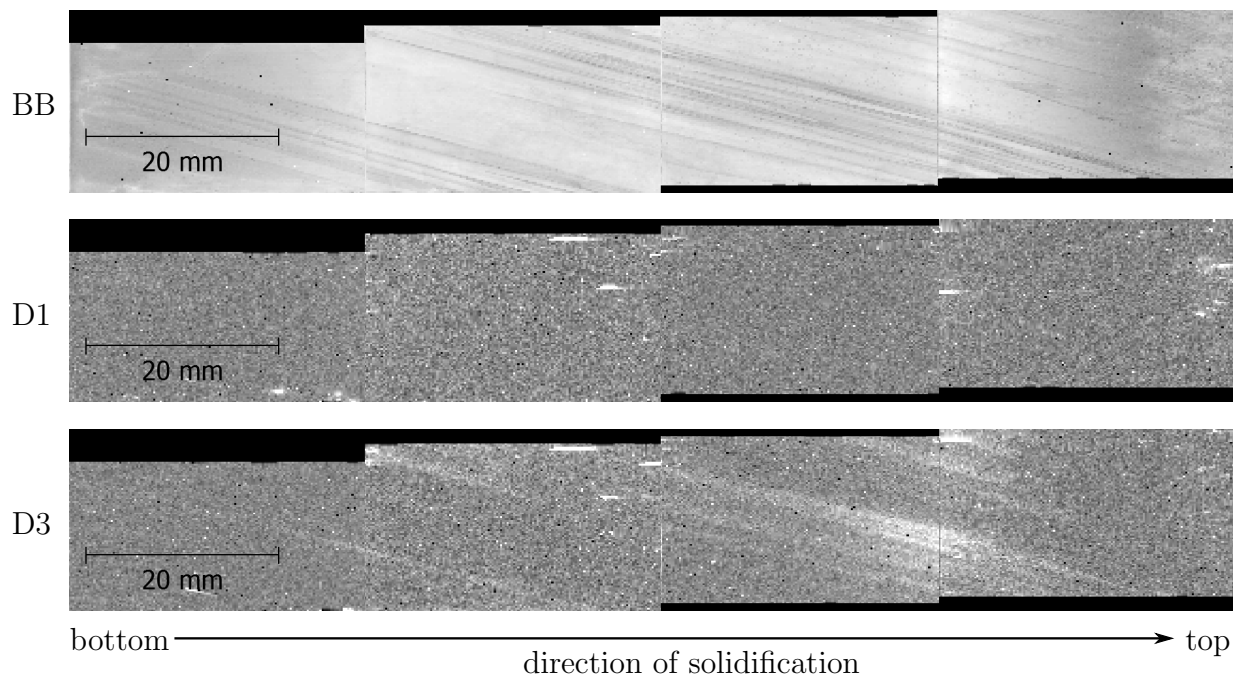
Here the results of the photoluminescence measurements of vertical slabs of the two blocks are shown. The samples (about 125 mm in length/height) had to be cut into smaller pieces ($\frac{1}{4}$ of sample length), to fit into the cryostat, since room temperature measurements yielded only band-to-band luminescence. The four single maps are composed to one whole map. All maps shown here are recorded at 80 K. For both of the two blocks the following photoluminescence maps are created: (i) on top the band-to-band luminescence (1125 nm); (ii) in the middle “D1” luminescence (1530 nm) which should also include shoulders of a possible oxygen peak (center located at 1600 nm); (iii) at bottom “D3” like luminescence (1333 nm) which also shows part of the real D3 peak. The PL intensity of the BB map has a logarithmic gray-scale, whereas both the D1 and D3 maps have a linear gray-scale for better illustration.

In Figure 7.2(a), the three maps of block 1 are depicted. In the BB map, the most lower part of the slab (first 20 mm from left) shows rather low PL intensity in the grains, but gettering zones at grain boundaries. The reason is the high impurity content at the bottom of the block material. Mainly metallic impurities cause such behavior. With increasing block height, the PL intensity in the clean grains seems to rise. Starting in the middle of the block, many dark areas are visible; these are defect-rich regions. These are grains with high dislocation density, grain boundaries and precipitates for example. The upper part of the block (right in the picture) has a reduced PL intensity in the grains and gettering effects seem to take place, too. The D1 map shows high luminescence intensity in the defect-rich regions only. Compared to the BB map only at the supposed grains with high dislocation density, grain boundaries and precipitates. The D3 map shows an increased signal at a few grain boundaries only.

The three maps of the second block are shown in Figure 7.2(b). Here the BB map shows in bottom and top region a similar behavior like in the first block. However, the lower intensity in the bottom region is not as spatially extended as in block 1. In the middle region of the block, no highly dislocated grains are detectable; there seem to be more parallel grain boundaries, which results in a decrease of PL intensity. In the top region, gettering zones are clearly visible. The D1 map shows only a few spots with higher intensity, mainly in the top region. In the D3 map, the dark grain boundaries of the BB map show increased PL intensity.



(a) Photoluminescence maps of block 1.



(b) Photoluminescence maps of block 2.

Figure 7.2.: Photoluminescence maps at 80 K for (a) block 1 and (b) block 2. In both Figures the upper image shows the band-to-band map (1125 nm), the middle image the D1 luminescence map (1530 nm), and the lower image shows the luminescence map near the D3 line (1333 nm).

7.3. Comparison of FTIR and PL

In this section, the results of the photoluminescence measurements on the FTIR samples are compared with the FTIR data. I approached the question whether there are correlations between various luminescence signals and non-doping impurities in multicrystalline ingots. The distribution of the band-to-band luminescence can be correlated with the interstitial oxygen distribution. Moreover, it is found that there might be a connection between radiating defects and a certain absorption band of the FTIR spectrum.

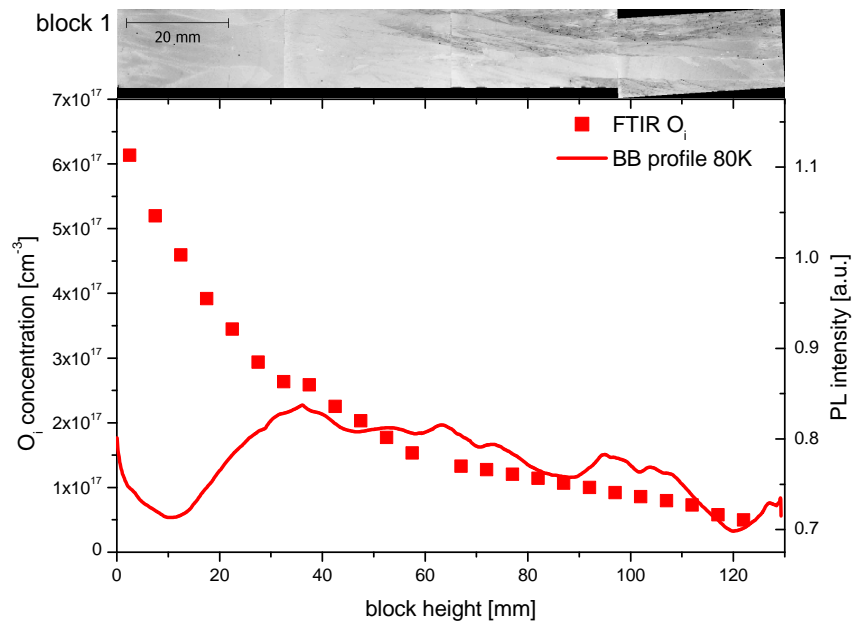
The luminescence profiles are averaged over a region of about 5 mm to get comparable with the aperture of the FTIR spectrograph.

Interstitial oxygen

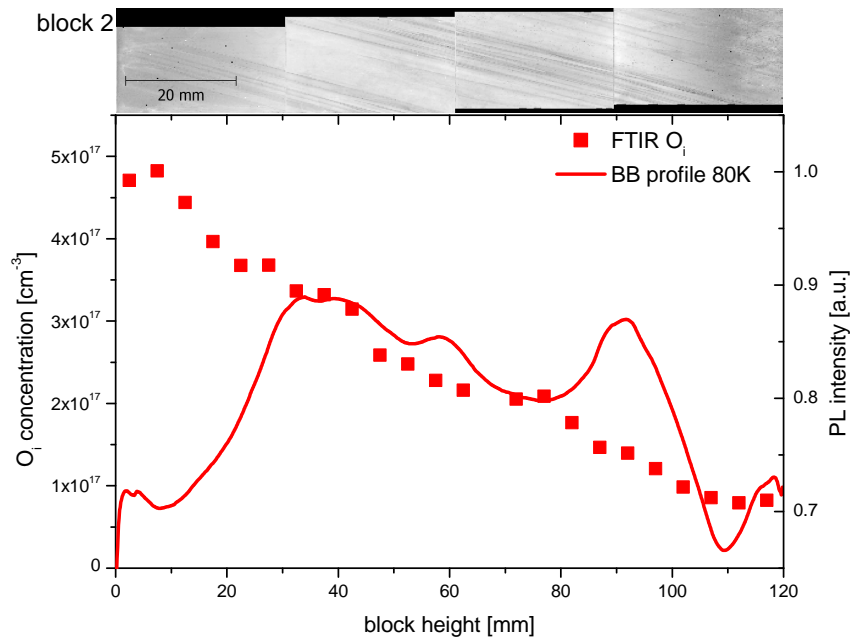
The band-to-band luminescence intensity of the slabs is in the lower quarter increasing with block height. Shortly above, the band-to-band luminescence intensity starts to drop down (cf. Figure 7.3). The low intensity at the bottom can be explained by a high concentration of impurity atoms at the bottom. In this region, the silicon melt has the longest contact to the crucible walls during crystallization process, thus a high amount of impurity atoms can diffuse from the crucible and/or coating into the melt. Impurity atoms in the bottom region are metals and oxygen in the main. The FTIR data show that the oxygen content in the bottom is rather high and decreases with increasing block height from beginning. Besides the impurities dislocation density is relevant as well, as Möller et al. [MFL⁺02] suggest. They say that the dislocation density is quite high at the bottom of a silicon block. Thus, oxygen precipitation should be most likely in the bottom part where the concentration of both, dislocations and oxygen, is higher. Since, the band-to-band luminescence is an indicator for the lifetime the reduced intensity at the bottom region can also be explained with the high oxygen content in this region. Rossberg et al. [RNI⁺05] remark that at the bottom oxygen correlated recombination defects dominate. They found that in the sidewall region of a block an increase of interstitial oxygen concentration correlates with a steep decrease in lifetime. They concluded that oxygen-related defects are reasonable for low lifetime. This would explain the drop in band-to-band luminescence intensity in the bottom region of the blocks.

However, much more interesting is the curvature of the BB profile in the following region, means after the first quarter. Here the band-to-band luminescence intensity starts at a maximum and decreases with increasing block height in almost the same manner as the

7. Comparative analysis of PL and FTIR



(a) Band-to-band luminescence and oxygen profiles of block 1.



(b) Band-to-band luminescence and oxygen profiles of block 2.

Figure 7.3.: Profile of BB luminescence at 80 K with respective PL map, and distribution of interstitial oxygen for (a) block 1 and (b) block 2, respectively. Solidification starts at 0 mm. Larger photoluminescence maps are shown in Figure 7.2.

oxygen content does (cf. Figure 7.3). This is in contrast to the before mentioned connection between interstitial oxygen and band-to-band luminescence intensity. It might be that the increasing carbon concentration is the decisive factor, but the distribution of substitutional carbon (Figure 7.1) is not connected in any way with the band-to-band luminescence profile in both of the blocks.

The BB profile in block 1 is most probably influenced by the defect density at all. These defects are especially grain boundaries, dislocation-rich grains and precipitates of various types. Obviously, the defect density raises with increasing block height, which is visible in the D1 map (Figure 7.2(a)) as well. In the top half of block 1, the D1 luminescence is clearly recognizable and its density is strikingly increased.

In block 2 the BB profiles decreases with increasing height as well as in block 1, except the “spike” at 90 mm height, but here is nearly no sight of D1 luminescence. This “spike” originates from measurement problems or more specifically this region is the edge of the sample. During sample preparation, the edges are influenced stronger by the etchant than the plane surfaces. Nevertheless, here another defect seems to play a major role for reduction of band-to-band luminescence. At these almost parallel grain boundaries, D3/D4 luminescence is detectable only, which is also a remarkable result. As known defects, insignificant of which type, reduce the charge carrier lifetime and hence the band-to-band luminescence intensity. By comparing the data for substitutional carbon and the BB profile, carbon seems not to play any role for the band-to-band luminescence in this block, though.

In Figure 7.4 typical spectra for defective regions in each block are given. The black graph depicts a grain boundary in block 1, whereas the red graph stands for one of these parallel grain boundaries in block 2. As the gentle reader might see, in block 1 the D1 line is dominant, while in block 2 the D3/D4 lines prevail (see also Figure 7.2).

Nitrogen and D3/D4 line

Comparison of the D3 luminescence profile with the distribution of nitrogen concentration of the FTIR measurements, an unexpected correlation between the behaviors of the curves is apparent. The photoluminescence spectra at various positions of block 2 show that D3 and D4 luminescence appear pairwise on the grain boundaries. A sample spectrum is shown in Figure 7.4.

The distribution of the D3 luminescence is similar to that of the nitrogen content over the block height. The profiles do not fit one-to-one because the luminescence maps are created at smaller samples pieces than the FTIR measurements. There is a loss due to

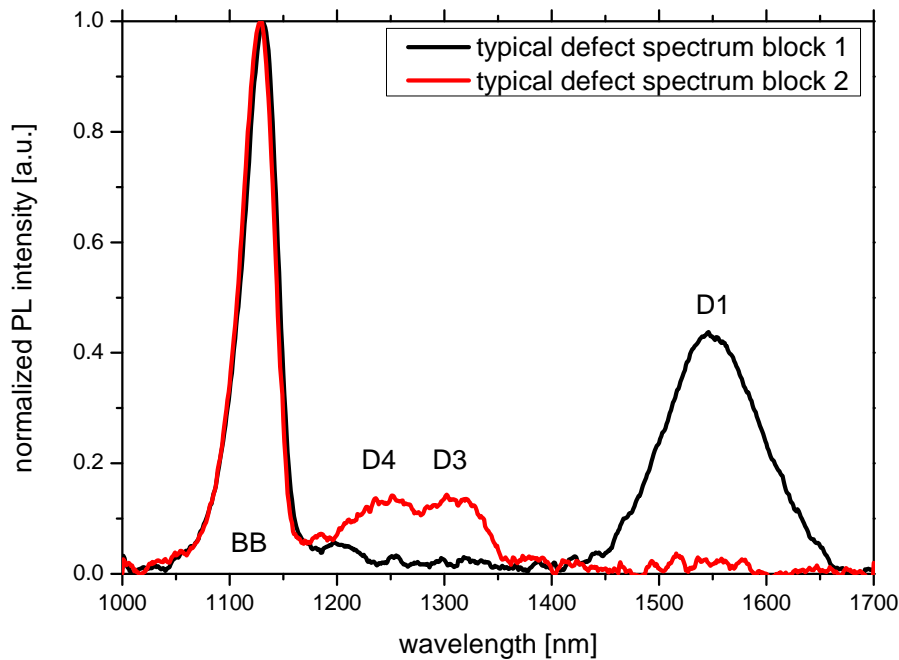
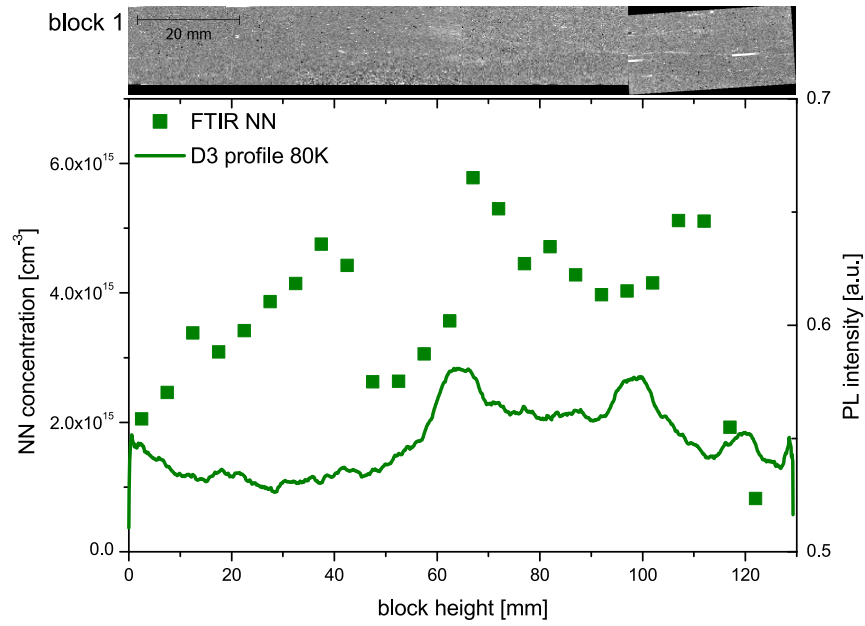


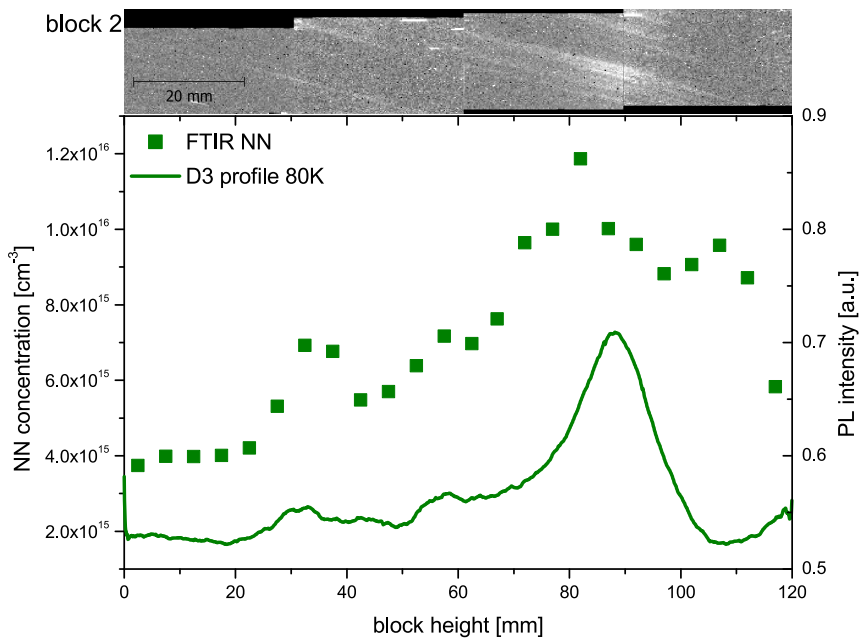
Figure 7.4.: Typical spectra at defective regions in block 1 (black) and block 2 (red). The spectra are recorded at 80 K and are normalized to the band-to-band transition. Important peaks are declared.

sawing and passing over sample edges during scanning because of occurring measurement artifacts. Nevertheless, the overall tendency is still observable.

In the lower part of block 1 (Figure 7.5(a)), a discrepancy between nitrogen distribution and D3 profile is noticeable. The nitrogen content rises whereas the profile of D3 luminescence remains almost constant or lower slightly. This could be caused by Si_3N_4 filaments or precipitates containing nitrogen, which are not observable with luminescence techniques. Nevertheless, from 45 mm block height onwards the profiles of D3 luminescence and nitrogen concentration are similar. At about 45 mm, the nitrogen concentration starts to increase as well as the D3 luminescence intensity, peaking at about 65 mm. Then the profiles decrease lightly and another peak appears at 90 mm to 110 mm. Thereafter a drop in both profiles is observable.



(a) D3 luminescence and nitrogen profiles of block 1.



(b) D3 luminescence and nitrogen profiles of block 2.

Figure 7.5.: Profile of D3 luminescence at 80 K with respective PL map, and distribution of nitrogen for (a) block 1 and (b) block 2, respectively. Solidification starts at 0 mm. Larger photoluminescence maps are shown in Figure 7.2.

In block 2 (Figure 7.5(b)), the correlation between the profiles of D3 luminescence and nitrogen concentration is much more obviously. The nitrogen concentration and D3 luminescence profile increase until a maximum in the upper half is reached and dropped down subsequently. At a block height of about 30 mm, a local maximum of both curves is visible. In the upper part of the block (100 mm to 120 mm) a large amount of precipitates, especially SiC clusters and Si₃N₄ filaments, are present. Hence, in this region the D3 luminescence as well as the BB luminescence has a steep decrease in intensity, but the FTIR results show meanwhile an increased nitrogen concentration.

Binetti et al. [BSD⁺02] studied the effect of nitrogen on the optical properties of dislocations in nitrogen-doped Czochralski and nitrogen-doped float zone silicon. They introduced the dislocations by plastic deformation at 650 °C. They concluded that nitrogen enhances the oxygen-dislocation interaction, and thus the oxygen precipitation process. Moreover, they found a red shift of about 9 meV of the D3 and D4 bands in the nitrogen-doped samples. The latter case could not be observed in this study. The D3/D4 bands remain at the same energies/wavelengths as found in the literature, independent of the experimental conditions. The former case remains an open question, because they observed peaks in the range of 0.83 eV besides the D2 and D3/D4 luminescence bands. In this work, D3/D4 and D1 or the oxygen-related luminescence line could not be observed at the same sample positions.

7.4. Summary

It is found that comparative investigations of Fourier-transform infrared spectroscopy and photoluminescence spectroscopy on mc-Si block material show surprising results. At first there seems to be a correlation of the distributions of interstitial oxygen and the band-to-band luminescence profiles. With increasing block height, both the oxygen content and the band-to-band luminescence, and thus the effective charge carrier lifetime, decrease. One exception on this point is the very bottom of the block, because there the impurity density is very high and thus the lifetime is reduced vastly. Another idea at the beginning of the observations was to find a correlation between the oxygen content and the D1 or oxygen-related luminescence, but this could not be approved. Additionally, a correlation between D3/D4 luminescence profile and nitrogen distribution in the blocks was observed. In contrast to the work of Binetti et al. [BSD⁺02], no connection between oxygen/nitrogen content and defect-related luminescence bands could be found.

8. Growth process of microcrystalline silicon

Hydrogenated microcrystalline silicon ($\mu\text{c-Si:H}$) is one of the most promising absorber materials for thin film silicon photovoltaics. Compared to pure amorphous silicon (a-Si:H), it offers several advantages. It shows lower affinity for light-induced degradation than a-Si:H, its band gap energy is lower than that of a-Si:H, and when used as emitter for tandem cells it allows higher efficiencies [MSD⁺06]. The advantages of using $\mu\text{c-Si:H}$ for thin film cells have been experimentally confirmed by other research groups as well (e.g. [RRR⁺03, SHTDB10]).

Besides the technological benefits of using $\mu\text{c-Si:H}$, it also presents an interesting object for material research. Here, two topics are very interesting. First, $\mu\text{c-Si:H}$ is much more complex than pure a-Si:H or pure c-Si. It is a mixture of nanocrystalline and amorphous silicon, whereas the grains can appear isolated within the matrix as well as agglomerated in columnar structures. A high density of twin boundaries and stacking faults is typical for these columns. They reach sizes of few hundred nanometers and are separated from each other by regions of a-Si:H or voids [Hou98, VFC⁺00]. But the size of the grains in the columns is still in a range of 10 - 30 nm. However, the exact mechanism of growth of $\mu\text{c-Si:H}$ is not clear yet. The second topic deals with the enormous impact of the deposition conditions on the photoluminescence (PL) features of $\mu\text{c-Si:H}$. Small deviations in those (gas flow rates, surface temperature, substrate properties, etc.) can lead to significant changes in the material properties, which are manifested by very different luminescence features. Among them, two PL peaks appear quite regularly. The first peak is related to tail-states of a-Si:H and is located between 1.2 eV and 1.3 eV. The second one is located between 0.9 eV and 1.0 eV and is related to tail-states of $\mu\text{c-Si:H}$ [LSB⁺83, MCK⁺06, YHW⁺00]. However, significant deviations were reported for those peaks. Both PL peaks reflect the structure of the amorphous/microcrystalline layer. Then it is obvious that the optical properties are related to the solar cell parameters. In this co-work with Andre Klosssek (cf.

[KMA⁺13, Klo13]), we considered both aspects the technological and material scientific one about microcrystalline silicon.

Both topics are discussed by combined PL and Raman investigations on 500 nm thick $\mu\text{c-Si:H}$ layers on glass substrates. It should be emphasized that the deposition conditions are actually used for the production of state-of-the-art a-Si:H/ $\mu\text{c-Si:H}$ tandem solar cells on glass substrate, consisting of a 260 nm thick a-Si:H top cell and a 1.8 μm thick $\mu\text{c-Si:H}$ bottom cell [SGC⁺13]. This study represents a more detailed investigation of such cells [KKA⁺13].

8.1. Samples and measurements

The investigated samples are a series of 500 nm thick intrinsic $\mu\text{c-Si:H}$ layers, deposited on $30 \times 30 \times 3.2 \text{ mm}^3$ glass substrates (*Float glass SGG Planilux*) by plasma enhanced chemical vapor deposition (PECVD). The deposition was performed using a capacitively coupled RF plasma with an excitation frequency of 13.56 MHz in an industrial-type AKT1600A cluster tool by Applied Materials. The RF power density, deposition pressure, substrate temperature, and electrode gap were 200 mW/cm^2 , 1.2 kPa, 190°C , and 18 mm, respectively. Different crystallinities were obtained by variations of the silane concentration between 0.2% and 0.9% in hydrogen. A 30 nm thick a-SiN_x layer was needed between glass and silicon to avoid delamination of the $\mu\text{c-Si:H}$ due to mechanical stress. Despite this, the stabilized thickness of the layer is limited to 500 nm instead of 1.8 μm , which is used in the tandem cells. Another difference is the plane substrate, which is in contrast to the conditions in the tandem cells with rougher interfaces. This can influence the growth of the $\mu\text{c-Si:H}$ (formation of cracks and shunts) [PMD⁺09].

For PL spectroscopy the setup described in Section 3.1 was used. The Raman measurements were performed at room temperatures using a laser of 532 nm wavelength with a spot size of about 10 μm (<50 mW) and a Si CCD camera. In both cases, PL and Raman, the laser power was set as low as possible to prevent any modifications of the crystalline structure of the sample ($\approx 500 \text{ W/cm}^2$).

8.2. Results and discussion

Raman investigations

Figure 8.1 shows the spectra recorded on six different samples with crystallinities ranging between pure amorphous and crystalline silicon. There are two distinct features observed in the spectra. One is a broad band at about 480 cm^{-1} and is related to the amorphous phase. The other is a quite sharp peak at about 520 cm^{-1} corresponding to crystalline silicon. Using those two peaks, one can determine the Raman crystallinity F_C . F_C is a well-established measure for the crystalline volume fraction of microcrystalline silicon. It is calculated by fitting five Gaussians to the spectrum, similar to the procedure described by Smit et al. [SvSD⁺03]. It is commonly extracted by deconvolution of the Raman spectra into the amorphous and crystalline components. F_C can then be calculated as

$$F_C = \frac{I_{505} + I_{520}}{I_{480} + I_{505} + I_{520}}, \quad (8.1)$$

where I_{480} , I_{505} , and I_{520} denote the intensities of the transverse optical mode of the amorphous, intermediate and crystalline phase, respectively. According the procedure above, we determined the crystallinities to 8 %, 23.1 %, 37.5 %, 52.4 %, and 77.1 %. It is obvious that the increasing crystallinity is clearly indicated by the increasing intensity of the peak associated with c-Si.

Besides the crystalline fraction, the spectra can also be used to estimate the size of the nano-grains. According to the peak shift of the c-Si peak at about 520 cm^{-1} ([VSI87]), the mean diameter of the nanocrystalline grains can be found. The different peak position and peak width were first discussed by Richter et al. [RWL81] and Campbell et al. [CF86]. They explained the redshift and broadening of the Raman signal by the relaxation of the phonon wave vector due to the smaller crystallite sizes. A similar approach can be used for Si nanowires [PCF⁺03, HDN⁺03], whereas the actual shape must be considered. The actual shape of our crystals is unknown due to missing high resolution TEM investigations. Therefore, the improved correlation between grain size and peak position especially for $\mu\text{c-Si:H}$ films by Ossadnik et al. [OVG99] was used to estimate the grain size. This is shown in Figure 8.2. There is a threshold value of crystallinity, which induces a significant change in the grain size. Below 40 % crystallinity, there are only small grains of about 3-4 nm. Above 50 %, the grains grow larger achieving sizes of around 25 nm for highly crystalline $\mu\text{c-Si:H}$. These values are in good agreement with TEM investigations carried out on similarly grown

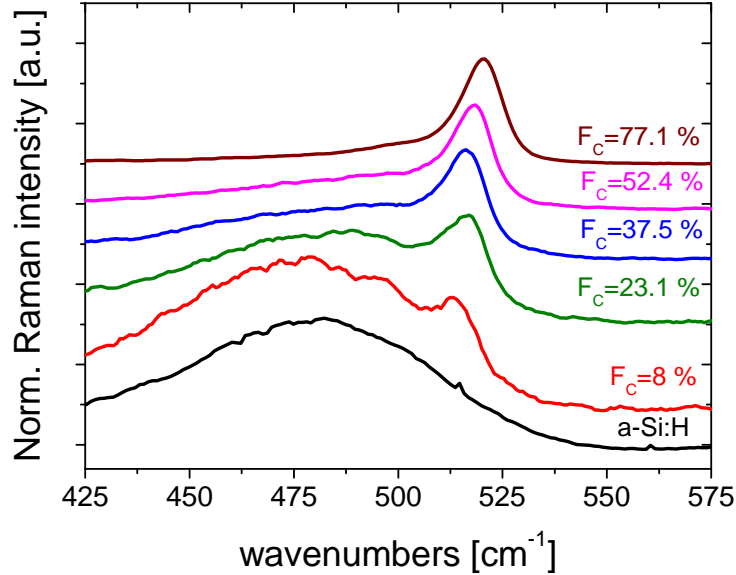


Figure 8.1.: Normalized Raman spectra of a-Si:H and $\mu\text{c-Si:H}$ samples with different Raman crystallinity F_C . The spectra are shifted vertically for better visibility.

samples (cf. [LHCF97, HLH⁺98]). For later interpretations of the estimated grain sizes, it must be considered that the reference assumes the missing of internal stress within the grains. We expect that this approach is quite plausible due to the relaxation of stress in the amorphous Si during the formation of nano-crystallites. It should be also considered that Raman spectroscopy is not able to distinguish between grains, which are isolated in a-Si:H matrix and those agglomerated to columns.

PL investigations

The measured PL spectra of the samples show luminescence from silicon and from the glass substrate as well. Here we analyze the spectra after subtracting the features related to the glass substrate.

The integrated PL intensity at 80 K is strongly dependent on the crystallinity of the sample. Here, the dependence on the Raman crystallinity is shown in Figure 8.3, where the total PL intensity is separated in the amorphous and crystalline components (cf. PL spectra in Fig. 8.5). All data can be fitted by exponential curves, whereas to total PL intensity decreases of more than two orders of magnitude. The main part of the luminescence is generated in amorphous Si up to crystallinities of about 40%. At higher values, the

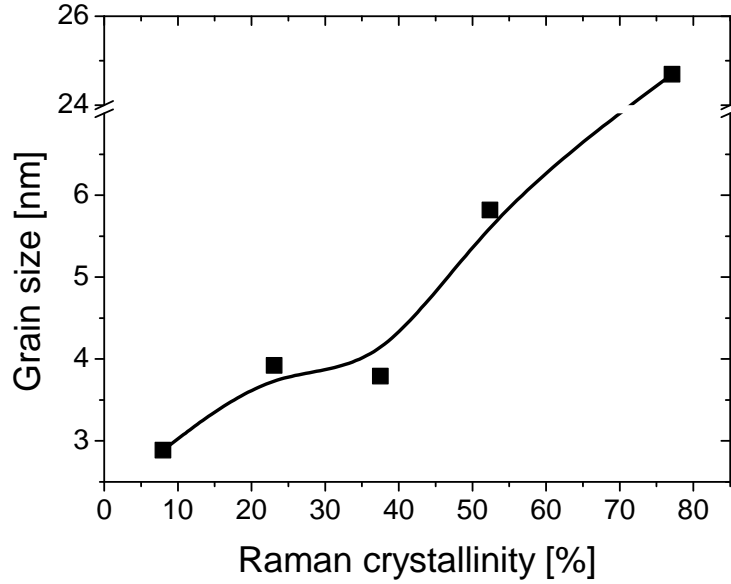


Figure 8.2.: Correlation between the measured Raman crystallinity and grain size extracted from [OVG99]. The corresponding spectra are shown in Figure 8.1.

crystalline components become more important. Note that the threshold value fits with that one for the appearance of larger grains obtained from Raman data.

More detailed investigations of the recombination mechanisms in μc -Si:H were performed by temperature dependent PL measurements to determine the activation energies, which describe the energetic positions of the tail-states within the band gap (e.g. the offset energy between the level E_T and the conduction band edge E_C). It was extracted by the following relation [SWS⁺85, SSS83]:

$$\frac{I(T)}{I(0)} = \frac{1}{1 + CT^{3/2} \exp(-E_A/k_B T)}, \quad (8.2)$$

where $I(T)$ is the intensity of the luminescence at temperature T , $I(0)$ is the intensity extrapolated to 0 K, and k_B is the Boltzmann constant. The term $CT^{3/2}$ is proportional to the degeneracy factor of the bound state and the density of states in the band, and E_A denotes the activation energy.

We found a correlation between the crystallinity and the activation energy (cf. Figure 8.4(a)). The dependence is nearly linear and it shows a decrease from about 130 meV for pure a-Si:H, which is in good agreement with literature data [EF77], to about 30 meV for

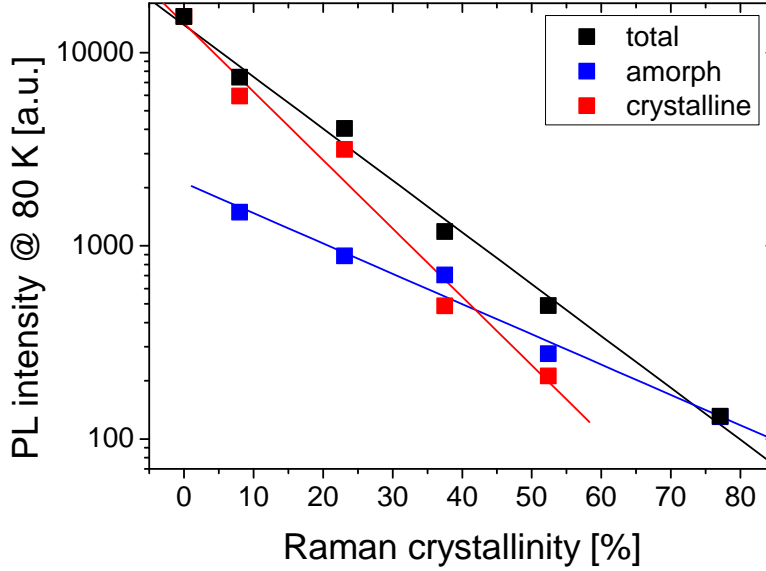


Figure 8.3.: Dependence of the PL intensity on the crystallinity: The PL intensity at 80 K shows an exponential decrease with increasing crystallinity. It is dominated by the amorphous components up to about 40% crystallinity. Luminescence from the crystalline components becomes important at higher crystallinities. Data are fitted by exponential curves.

highly crystalline $\mu\text{c-Si:H}$. This linear dependence could be interpreted as a presence of an additional energetic level or defect band between the tail-states and the conduction band edge. The position of that level depends on the crystalline fraction. We suggest that the level/defect band originates from the nano-grains and its energetic position is dependent by their size. The carriers captured in the tail-states deactivate in those level determined by the nano-crystallites. It mediates the activation of the tail-states. This is illustrated schematically in Figure 8.4(b).

Figure 8.5 shows PL spectra measured at 80 K of the Si samples. The spectra are normalized on maximum to emphasize the spectral distribution of the luminescence, because of the very strong differences in the PL intensity (cf. Figure 8.3).

Several Gaussian peaks can be used to deconvolve the curves. These peaks are labeled according to the corresponding radiative transition. For instance, pure a-Si:H shows a well-known spectrum consisting of two very broad peaks. The main one at about 1.2 eV is related to transitions between the tail-states and the smaller one belongs to radiative defects. This peak is located at about 0.9 eV. [Str80]

In case of $\mu\text{c-Si:H}$, four peaks can be distinguished, which have characteristic dependen-

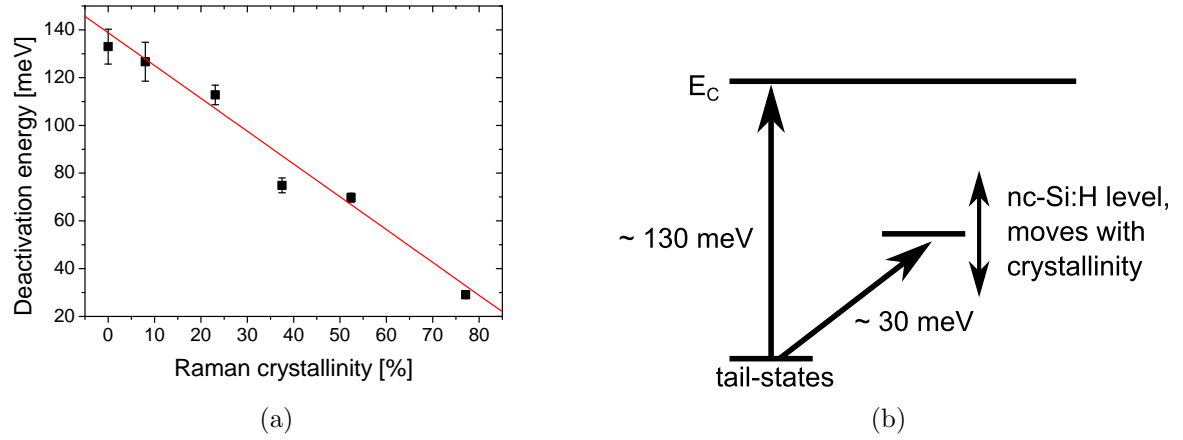


Figure 8.4.: Activation mechanisms in μc -Si:H: A linear decrease of the activation energies with increasing crystallinity is extracted (a); Scheme of the possible non-radiative recombination path in μc -Si:H (b).

cies on the crystallinity. Inverted commas in the labels are used to indicate differences in the properties of the peaks. The 'a'-Si:H peak (1.1 - 1.2 eV) represents the transition between tail-states in the a-Si:H matrix. The ' μc '-Si:H peak between 0.9 and 1 eV is related to tail-states of μc -Si:H. Similar results can be found in [KAS⁺85, YHMW00].

The peak at around 0.8 eV is related to defects in μc -Si:H. The position of this peak corresponds quite well with the data given in the literature. Depending on the deposition conditions, the 'defect' μc -Si:H peak can appear between 0.7 eV ([MCK⁺06]) and little above 0.8 eV [YLL⁺99]. The peak located at around 1.4 eV is associated with nanocrystalline silicon and therefore, labeled as 'nc'-Si:H. It was previously detected by Yue et al. [YLL⁺99]. There are different explanations for its energetic position. The original explanation considers band gap widening due to hydrogen. However, we suggest that quantum confinement effects are responsible for that.

Figure 8.6 shows the dependence of the peak position and peak width (FWHM) on the crystalline fraction of the sample. All peaks except the 'nc'-Si:H are characterized by a redshift with increasing crystallinity. Surprisingly, the 'nc'-Si:H peak shifts in the opposite direction. The nanocrystalline and amorphous peaks are characterized by a significant narrowing of the peak width with increasing crystallinity, whereas the width of the μc -Si:H peaks remain quite constant.

The most interesting PL peak is that one which is related to isolated nano-grains in the amorphous matrix, because of its specific dependencies on the crystallinity. The position

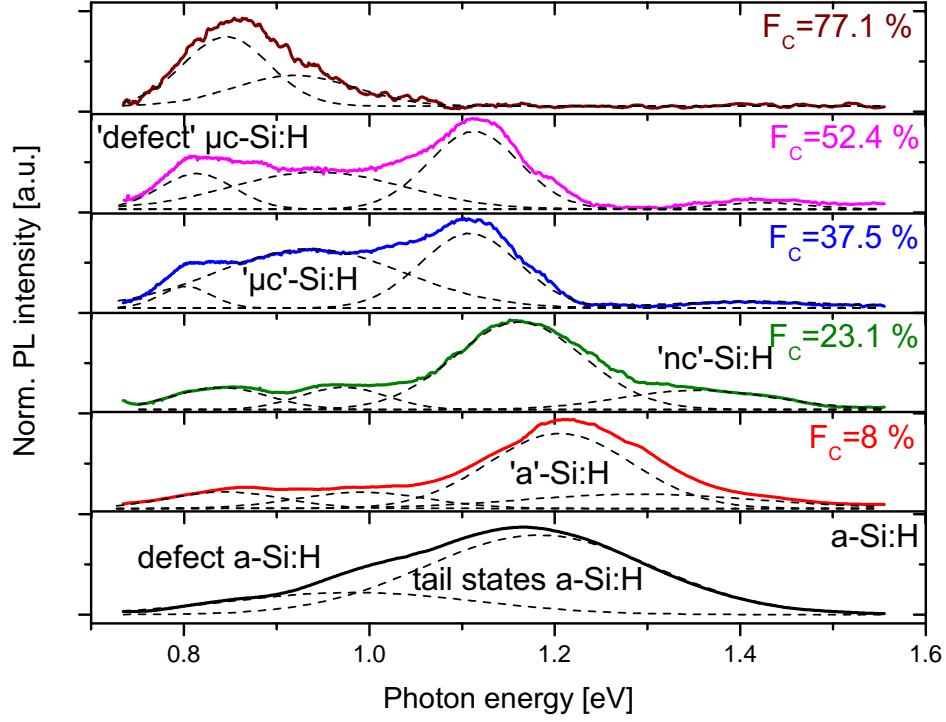
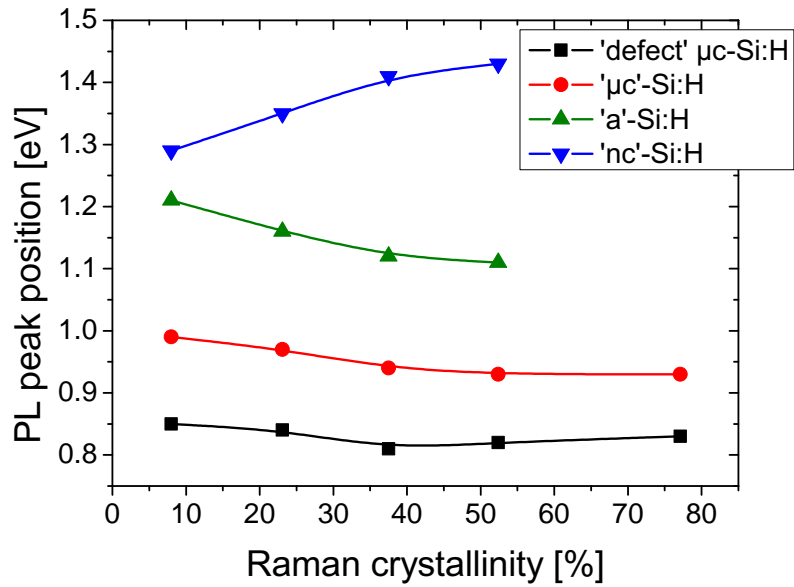


Figure 8.5.: Normalized PL spectra of the series of $\mu\text{c-Si:H}$ samples with different Raman crystallinity F_C at 80 K. Spectra are fitted by several Gaussian peaks (dashed lines). The labels are explained in the text.

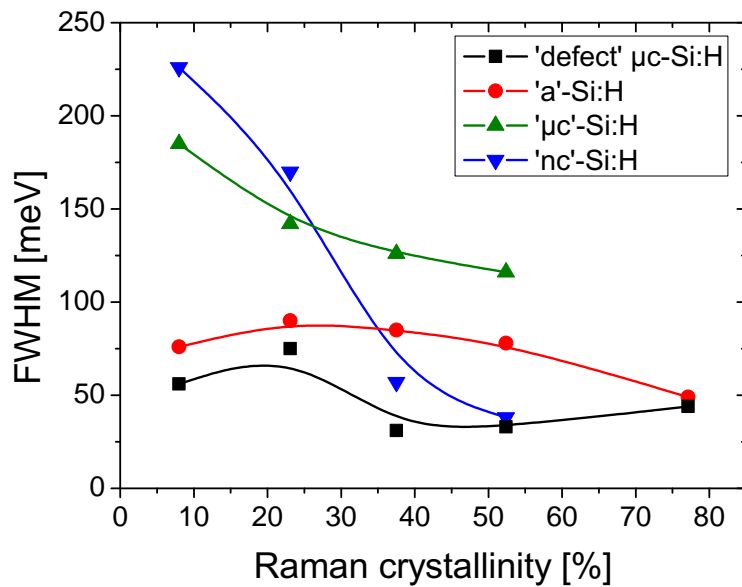
of the crystalline peaks is determined by the mean size of the grains in Raman and PL spectroscopy. Similarly to the case of Raman spectroscopy, an estimation of the size can be done by using the PL data. Nanocrystalline silicon is characterized by a strong correlation between the PL peak energy and the grain size. The smaller the grain size d the bluer is the maximum of the PL signal E . This is given by the equation [KPK⁺04]:

$$E = 1.16 + \frac{11.8}{d^2} \quad (8.3)$$

The detected peak energies can be understood based on quantum confinement, i.e., by the radiative recombination of electron-hole pairs confined in silicon nano-crystals. In this model, the recombination energy of the electron-hole pairs is shifted towards higher energies. Note that this equation 8.3 describes the relation in case of c-Si quantum dots



(a)



(b)

Figure 8.6.: Dependencies of the PL peak positions (a) and peak widths (FWHM) (b) on the Raman crystallinity.

in SiN_x . We were not able to find a reference where the quantum confinement of nc-Si:H in an a-Si:H matrix was investigated. The grain sizes are estimated by using the peak position of Figure 8.6 and calculated with Equation 8.3. The results are shown in Figure 8.7 in dependence on the crystallinity. The peak width might indicate a wide distribution of grain sizes, which decreases with increasing crystallinity.

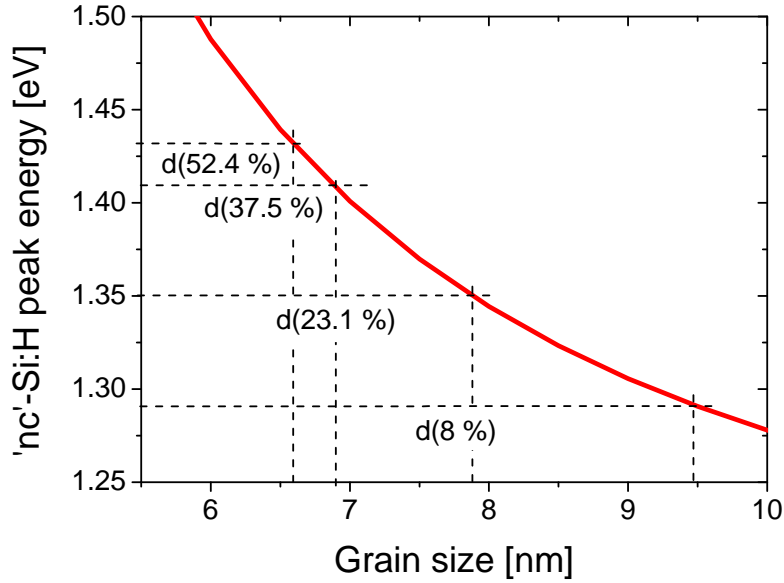


Figure 8.7.: Size of nc-Si:H grain in μc -Si:H samples: The grain sizes are extracted from 'nc'-Si:H peak position (cf. Fig. 8.6(a)) and calculated according to Eq. 8.3 [KPK⁺04].

The extracted sizes vary from 6 - 7 nm (52.4%) to 9 - 10 nm (8%). The value for the highly crystalline μc -Si:H sample agrees with the value obtained by Raman measurements. However, the general behavior of a decreasing grain size with increasing crystallinity is in clear contrast to the Raman results. We see two possible reasons for that behavior. The first one based on the different sensitivities of PL and Raman techniques. The Raman signal is proportional to the volume fraction of certain phase and respectively the larger crystals contribute more to the signal than the smaller ones. In contrast, the PL is more sensitive to the smaller crystals, because in the small crystals the momentum conservation rule is relaxed and band-to-band transitions are more probable. That is why the Raman and the PL spectroscopy have different weighting functions for the nanocrystalline size distribution. Thus, PL reflects the presence of small nano-crystal ensembles. Therefore, the PL results do not necessarily correlate with the Raman results. Moreover, the PL

results give information to the size distribution of the nanocrystalline fraction. The second reason for this surprising behavior of the extracted grain size considers the neighborhood of the grains. Quantum confinement is not dependent on the actual size of the grains only, but also on the barrier height caused by the surrounding material. In case of isolated nc-Si:H grains, the barrier between a-Si:H and c-Si:H should be higher than that one in the columnar structures, where the barrier is formed between different grains. Moreover, the significant decrease of the peak width indicates a higher affinity of larger grains to agglomeration in columnar structures. Therefore, the fraction of small grains remains detectable in the 'nc'-Si:H PL peak only. The decrease of the peak width is consistent with a narrowing of the size distribution of the nano-crystals at high crystalline fractions. However, combined data from Raman and PL can give better estimations of the actual grain sizes by comparing the results and considering the impact of several limitations.

The main contribution in the total PL intensity is from recombination in the amorphous phase ('a'-Si:H). An enormous decrease of the total PL intensity with increasing crystallinity (as shown in Figure 8.3) has been previously reported in literature. This can be explained by the reduction of PL intensity due to enhanced non-radiative recombination in the crystalline regions of the samples. There, the decrease is caused by a lower amount of trapped charge carriers in localized tail-states and the additional need of momentum conservation in the μ c-Si:H phase [YLL⁺99]. That can be illustrated by a very simple model, in that nanocrystalline grains are distributed homogeneously in amorphous silicon. Due to the relaxation of momentum conservation, the probability for radiative recombination in the amorphous regions of μ c-Si:H is much higher than in crystalline regions. So it can be simplified that the entire recombination rate R_{nr} is non-radiative. Then the PL intensity I_{PL} can be expressed as:

$$I_{PL} \sim G - R_{nr}, \quad (8.4)$$

where G is the generation rate. In this approach, the non-radiative recombination rate is determined by the probability of an excess charge carrier in a-Si:H reaching a nc-Si:H grain during thermalization and diffusion. If it reaches such a grain, it would recombine non-radiatively either due to recombination at the interface between the two silicon phases or within the crystal. In summary, the nano-crystals act as a total sink for excess charge carriers. Hence, the PL intensity is limited by the diffusion length of the excess charge carriers L and the mean distance between the nano-crystals or in other words the crystallinity.

This can be written as a sum over N grains with distances r_i :

$$I_{PL} \sim G - \sum_{i=1}^N \exp(-r_i/L) \quad (8.5)$$

This expression describes the measured behavior of the PL intensity. The shorter the mean distance (higher crystallinity) the lesser the PL intensity in exponential scale. This model fits to the behavior of the PL intensity in ranges of lower crystallinities (less than 40 %), where the amorphous regions are dominating. However, at higher crystallinities, the luminescence generated in the crystalline regions of the μc -Si:H has to be considered as well. Nevertheless, their contribution to the total PL intensity is rather low because of the additional need of momentum conservation.

Similar dependencies on the crystalline fraction can be observed for the spectral position and the peak width of the amorphous and μ -Si:H peaks. The 'a'-Si:H peak shifts to lower energies with increasing crystallinity. Its width decreases significantly from 290 meV (pure a-Si:H) to 110 meV (52.4% μc -Si:H). We suggest that this is a result of ordering in the amorphous silicon, in which the typical deviations of bond length and bonding angle of a-Si:H become reduced. The amorphous and nanocrystalline regions give a less contribution to luminescence with increasing crystallinity. At high crystallinity values, microcrystalline columns are dominating structures. These structures are characterized by the microcrystalline peaks in the PL spectra (' μc '-Si:H and 'defect' μc -Si:H). Whereas the μc -Si:H peak is related to tail-states in the bulk of the nano-crystals and the 'defect' μc -Si:H peak originates most probably at the boundaries of the grains. In highly crystalline μc -Si samples ($F_C = 77.1\%$), the grain boundaries in the columns become the prevailing factor due to a higher density of the grains. This is clearly indicated by the strong increase of the relative intensity of the 'defect' μc -Si:H peak. This observation agrees with measurements from Yue et al. [YLL⁺99].

We discuss the obtained results in a view of the theoretical models [Mat04], where the growth process of μc -Si:H can be separated into two main parts. The first part describes the nucleation of nanocrystalline grains at the surface, which are the basis for further crystallization/growth processes of μc -Si:H. Nucleation is mediated by a reaction of hydrogen with amorphous silicon. The exact type is considered to be either: surface-diffusion, etching or chemical-annealing; but it is not an objective of this study. Here, we consider the second part of the process, where the formation of crystalline islands in the a-Si:H matrix begins this moderated by the silane to hydrogen concentration and is responsible for the

amount of crystalline material in the layers. According to TEM measurements [VFC⁺00], these nucleation centers result in a columnar growth process with a very high amount of twin boundaries. The crystallinity is controlled by the hydrogen concentration during the growth. The higher the concentration of hydrogen, the higher the crystallinity. Besides the crystallinity, also the typical structures of the layer and its optical parameters change.

8.3. Summary

PL and Raman investigations were performed on 500 nm thick $\mu\text{c-Si:H}$ layers with different crystallinities. An exponential decrease of the total, amorphous and crystalline components of the PL intensity were observed with increasing crystallinity. The behavior of the amorphous ones could be explained by excess charge carriers generated in the amorphous region and non-radiative recombination at crystalline regions of $\mu\text{c-Si:H}$. Detailed temperature dependent measurements suggest the presence of a nanocrystalline level between the tail-states and the conduction band mediating a non-radiative recombination path in $\mu\text{c-Si:H}$. PL spectra indicate a process of ordering of a-Si:H is indicated by significant narrowing of the corresponding PL peak width. That represents lower deviations in bond length and bond angle. Isolated nc-Si:H grains in the a-Si:H matrix were associated with a PL peak at about 1.4 eV. It is characterized by specific peak energy and peak width, which is dependent on the crystallinity of $\mu\text{c-Si:H}$. This was used to determine the grain size by accounting for the quantum confinement effects. Combined with Raman data, estimations of the grain sizes were suggested. At lower crystallinities a broad distribution of grain sizes with a mean value around 3 - 4 nm was found. At higher crystallinities, the grains grow further up to 25 nm.

9. Conclusions

In this work, multicrystalline silicon solar cells and polycrystalline silicon thin film on glass cells were investigated by electro- and photoluminescence techniques.

Using a photoluminescence imaging system, which delivers band-to-band (BB) as well as defect-related (D1) luminescence images, is much more suitable for characterizing solar wafers at different processing steps than the analysis of band-to-band images only. Investigating both, BB and D1 images, the impact of surface recombination activity can be excluded.

Spectroscopic photoluminescence investigations on bulk multicrystalline silicon wafer showed a new line, which is labeled “Di” luminescence. This new line is very intense, even at room temperature and under low injection conditions. It is located near the D3 line, particularly at 0.93 eV at liquid nitrogen temperature and 0.91 eV at room temperature. This line can be detected with an appropriate filter and an InGaAs camera by electro- or photoluminescence imaging at room temperature. The energy barrier of 120 meV, obtained by temperature dependent PL, CL and EBIC analysis, support the involvement of Frank partials.

Oxygen-related luminescence could be detected in the range of 0.8 eV at liquid nitrogen temperatures. In this range, the D1 luminescence is detectable. Deconvolution of D1 and oxygen-related luminescence peaks reveal that usually both kinds of luminescence coexist. The D1 peak is located at 810 meV, whereas peaks at 780 meV and 850 meV are responsible for oxygen. The presence of oxygen in this luminescence is also supported by the appearance of Di luminescence in these regions. Oxygen precipitates tend to create stacking faults, and at the rim of these stacking faults, Frank partials occur.

The investigated silicon thin films have similar optical properties as bulk multicrystalline silicon. Differences were found in the extended dislocation-rich grains, those are rather

uncommon in bulk material. These defect-rich grains exhibit almost all of the silicon defect lines D1 to D4 at low temperatures.

Electroluminescence imaging of band-to-band and defect-related luminescence could be correlated with reverse bias electroluminescence in the near-infrared part in multicrystalline silicon solar cells. A spatial separation between defects and grain boundaries emitting defect-related luminescence and defects emitting reverse bias electroluminescence was observed by high-resolution imaging. Moreover, an interaction between radiative defects and non-radiative defects in the vicinity has been indicated. This could lead to a reduced affinity for breakdown near radiative defects.

Electroluminescence imaging on silicon thin films showed, that this material is quite complementary to bulk multicrystalline silicon. The interlayer between glass substrate and silicon layer affect the formation of misfit dislocations, and, subsequently the material properties. Defect-related luminescence is not only observed at grain boundaries, relatively large defect-rich grains emit defect-related luminescence, too. Reverse bias electroluminescence is observable in thin film cells, but it appears very rarely.

Comparative PL and FTIR investigations on multicrystalline silicon block material showed some unexpected results. With increasing block height, the oxygen content and the band-to-band luminescence, and thus the effective charge carrier lifetime, decreases. Additionally, a correlation between D3/D4 luminescence profile and nitrogen distribution in the block could be observed. Here, two blocks were investigated only. To get a better understanding of these correlations much more blocks should be analyzed with these methods.

Combined Raman and photoluminescence investigations on $\mu\text{c-Si:H}$ layers of various crystallinities allow a suggestion of a stepwise transformation process from amorphous to microcrystalline silicon. Comparisons with theoretical models show good agreements. For instance, the suggested ordered form of a-Si:H ('a'-Si:H) could be associated with a-Si:H, which is affected by structural changes induced by hydrogen, where the interactions with hydrogen results in substitution of stronger Si-Si bonds instead of weak a-Si:H bonds. This provides the basis for the formation of nc-Si:H. A special care should be on the presence of 'a'-Si:H and 'nc'-Si:H.

Scientific visibility

Publications

Properties of strong luminescence at 0.93eV in solar grade silicon

C. Krause, T. Arguirov, W. Seifert, D. Mankovics, H.M. Krause, M. Kittler
Solid State Phenomena 205-206, 83-88 (2014)

On the origin of intense luminescence at 0.93eV in multicrystalline silicon

C. Krause, D. Mankovics, H.-M. Krause, T. Arguirov, M. Kittler
J. Appl. Phys. 114, 034902 (2013)

Growth process of microcrystalline silicon studied by combined photoluminescence and Raman investigations

A. Klossek, D. Mankovics, T. Arguirov, M. Ratzke, S. Kirner, F. Friedrich, O. Gabriel, B. Stannowski, R. Schlatmann and M. Kittler
J. Appl. Phys. 114, 223511 (2013)

Distribution of defects and breakdown sites in mc-Si solar cells studied by luminescence imaging

A. Klossek, D. Mankovics, M. Kittler
Energy Procedia 27, 143 (2012)

Dislocation-related photoluminescence imaging of mc-Si wafers at room temperature

D. Mankovics, R.P. Schmid, T. Arguirov, M. Kittler
Crystal Research and Technology 47(11), 1148 (2012)

Luminescence of defects and breakdown sites in multicrystalline Si solar cells

D. Mankovics, A. Klossek, Ch. Krause, T. Arguirov, W. Seifert, M. Kittler
Phys. Stat. Sol. A 209(10), 1908 (2012)

Rapid dislocation-related D1 photoluminescence imaging of multicrystalline Si wafers at room temperature

R.P. Schmid, D. Mankovics, T. Arguirov, M. Ratzke, T. Mchedlidze, M. Kittler
Phys. Stat. Sol. A 208, 888 (2011)

Novel imaging techniques for dislocation-related D1 photoluminescence of multicrystalline Si wafers: two different approaches

R. Schmid, D. Mankovics, T. Arguirov, T. Mchedlidze, M. Kittler
Phys. Stat. Sol. C 8, 1297 (2011)

Presentations

Combined investigation of scanning photoluminescence and camera based imaging techniques on thin-film silicon on glass substrate

D. Mankovics, A. Klossek, D. Amkreutz, M. Kittler
12th International Workshop on Beam Injection Assessment of Microstructures (BIAMS 2014), June 22-26, 2014, Tsukuba, Japan

PVcomB - TV 6 "Optische und elektrische Defektanalytik"

D. Mankovics, C. Krause, W. Seifert, M. Kittler
Projekttreffen PVcomB, 03. July 2014, Berlin, Germany

Luminescence of defects and breakdown sites in multicrystalline Si solar cells

D. Mankovics, A. Klossek, Ch. Krause, T. Arguirov, W. Seifert, M. Kittler
E-MRS Spring Meeting, May 14 - 18, 2012, Strasbourg, France

ReBEL an mc-Si in Korrelation zu Defekt- und BB-Lumineszenz

D. Mankovics, A. Klossek
Projekttreffen SolarWinS, January 17-19, 2012, Arnstadt, Germany

Dislocation-related photoluminescence imaging of mc-Si wafers at room temperature

D. Mankovics, R. Schmid, T. Arguirov, M. Kittler
GPCCG 2011, March 14-18, 2011, Frankfurt (Oder)/Slubice, Germany/Poland

Fast photoluminescence imaging of mc-Si

D. Mankovics
UMG-Projekttreffen, March 31, 2011, Frankfurt (Oder), Germany

Defektcharakterisierung in mc-Si: Vergleichende Untersuchungen mit PL-Mapping und Spektroskopie, PL-Imaging und Kathodolumineszenz

D. Mankovics, Ch. Krause, T. Arguirov

Projekttreffen SolarWinS, July 5-7, 2011, Ochsenfurt, Germany

References

- [AMS⁺11] D. Amkreutz, J. Müller, M. Schmidt, T. Hänel, and T. F. Schulze. Electron-beam crystallized large grained silicon solar cell on glass substrate. *Progress in Photovoltaics: Research and Applications*, 19(8):937–945, 2011.
- [Arg07] Tzanimir Arguirov. *Electro-optical properties of dislocations in silicon and their possible application for light emitters*. PhD thesis, Brandenburgische Technische Universität Cottbus, 2007.
- [ARI06] V.D. Akhmetov, H. Richter, and N. Inoue. Determination of low concentrations of n and c in cz-si by precise ft-ir spectroscopy. *Materials Science and Engineering: B*, 134(2-3):207–212, 2006. {EMRS} 2006, Symposium V; Advanced Silicon for the 21st Century.
- [BBB⁺11] Otwin Breitenstein, Jan Bauer, Karsten Bothe, Wolfram Kwapil, Dominik Lausch, Uwe Rau, Jan Schmidt, Matthias Schneemann, Martin C. Schubert, Jan-Martin Wagner, and Wilhelm Warta. Understanding junction breakdown in multicrystalline solar cells. *Journal of Applied Physics*, 109(7):071101, 2011.
- [BFM12] K. Bothe, R. J. Falster, and J. D. Murphy. Room temperature sub-bandgap photoluminescence from silicon containing oxide precipitates. *Applied Physics Letters*, 101(3):032107, 2012.
- [BKP⁺97] Shen Bo, Yang Kai, Chen Peng, Zhang Rong, Shi Yi, Zheng You-dou, T Sekiguchi, and K Sumino. Electrical activity of frank partial dislocations and the influence of metallic impurities in czochralski-grown silicon. *Chinese Physics Letters*, 14(6):436, 1997.
- [BRH⁺09] K. Bothe, K. Ramspeck, D. Hinken, C. Schinke, J. Schmidt, S. Herlufsen, R. Brendel, J. Bauer, J.-M. Wagner, N. Zakharov, and O. Breitenstein. Luminescence emission from forward- and reverse-biased multicrystalline silicon solar cells. *Journal of Applied Physics*, 106(10):104510, 2009.

- [BSD⁺02] S. Binetti, R. Somaschini, A. Le Donne, E. Leoni, S. Pizzini, D. Li, and D. Yang. Dislocation luminescence in nitrogen-doped czochralski and float zone silicon. *Journal of Physics: Condensed Matter*, 14(48):13247, 2002.
- [CF86] I.H. Campbell and P.M. Fauchet. The effects of microcrystal size and shape on the one phonon raman spectra of crystalline semiconductors. *Solid State Communications*, 58(10):739 – 741, 1986.
- [CFB⁺97] R. Carius, F. Finger, U. Backhausen, M. Luysberg, P. Hapke, L. Houben, M. Otte, and H. Overhof. Electronic properties of microcrystalline silicon. *MRS Proceedings*, 467, 1 1997.
- [CM56] A. G. Chynoweth and K. G. McKay. Photon emission from avalanche breakdown in silicon. *Phys. Rev.*, 102:369–376, Apr 1956.
- [DBP10] G. Dhanaraj, K. Byrappa, and V. Prasad. *Springer Handbook of Crystal Growth*. Springer London, Limited, 2010.
- [DN76] Tkachev V.D. Drozdov N.A., Patrín A.A. Recombination radiation on dislocations in silicon. *Sov. Phys. JETP Lett.*, 23(11):597, 1976.
- [DS77] J. Dziewior and W. Schmid. Auger coefficients for highly doped and highly excited silicon. *Applied Physics Letters*, 31(5):346–348, 1977.
- [EF77] D. Engemann and R. Fischer. Photoluminescence in amorphous silicon. *physica status solidi (b)*, 79(1):195–202, 1977.
- [FCH⁺96] F. Finger, R. Carius, P. Hapke, L. Houben, M. Luysberg, and M. Tzolov. Growth and structure of microcrystalline silicon prepared with glow discharge at various plasma excitation frequencies. *MRS Proceedings*, 452, 1 1996.
- [FK76] H. Foell and B. O. Kolbesen. Agglomerate von zwischengitteratomen (swirldefekte) in silizium - ihre bedeutung für grundlagenforschung und technologie. *Jahrbuch der Akademie der Wissenschaften in Göttingen*, page 27, 1976.
- [FKY⁺05] Takashi Fuyuki, Hayato Kondo, Tsutomu Yamazaki, Yu Takahashi, and Yukiharu Uraoka. Photographic surveying of minority carrier diffusion length in polycrystalline silicon solar cells by electroluminescence. *Applied Physics Letters*, 86(26):262108, 2005.

-
- [Foe14] Helmut Foell. Defects in crystals. Hyperscript, July 2014.
- [Gru10] Marius Grundmann. *The Physics of Semiconductors*. Springer, 2nd edition, 2010.
- [Hal52] R. N. Hall. Electron-hole recombination in germanium. *Phys. Rev.*, 87(2):387, Jul 1952.
- [HDN⁺03] S. Hofmann, C. Ducati, R. J. Neill, S. Piscanec, A. C. Ferrari, J. Geng, R. E. Dunin-Borkowski, and J. Robertson. Gold catalyzed growth of silicon nanowires by plasma enhanced chemical vapor deposition. *Journal of Applied Physics*, 94(9):6005–6012, 2003.
- [HDTO06] S. He, S. Danyluk, I. Tarasov, and S. Ostapenko. Residual stresses in polycrystalline silicon sheet and their relation to electron-hole lifetime. *Applied Physics Letters*, 89(11):111909, 2006.
- [HGKR09] J. Haunschild, M. Glatthaar, W. Kwapil, and S. Rein. Comparing luminescence imaging with illuminated lock-in thermography and carrier density imaging for inline inspection of silicon solar cells. *24th European Photovoltaic Solar Energy Conference, Hamburg, Germany (21-25 Sept. 2009)*, pages 857–862, 2009.
- [HL82] J.P. Hirth and J. Lothe. *Theory of dislocations*. Wiley, 1982.
- [HLH⁺98] L. Houben, M. Luysberg, P. Hapke, R. Carius, F. Finger, and H. Wagner. Structural properties of microcrystalline silicon in the transition from highly crystalline to amorphous growth. *Philosophical Magazine A*, 77(6):1447–1460, 1998.
- [Hou98] L. Houben. *Plasmaabscheidung von mikrokristallinem Silizium : Merkmale und Mikrostruktur und deren Deutung im Sinne von Wachstumsvorgängen*. PhD thesis, Heinrich-Heine-Universität Düsseldorf, 1998.
- [IEA10] IEA/OECD. *Technology Roadmap - Solar photovoltaic energy*. International Energy Agency, 2010.

- [IST⁺08] M. Inoue, H. Sugimoto, M. Tajima, Y. Ohshita, and A. Ogura. Microscopic and spectroscopic mapping of dislocation-related photoluminescence in multicrystalline silicon wafers. *Journal of Materials Science: Materials in Electronics*, 19(1):132–134, 2008.
- [Jia09] Goubin Jia. *Characterization of electrical and optical properties of silicon based materials*. PhD thesis, Brandenburgische Technische Universität Cottbus, 2009.
- [JMU13] Supawan Joonwichien, Satoru Matsushima, and Noritaka Usami. Effects of crystal defects and their interactions with impurities on electrical properties of multicrystalline si. *Journal of Applied Physics*, 113(13):133503, 2013.
- [JP07] J. Jedlička and M. Potůčková. Correction of radial distortion in digital images. Proceedings Technical Computing Prague 2007, 2007.
- [KAR⁺14] M. Kittler, T. Arguirov, M. Reiche, C. Krause, and D. Mankovics. About dislocation and oxygen related luminescence of si around 0.8 ev. Presentation EDS 2014 Göttingen, September 2014.
- [KAS⁺85] Shuji Komuro, Yoshinobu Aoyagi, Yusaburo Segawa, Susumu Namba, Akio Masuyama, Dusit Kruangam, Hiroaki Okamoto, and Yoshihiro Hamakawa. Steady?state and time?resolved photoluminescence in microcrystalline silicon. *Journal of Applied Physics*, 58(2):943–947, 1985.
- [KAS⁺13] C. Krause, T. Arguirov, W. Seifert, D. Mankovics, H.-M. Krause, and M. Kittler. Properties of strong luminescence at 0.93 ev in solar grade silicon. *Solid State Phenomena*, 205-206:83–88, 2013.
- [KBS⁺04] V. Kveder, M. Badylevich, E. Steinman, A. Izotov, M. Seibt, and W. Schröter. Room-temperature silicon light-emitting diodes based on dislocation luminescence. *Applied Physics Letters*, 84(12):2106–2108, 2004.
- [KKA⁺13] A. Klossek, C. Krause, T. Arguirov, H.-M. Krause, W. Seifert, F. Friedrich, S. Calnan, O. Gabriel, B. Stannowski, and M. Kittler. Characterization of thin-film a-si:h/ μ c-si:h tandem solar cells on glass substrates. *Crystal Research and Technology*, 48(5):279–286, 2013.

- [KKG⁺09] Wolfram Kwapil, Martin Kasemann, Paul Gundel, Martin C. Schubert, Wilhelm Warta, Paula Bronsveld, and Gianluca Coletti. Diode breakdown related to recombination active defects in block-cast multicrystalline silicon solar cells. *Journal of Applied Physics*, 106(6):063530, 2009.
- [Klo13] André Klossek. *Optical characterization of thin-film Si solar cells and knowledge transfer from bulk mc-Si*. PhD thesis, Brandenburgische Technische Universität Cottbus, 2013.
- [KLP77] L. C. Kimerling, H. J. Leamy, and J. R. Patel. The electrical properties of stacking faults and precipitates in heat-treated dislocation-free czochralski silicon. *Applied Physics Letters*, 30(5):217–219, 1977.
- [KMA⁺09] Martin Kittler, Teimuraz Mchedlidze, Tzanimir Arguirov, Winfried Seifert, Manfred Reiche, and Thomas Wilhelm. Silicon based ir light emitters. *physica status solidi (c)*, 6(3):707–715, 2009.
- [KMA⁺13] A. Klossek, D. Mankovics, T. Arguirov, M. Ratzke, S. Kirner, F. Friedrich, O. Gabriel, B. Stannowski, R. Schlatmann, and M. Kittler. Growth process of microcrystalline silicon studied by combined photoluminescence and raman investigations. *Journal of Applied Physics*, 114(22):223511, 2013.
- [KMK⁺13] Christoph Krause, Daniel Mankovics, Hans-Michael Krause, Tzanimir Arguirov, and Martin Kittler. On the origin of intense luminescence at 0.93 eV from multi-crystalline silicon. *Journal of Applied Physics*, 114(3):034902, 2013.
- [KOT⁺99] Y. Koshka, S. Ostapenko, I. Tarasov, S. McHugo, and J. P. Kalejs. Scanning room-temperature photoluminescence in polycrystalline silicon. *Applied Physics Letters*, 74(11):1555–1557, 1999.
- [KPK⁺04] Tae-Youb Kim, Nae-Man Park, Kyung-Hyun Kim, Gun Yong Sung, Young-Woo Ok, Tae-Yeon Seong, and Cheol-Jong Choi. Quantum confinement effect of silicon nanocrystals in situ grown in silicon nitride films. *Applied Physics Letters*, 85(22):5355–5357, 2004.
- [KRW06] Thomas Kieliba, Stephan Riepe, and Wilhelm Warta. Effect of dislocations on minority carrier diffusion length in practical silicon solar cells. *Journal of Applied Physics*, 100(6):063706, 2006.

- [KSA⁺02] M. Kittler, W. Seifert, T. Arguirov, I. Tarasov, and S. Ostapenko. Room-temperature luminescence and electron-beam-induced current (ebic) recombination behaviour of crystal defects in multicrystalline silicon. *Solar Energy Materials and Solar Cells*, 72(1-4):465 – 472, 2002.
- [KSDT89] W. Kürner, R. Sauer, A. Dörnen, and K. Thonke. Structure of the 0.767-ev oxygen-carbon luminescence defect in 450 °c thermally annealed czochralski-grown silicon. *Phys. Rev. B*, 39:13327–13337, Jun 1989.
- [KSP⁺03] A J Kenyon, E A Steinman, C W Pitt, D E Hole, and V I Vdovin. The origin of the 0.78 ev luminescence band in dislocated silicon. *Journal of Physics: Condensed Matter*, 15(39):S2843, 2003.
- [LH03] Antonio Luque and Steven Hegedus, editors. *Handbook of Photovoltaic Science and Engineering*. Wiley, 2003.
- [LHCF97] M. Luysberg, P. Hapke, R. Carius, and F. Finger. Structure and growth of hydrogenated microcrystalline silicon: Investigation by transmission electron microscopy and raman spectroscopy of films grown at different plasma excitation frequencies. *Philosophical Magazine A*, 75(1):31–47, 1997.
- [LRR⁺92] Y. S. Lelikov, Y. T. Rebane, S. Ruvimov, A. A. Sitnikova, D. V. Tarhin, and Y. G. Shreter. A classification of the dislocation-related photoluminescence in silicon. *physica status solidi (b)*, 172:53–63, Jul 1992.
- [LSB⁺83] PG LeComber, WE Spear, PK Bhat, G Diprose, TM Searle, and IG Austin. Plasma deposited microcrystalline and amorphous silicon - a comparative study of photoluminescence. *Physica B+C*, 117-118, Part 2(0):917 – 919, 1983.
- [Man11] Daniel Mankovics. Defect monitoring using a luminescence imaging technique for mc-si solar wafers. Diploma-thesis, March 2011.
- [Mat04] Akihisa Matsuda. Microcrystalline silicon.: Growth and device application. *Journal of Non-Crystalline Solids*, 338-340(0):1 – 12, 2004. Proceedings of the 20th International Conference on Amorphous and Microcrystalline Semiconductors.

- [MCK⁺06] T. Merdzhanova, R. Carius, S. Klein, F. Finger, and D. Dimova-Malinovska. Defect states in microcrystalline silicon probed by photoluminescence spectroscopy. *Thin Solid Films*, 511?512(0):394 – 398, 2006. {EMSR} 2005 - Proceedings of Symposium F on Thin Film and Nanostructured Materials for Photovoltaics {EMRS} 2005- Symposium F {EMSR} 2005 - Proceedings of Symposium F on Thin Film and Nanostructured Materials for Photovoltaics.
- [MFL⁺02] H.J. Möller, C. Funke, A. Lawerenz, S. Riedel, and M. Werner. Oxygen and lattice distortions in multicrystalline silicon. *Solar Energy Materials and Solar Cells*, 72(1-4):40 –416, 2002. {EMRS} 2001 Symposium E: Crystalline Silicon for Solar Cells.
- [MK12] T. Mchedlidze and M. Kittler. Investigation of defect states in heavily dislocated thin silicon films. *Journal of Applied Physics*, 111(5):053706, 2012.
- [MKA⁺09] T. Mchedlidze, O. Kononchuk, T. Arguirov, M. Trushin, M. Reiche, and M. Kittler. Determination of the origin of dislocation related luminescence from silicon using regular dislocation networks. *Solid State Phenomena*, 156-158:567–572, 2009.
- [Möl06] H.-J. Möller. Wafering of silicon crystals. *physica status solidi (a)*, 203:659–669, Mar 2006.
- [MM81] N. S. Minaev and A. V. Mudryi. Thermally-induced defects in silicon containing oxygen and carbon. *physica status solidi (a)*, 68(2):561–565, 1981.
- [MSAK12] D. Mankovics, R. P. Schmid, T. Arguirov, and M. Kittler. Dislocation-related photoluminescence imaging of mc-si wafers at room temperature. *Crystal Research and Technology*, 47(11):1148–1152, 2012.
- [MSD⁺06] F. Meillaud, A. Shah, C. Droz, E. Vallat-Sauvain, and C. Miazza. Efficiency limits for single-junction and tandem solar cells. *Solar Energy Materials and Solar Cells*, 90(18?19):2952 – 2959, 2006. 14th International Photovoltaic Science and Engineering Conference 14th International Photovoltaic Science and Engineering Conference.
- [New55] Roger Newman. Visible light from a silicon $p-n$ junction. *Phys. Rev.*, 100:700–703, Oct 1955.

- [NU09] Kazuo Nakajima and Noritaka Usami, editors. *Crystal Growth of Si for Solar Cells*. Springer, 2009.
- [OTK⁺00] S. Ostapenko, I. Tarasov, J. P. Kalejs, C. Haessler, and E.-U. Reisner. Defect monitoring using scanning photoluminescence spectroscopy in multicrystalline silicon wafers. *Semiconductor Science and Technology*, 15(8):840, 2000.
- [OVG99] Ch Ossidnik, S Vep?ek, and I Gregora. Applicability of raman scattering for the characterization of nanocrystalline silicon. *Thin Solid Films*, 337(1?2):148 – 151, 1999.
- [Pan75] Jacques I. Pankove. *Optical Processes in Semiconductors*. Dover Publications, Inc., 1975.
- [PCF⁺03] S. Piskanec, M. Cantoro, A. C. Ferrari, J. A. Zapien, Y. Lifshitz, S. T. Lee, S. Hofmann, and J. Robertson. Raman spectroscopy of silicon nanowires. *Phys. Rev. B*, 68:241312, Dec 2003.
- [PLB⁺04] S. Pizzini, E. Leonie, S. Binetti, M. Acciarri, A. Le Donne, and B. Pichaud. Luminescence of dislocations and oxide precipitates in si. *Solid State Phenomena*, 95-96:273–282, 2004.
- [PMD⁺09] M. Python, O. Madani, D. Dominé, F. Meillaud, E. Vallat-Sauvain, and C. Ballif. Influence of the substrate geometrical parameters on microcrystalline silicon growth for thin-film solar cells. *Solar Energy Materials and Solar Cells*, 93(10):1714 – 1720, 2009.
- [RNI⁺05] M. Rossberg, M. Naumann, K. Irmscher, U. Juda, A. Lüdge, Michael Ghosh, and Armin Müller. Investigation of defects in the edge region of multicrystalline solar silicon ingots. *Solid State Phenomena*, 108-109:531–538, 2005.
- [RRR⁺03] B. Rech, T. Roschek, T. Repmann, J. Müller, R. Schmitz, and W. Appenzeller. Microcrystalline silicon for large area thin film solar cells. *Thin Solid Films*, 427(1?2):157 – 165, 2003. Proceedings of Symposium K on Thin Film Materials for Large Area Electronics of the European Materials Research Society (E-MRS) 2002 Spring Conference.
- [RTJ⁺10] C. Reimann, M. Trempa, T. Jung, J. Friedrich, and G. Müller. Modeling of incorporation of o, n, c and formation of related precipitates during directional

- solidification of silicon under consideration of variable processing parameters. *Journal of Crystal Growth*, 312(7):878 – 885, 2010.
- [RWL81] H. Richter, Z.P. Wang, and L. Ley. The one phonon raman spectrum in microcrystalline silicon. *Solid State Communications*, 39(5):625 – 629, 1981.
- [SAA⁺11] W. Seifert, D. Amkreutz, T. Arguirov, H. M. Krause, and M. Schmidt. Analysis of electron-beam crystallized large grained si films on glass substrate by ebic, ebsd and pl. *Solid State Phenomena*, 178-179:116–121, August 2011.
- [SAT⁺07] H. Sugimoto, K. Araki, M. Tajima, T. Eguchi, I. Yamaga, M. Dhamrin, K. Kamisako, and T. Saitoh. Photoluminescence analysis of intragrain defects in multicrystallinesilicon wafers for solar cells. *Journal of Applied Physics*, 102(5):054506, 2007.
- [Sch06a] Dieter K. Schroder. *Semiconductor Material and Device Characterization*. John Wiley & Sons, Inc., third edition edition, 2006.
- [Sch06b] E. Fred Schubert. *Light-Emitting Diodes*. Cambridge University Press, 2nd edition edition, 2006.
- [SGC⁺13] B. Stannowski, O. Gabriel, S. Calnan, T. Frijnts, A. Heidelberg, S. Neubert, S. Kirner, S. Ring, M. Zelt, B. Rau, J.-H. Zollondz, H. Bloess, R. Schlattmann, and B. Rech. Achievements and challenges in thin film silicon module production. *Solar Energy Materials and Solar Cells*, 119(0):196 – 203, 2013. Thin-film Photovoltaic Solar Cells.
- [SGT⁺08] M.C. Schubert, P. Gundel, M. The, W. Warta, M. Romero, S. Ostapenko, and T. Arguirov. Spatially resolved luminescence spectroscopy on multicrystalline silicon. *23rd European Photovoltaic Solar Energy Conference, Valencia, Spain (1-5 Sept. 2008)*, pages 17–23, 2008.
- [SGW04] O. Schultz, S. W. Glunz, and G. P. Willeke. Short communication: Accelerated publication: Multicrystalline silicon solar cells exceeding 20% efficiency. *Progress in Photovoltaics: Research and Applications*, 12:553–558, Nov 2004.
- [SHTDB10] T. Söderström, F.-J. Haug, V. Terrazzoni-Daudrix, and C. Ballif. Flexible micromorph tandem a-si/ μ c-si solar cells. *Journal of Applied Physics*, 107(1):014507, 2010.

- [SKS94] T. Sekiguchi, V. V. Kveder, and K. Sumino. Hydrogen effect on the optical activity of dislocations in silicon introduced at room temperature. *Journal of Applied Physics*, 76(12):7882–7888, 1994.
- [SMA⁺11a] R. P. Schmid, D. Mankovics, T. Arguirov, T. Mchedlidze, and M. Kittler. Novel imaging techniques for dislocation-related d1-photo-luminescence of multicrystalline si wafers - two different approaches. *physica status solidi (c)*, 8(4):1297–1301, 2011.
- [SMA⁺11b] R. P. Schmid, D. Mankovics, T. Arguirov, M. Ratzke, T. Mchedlidze, and M. Kittler. Rapid dislocation-related d1-photoluminescence imaging of multicrystalline si wafers at room temperature. *physica status solidi (a)*, 208(4):888–892, 2011.
- [SR52] W. Shockley and W. T. Read. Statistics of the recombinations of holes and electrons. *Phys. Rev.*, 87(5):835–842, Sep 1952.
- [SRLW07] G. Stokkan, S. Riepe, O. Lohne, and W. Warta. Spatially resolved modeling of the combined effect of dislocations and grain boundaries on minority carrier lifetime in multicrystalline silicon. *Journal of Applied Physics*, 101(5):–, 2007.
- [SS96] T. Sekiguchi and K. Sumino. Cathodoluminescence study on dislocations in silicon. *Journal of Applied Physics*, 79(6):3253–3260, 1996.
- [SSPR09] M. Schumann, M. Singh, T. Orellana Pérez, and S. Riepe. Reaching a kerf loss below 100 μm by optimizing the relation between wire thickness and abrasive size for multi-wire sawing. *24th European Photovoltaic Solar Energy Conference, Hamburg, Germany (21-25 Sept. 2009)*, pages 1222–1227, 2009.
- [SSS83] M. Suezawa, Y. Sasaki, and K. Sumino. Dependence of photoluminescence on temperature in dislocated silicon crystals. *physica status solidi (a)*, 79(1):173–181, 1983.
- [Str80] R. A. Street. Recombination in $a - \text{Si} : \text{H}$: Defect luminescence. *Phys. Rev. B*, 21:5775–5784, Jun 1980.
- [SvSD⁺03] C. Smit, R. A. C. M. M. van Swaaij, H. Donker, A. M. H. N. Petit, W. M. M. Kessels, and M. C. M. van de Sanden. Determining the material structure

- of microcrystalline silicon from raman spectra. *Journal of Applied Physics*, 94(5):3582–3588, 2003.
- [SWS⁺85] R. Sauer, J. Weber, J. Stolz, E. R. Weber, K. H. Küsters, and H. Alexander. Dislocation-related photoluminescence in silicon. *Applied Physics A: Materials Science & Processing*, 36:1–13, 1985. 10.1007/BF00616453.
- [Sze81] S. M. Sze. *Physics of Semiconductor Devices*. John Wiley & Sons, Inc., second edition edition, 1981.
- [TBA05] T. Trupke, R. A. Bardos, and M. D. Abbott. Self-consistent calibration of photoluminescence and photoconductance lifetime measurements. *Applied Physics Letters*, 87(18):184102, 2005.
- [TBA⁺06] T. Trupke, R. A. Bardos, M. D. Abbott, F. W. Chen, J. E. Cotter, and A. Lorenz. Fast photoluminescence imaging of silicon wafers. *Photovoltaic Energy Conversion*, Conference Record of the 2006 IEEE 4th World Conference on Photovoltaic Energy Conversion, 2006.
- [TBA⁺07] T. Trupke, R.A. Bardos, M.D. Abbott, P. Würfel et al. Y. Augarten, F.W. Chen, K. Fisher, J.E. Cotter, M. Kasemann, M. Rüdiger, S. Kontermann, M.C. Schubert, M. The, S.W. Glunz, W. Warta, D. Macdonald, J. Tan, A. Cuevas, J. Bauer, R. Gupta, O. Breitenstein, T. Buonassisi, G. Tarnowski, A. Lorenz, H.P. Hartmann, D.H. Neuhaus, and J.M. Fernandez. Progress with luminescence imaging for the characterisation of silicon wafers and solar cells. *22nd European Photovoltaic Solar Energy Conference, Milan, Italy (3-7 Sept. 2007)*, pages 22–31, 2007.
- [TBSW06] T. Trupke, R. A. Bardos, M. C. Schubert, and W. Warta. Photoluminescence imaging of silicon wafers. *Applied Physics Letters*, 89(4):044107, 2006.
- [TGW⁺03] T. Trupke, M. A. Green, P. Würfel, P. P. Altermatt, A. Wang, J. Zhao, and R. Corkish. Temperature dependence of the radiative recombination coefficient of intrinsic crystalline silicon. *Journal of Applied Physics*, 94(8):4930–4937, 2003.
- [Thu75] C. D. Thurmond. The standard thermodynamic functions for the formation of electrons and holes in ge, si, gaas, and gap. *Journal of the Electrochemical Society*, 122:1133–1141, 1975.

- [TIO⁺12] Michio Tajima, Yasuaki Iwata, Futoshi Okayama, Hiroyuki Toyota, Hisashi Onodera, and Takashi Sekiguchi. Deep-level photoluminescence due to dislocations and oxygen precipitates in multicrystalline si. *Journal of Applied Physics*, 111(11):113523, 2012.
- [TOHR00] I. Tarasov, S. Ostapenko, C. Haessler, and E. U. Reisner. Spatially resolved defect diagnostics in multicrystalline silicon for solar cells. *Materials Science and Engineering B*, 71(1-3):51 – 55, 2000.
- [TTA92] M. Tajima, H. Takeno, and T. Abe. Characterization of point defects in si crystals by highly spatially resolved photoluminescence. *Materials Science Forum*, 83-87:1327–1332, 1992.
- [TTW95] M. Tajima, M. Tokita, and M. Warashina. Photoluminescence due to oxygen precipitates distinguished from the d lines in annealed si. *Materials Science Forum*, 196 - 201:1749 – 1754, 1995.
- [Var67] Y. P. Varshni. Band-to-band radiative recombination in groups iv, vi, and iii-v semiconductors (i). *physica status solidi (b)*, 19:459–514, 1967.
- [VFC⁺00] O Vetterl, F Finger, R Carius, P Hapke, L Houben, O Kluth, A Lambertz, A Mück, B Rech, and H Wagner. Intrinsic microcrystalline silicon: A new material for photovoltaics. *Solar Energy Materials and Solar Cells*, 62(1?2):97 – 108, 2000.
- [vRS54] W. van Roosbroeck and W. Shockley. Photon-radiative recombination of electrons and holes in germanium. *Phys. Rev.*, 94(6):1558–1560, Jun 1954.
- [VSI87] S. Veprek, F. A. Sarott, and Z. Iqbal. Effect of grain boundaries on the raman spectra, optical absorption, and elastic light scattering in nanometer-sized crystalline silicon. *Phys. Rev. B*, 36:3344–3350, Aug 1987.
- [VVK08] Martin Kittler Vitaly V. Kveder. Dislocations in silicon and d-band luminescence for infrared light emitters. *Materials Science Forum*, 590:29–56, 2008.
- [Wür05] P. Würfel. *Physics of Solar Cells: From Principles to New Concepts*. Wiley-VCH, first edition edition, 2005.

- [YHMW00] Guozhen Yue, Daxing Han, L. E. McNeil, and Qi Wang. Characteristics of the low energy photoluminescence in $\mu\text{c-si}$ films. *Journal of Applied Physics*, 88(8):4904–4906, 2000.
- [YHW⁺00] Guozhen Yue, Daxing Han, D. L. Williamson, Jeffrey Yang, Kenneth Lord, and Subhendu Guha. Electronic states of intrinsic layers in n-i-p solar cells near amorphous to microcrystalline silicon transition studied by photoluminescence spectroscopy. *Applied Physics Letters*, 77(20):3185–3187, 2000.
- [YLL⁺99] Guozhen Yue, J. D. Lorentzen, Jing Lin, Daxing Han, and Qi Wang. Photoluminescence and raman studies in thin-film materials: Transition from amorphous to microcrystalline silicon. *Applied Physics Letters*, 75(4):492–494, 1999.

Acknowledgments

First, I would like to express my deep gratitude to Prof. Martin Kittler for giving me the opportunity to prepare my Ph.D. thesis at the Joint Laboratory of IHP and Brandenburg University of Technology. Furthermore, I would like to thank Prof. Jürgen Reif for getting the permission to use his laboratories and equipment.

My special thanks to Dr. Tzanimir Arguirov, who always stood by my side during scientific work. He had great ideas not only in scientific issues, I have learned a lot from him. He made the scientific life more bearable.

I would like to express my thanks Christoph Krause, Dr. Winfried Seifert and Hans-Michael Krause for several SEM-measurements and helpful discussions.

Special thanks to Prof. Reiner Schmid for supporting me during the development of the PL imaging setup.

I am very thankful for the good cooperation and atmosphere with the Joint Lab colleagues during this work at BTU Cottbus. I only mention a few of the names here, Dr. Teimuraz Mchedlidze, Dr. Maxim Trushin, Jürgen Bertram, Dr. Markus Ratzke, Dr. Olga Varlamova, Markus Holla and Biwang Yang.

I especially thank my co-Ph.D.-students at the Joint Lab, Dr. Andre Klossek and Bernhard Schwartz. It made the work much more easy and enjoyable to have colleges in the same situation.

Our secretaries Marion Borrmann and Kathrin Staar are kindly acknowledged for their continuous help with all the small and big administrative problems.

I would like to acknowledge our project partners of SolarWinS project and the PVcomB project, for financial support and providing samples.

Finally, I feel incredibly grateful to my family for their love and patience. They always supported me during the last years in science.